ADVANCEMENTS IN QUANTITATIVE PERFUSION MAGNETIC RESONANCE IMAGING (MRI) OF DEMENTIA

by

Weiying Dai

B. S. in Mathematics, Peking University, 1996

M. S. in Computer Science, University of Pittsburgh, 2002

Submitted to the Graduate Faculty of

Arts and Sciences in partial fulfillment

of the requirements for the degree of

Doctor of Philosophy

University of Pittsburgh

2006

UNIVERSITY OF PITTSBURGH

FACULTY OF ARTS AND SCIENCES

This dissertation was presented

by

Weiying Dai

It was defended on

November 1, 2006

and approved by

Shi-kuo Chang, PhD, Professor

H. Michael Gach, PhD, Assistant Professor

Amer Ahmed, PhD, Assistant Professor

Patch Uthaisombut, Ph D, Assistant Professor

Dissertation Director: Shi-kuo Chang, PhD, Professor

Copyright © by Weiying Dai
2006

ADVANCEMENTS IN QUANTITATIVE PERFUSION MAGNETIC RESONACE IMAGING (MRI) OF DEMENTIA

Weiying Dai, PhD
University of Pittsburgh, 2006

Alzheimer's disease (AD) affects a considerable, and increasing, part of the population. Early diagnosis of AD is very important to permit effective therapy, and minimize AD's social and economic burden. The goal of our research is to evaluate the changes of cerebral perfusion (i.e., blood flow) in the early stages of AD and the effects from hypertension.

We studied volunteers with Mild Cognitive Impairment (MCI) and early AD from the Pittsburgh cohort of the Cardiovascular Health Study (CHS) Cognitive Study during a four-year follow-up. Previously, studies used referral patients who typically have more advanced AD. No perfusion data concerning the early and transitional disease stages are currently available from population studies (i.e., subjects who have been monitored longitudinally in time). There are no common techniques for perfusion quantification and image analysis so that inconsistencies are observed between/within studies, modalities, and researchers.

Several advancements were achieved in preparation for the cohort study. First, we improved the accuracy and speed of brain perfusion quantification. Second, we improved the accuracy of image registration to a reference brain using quantitative validation of a registration method and performance comparison with a popular registration method. Third, we improved the method of statistical analysis for evaluating the changes of perfusion between groups. Fourth, we evaluated the changes of cerebral perfusion between cognitive groups (controls, MCIs, ADs), and hypertension and normo-tensive subgroups.

Individual perfusion maps were improved by measuring and incorporating individual arrival time, saturation effects, and individual inversion efficiency. A fully deformable registration technique was shown to be more accurate than standard techniques like statistical parametric mapping to detect local perfusion changes. All of the published literature for perfusion up-to-date reported decreased perfusion in AD, but we found hyperperfusion in some regions. The regional findings imply that a hemodynamic process, at the capillary level, accompanied the neurodegenerative process. Hypertensive normal cognitive controls demonstrated hypoperfusion in regions usually involved in AD pathology. However, the effect of hypertension was attenuated after the onset of the pathological cognitive process.

TABLE OF CONTENTS

LIST OF TABLES

LIST OF FIGURES

ACNOWLEDGEMENTS

My first, and most earnest, acknowledgment must go to my advisors, Dr. Shi-Kuo Chang and Dr. H. Michael Gach. They always provide constant and timely guidance whenever I swap in the puzzles. They have been instrumental in ensuring my academic and professional wellbeing ever since. In every sense, none of this work would have been possible without them.

My special thanks go to Dr. Oscar O. Lopez, who provided not only financial support for my thesis project, but also the heuristic discussion for medical importance.

The time spent by Dr. Ahmed Amer and Dr. Patch Uthaisombut, and their suggestions to improve the thesis are all very much appreciated.

I am would like to thank my collaborators Dr. Owen Carmichael and Prasad Lakkavaram for the discussion regarding image registration tools.

I am grateful to Phil Greer, Dr Stuart Derbyshire, Dr. Howard Aizenstein, Minjie Wu for their generous help on countless occasions.

My final, and most heartfelt, acknowledgment must go to my husband, Guangwen Zhou. His support, encouragement, and companionship have turned my journey through graduate school into a pleasure. For all that, and for being everything I am not, he has my everlasting love.

1.0 INTRODUCTION

Alzheimer's disease (AD) is a serious health problem facing the United States and ranks as the fourth leading cause of death in the United States [1]. The prevalence of Alzheimer's disease (AD) ranges from 3% to 10% in subjects ages 65 and older, and from 20% to more than 30% in those ages 85 and older[2-4]. The incidence and prevalence of AD will continue to rise as the population ages and longevity increases. Prevalence is projected to increase from 8 to 13.5 million cases over the next 50 years in the U. S. [5, 6], creating a significant impact on the healthcare system and society.

The clinical diagnosis of AD typically comes late in the disease progression. This is primarily due to the lack of sensitive markers of early AD because of the similarities between normal aging and abnormal cognitive impairments that are a forerunner of AD [7]. Disease markers are important to devise effective treatments to prevent the onset of symptoms.

However, there is currently no cure for AD. The U. S. Food and Drug Administration (FDA) claimed no evidence for any candidate drugs that have an effect on the underlying progression of the disease, although there are some symptomatic treatments, such as acetylcholinesterase inhibitors [8]. One principle goal of AD research is to develop highly effective tools capable of identifying individuals who will eventually progress to AD to permit early diagnosis and therapeutic intervention.

There have been significant efforts from the medical community to understand the pathophysiology of the disease, especially the transition from normalcy to dementia. The transitional state has been called mild cognitive impairment (MCI) [9, 10], and its proper clinical identification is the key to devising effective therapies that can prevent, or delay, the onset of dementia. Similarly, the early diagnosis of AD is critical for the introduction of disease-modifying treatments.

1.1 THE MOTIVATION FOR RESEARCH SUBJECTS

Neuroimaging studies have provided valuable *in vivo* information of AD pathophysiology. Functional imaging techniques using positron emission tomography (PET) and single photon emission computed tomography (SPECT) showed decreased cerebral blood flow (CBF) or glucose metabolism in the temporal, parietal, and frontal heteromodal association areas, and mesial temporal lobe [11-17], and in the posterior cingulate gyrus [15, 16, 18-20] in AD subjects compared to normal individuals. MRI volumetric studies[17, 21-25], and continuous arterial spin labeling (CASL) perfusion MRI [26, 27] have shown atrophy and diminished CBF, respectively, in the same areas detected with functional methods.

Functional studies conducted in MCI subjects showed decreased metabolism in temporoparietal regions, especially in the posterior cingulate gyrus[12, 28-32]. MRI studies using region-of-interest analyses have shown that the volume of the hippocampus, entorhinal cortex and amygdala was reduced in MCI subjects compared to controls [33-39]. Studies based on whole brain techniques found that MCI subjects also had temporal, parietal, and frontal (including the subcallosal region of the anterior cingulate gyrus) volume loss [33, 40-42]. Taken together, these

studies showed that the MCI patients had cerebral changes not only in the mesial temporal lobe, but also in the heteromodal association areas. However, the majority of these studies were conducted in referral clinics [26, 27] with subjects that had advanced disease, especially MCIs.

Very little is known about CBF changes in MCI and early dementia in subjects from population cohorts. Neuroimaging studies in these subjects, especially those in early disease stages, are extremely important since the severity of symptoms may not have reached the threshold that usually initiates a referral to specialists. Therefore, neuroimaging of population cohorts provides an ideal opportunity to examine the incipient pathophysiological changes in AD, several years before they are enrolled in memory clinic imaging studies.

1.2 THE MOTIVATION FOR RESEARCH METHODOLOGY

MRI methods are able to provide the resolution comparable with, or superior to, nuclear medicine techniques such as PET and SPECT. First, MRI does not require the injection of radioactive tracers. Second, MRI is much cheaper and more widely available than PET. Third, it is easier to produce spatially registered structural information from MRI compared to SPECT or PET.

Two MRI techniques claim to provide a quantitative assessment of perfusion. The first of the techniques, dynamic susceptibility contrast magnetic resonance imaging (DSC-MRI), requires the injection of a contrast agent for which the acceptable maximum dose is limited. There are also quantification issues with DSC-MRI: 1) the relationship of changes in regional signal intensity to contrast agent concentration is complex; 2) an accurate quantification of

Artery Input Function (AIF) is difficult because the measured AIF may be affected by both a delay and dispersion between the artery where it was estimated and the volume of interest (VOI) [43, 44].

The second method, arterial spin labeling (ASL), employs radiofrequency (RF) pulses to invert naturally existing water proton spins (i.e., nuclear angular momentum) in the flowing blood prior to their arrival at VOI. ASL is commonly subdivided into two categories: continuous ASL (CASL) and pulsed ASL (PASL). CASL uses a continuous adiabatic RF pulse to invert blood water spins flowing through the carotids of the neck [45]. PASL uses a short RF pulse to invert blood water spins and minimize the distance between the labeling region and the image slice. Compared to CASL, PASL cannot cover the whole cerebrum in a single acquisition due to the smaller tracer bolus. We used the CASL technique in order to obtain the quantitative perfusion for the whole cerebrum. In addition, CASL can provide an improved signal-to-noise ratio (SNR) versus PASL[46].

1.3 THE CHALLENGE OF CASL MRI

CASL was first proposed by Detre et al. [47], who suggested the use of a train of RF pulses to repeatedly saturate blood water spins flowing throw the neck. The saturated spins flow into the brain and, assuming water is a freely diffusible tracer, exchange completely with brain tissue water, thus reducing the overall tissue magnetization. Soon after CASL was proposed, Williams et al.[45] improved the technique by using adiabatic fast passage (AFP) to label via spin inversion the arterial water spins [48, 49]. In AFP, an RF pulse is applied for several seconds to a plane in the neck of a subject, inflowing arterial water spins are inverted during this period, and a flow-

related steady state is achieved. The advantage of labeling arterial spins by inversion rather than saturation is an increase in the difference between the labeled and unlabeled states.

However, CASL has four well-recognized major problems in measuring tissue perfusion. First, the arrival time taken for spins to travel between the labeling plane and image slice voxels (sometimes referred to as the arrival time) is nonzero, and therefore spin relaxation occurs during the period. In the rat experiments, the short arrival time and the long T_1 of blood at the higher (4.7 Tesla) field strength reduced the impact of arrival times on the CBF quantification [50]. For human perfusion, however, arrival time dependence of the measured CBF represents a major obstacle to accurate quantification. Different people have different arrival times. Different regions of the brain have different arrival times, depending on the distance from the labeling plane and the cerebrovascular anatomy. These effects must be taken into account for accurate perfusion quantification.

Second, the application of a long (i.e., several seconds) off-resonance RF pulse in a single RF coil used for both labeling and imaging causes a decrease in the water signal resulting from magnetization transfer (MT) effects. No direct saturation of the observed water magnetization in the imaging slice occurs because of the narrow line width of the free water peak. However, off-resonance saturation of macromolecular spins does occur, resulting in attenuation of the free water signal through magnetization transfer [51]. The off-resonance saturation effects can mask the perfusion-dependent signal.

Third, multi-slice CASL imaging is complicated since the off-resonance saturation effects must be matched between both label and control acquisitions. Originally, the control plane was placed symmetrically opposite to the label plane with respect to the imaging slice and

only one slice was acquired. Several multi-slice techniques were developed to minimize the difference between off-resonance saturation effects in the label and control irradiations.

Fourth, the inversion (or labeling) efficiency (the measure of how efficiently the blood is inverted from the label and control plane) is not constant. Different people may experience different inversion efficiencies depending on the B_1 field at the label plane and the arterial blood velocity.

Researchers have worked to solve these issues. To account for the nonzero arrival time effect, one could measure the arrival time on a voxel-by-voxel basis and incorporate it into the original model (Bloch equation, will be introduced later) [52]. However, in most situations, SNR is found to be insufficient to estimate the arrival time with high spatial resolution [53]. Alsop and Detre [54] inserted a long time delay into the sequence between the end of the labeling period and the image acquisition and showed that if this delay is greater than the arterial arrival times across the image, then the resulting perfusion maps will be insensitive to variations in arrival time. However, the long postlabeling delay reduces the signal differences between control and labeled images, and the length of the delay is limited by T_1 relaxation and SNR. Furthermore, the long delay increases the experimental repeat time (TR) and constrains the acquisition volume.

The magnetization transfer (MT) effects decrease the MRI signal of both the label and control images**,** that are sensitive to the off-resonance saturation. The labeling plane is positioned in a transverse plane which is orthogonal to the supplying arteries. Even within a subject, all the imaging slices experience different off-resonance frequencies because those imaging slices are placed at varying distances from the labeled plane. For different subjects, the labeling planes may have varying distances from the center of the imaging section. Therefore, the MT effects vary regionally and between experiments, and so the effects must be properly

corrected. The MT effects need to be characterized for accurate perfusion quantification. MT effects were modeled and interpreted [55-58], but these MT models described the MT effects in steady-state, which is not necessarily the case in our CASL experiments.

Three methods were proposed to tackle multi-slice CASL imaging. First, an RF surface coil with a small spatial range was placed on the neck and used to perform spin labeling [59]. The B_1 field generated by the coil does not reach the imaging slices and thus causes no off-resonance saturation in the imaging volume.

Second, simultaneous proximal and distal irradiation (SPDI) [60] was developed to generate a small imaging volume in which the residual off-resonance saturation effects (i.e., the difference in saturation effects between control and label irradiations) are minimized. Equal RF power was applied proximal and distal to the slices to be imaged. Two-site irradiation applied in the presence of a gradient served as the labeling, while the same RF power in the absence of the gradient served as the control. Off-resonance saturation effects are similar with and without the gradient for the slices within the flat portion of the MT profile. However, the residual off-resonance effects are small relative to the CASL (difference) signal only for a few middle slices (usually 3-5 slices). The coverage of the whole cerebrum cannot be performed using a single experiment.

Third, *A*lternating *S*ingle adiabatic inversion (SAI) label and *D*ouble adiabatic inversion (DAI) control pulses (ASD) was developed to cover the whole cerebrum [61]. ASD used a pair of narrowly separated inversion planes to serve as the control. As spins flow through the first inversion plane, they are inverted and then immediately uninverted. The control RF pulse was designed to achieve identical off-resonance saturation effects throughout the brain. However, ASD suffers from inefficiencies in both the control and label. The inefficiencies may reduce the

perfusion SNR [62, 63] relative to the conventional single-slice CASL using alternating proximal and distal irradiations (APDI) [45] given the same labeling conditions.

The inversion efficiency may vary significantly between subjects since it is flow-velocity dependent [46] and the labeling and control planes tend to lie in the inhomogeneous region of the RF coil. Previous researchers cited relative ASD and APDI efficiencies obtained from the earlier *in vivo* measurements without compensating for varying clinical condition. The relative efficiencies based on comparisons of ASD and APDI signals are subject to significant errors from MT asymmetry [64] and residual MT gradient associated with APDI. There was no standard method for estimating the inversion efficiencies specifically for each experiment. Yet, knowledge of the inversion efficiency is key to the accurate quantification of perfusion.

Another important problem that has been neglected so far is the slice acquisition order. Researchers usually acquire the slice from inferior to superior order. But this image acquisition order can perturb the tracer and exacerbate off-resonance saturation effects.

1.4 THE CHALLENGE OF ELDERLY BRAIN NORMALIZATION

Statistical comparison of the perfusion changes between subject groups requires geometrical alignment (or registration) of the subject image to a reference image, i.e. brain normalization. The brain normalization is to remove the anatomical variability of different brains. The match of fine cortical structures between subject image and the reference image is a natural requirement for accurate normalization.

The widely used reference images are 1) Montreal Neurological Institute (MNI) template ICBM152, which was created from the average of 152 young templates, 2) Colin27 brain, in

which the brain of Colin Holmes (one of the MNI lab members) was scanned 27 times; the scans were coregistered and averaged to create a very high detail MRI dataset of one brain; the average was also registered to the MNI305 (the first MNI template). However, both reference images are the templates from young people.

Spatial normalization of elderly brains is a challenging issue. Whole brain volume and fine cortical structures have large variability between individuals that may change at different atrophy rates as people age. Individual brain image voxels may deform or warp at different rates during the brain normalization. The deformation variability across cortical structures requires an accurate normalization method to match the cortical structures between individual brain and the template. A poor normalization method will bias group comparisons. Therefore, the performance of spatial normalization on elderly brains has an important effect on group comparisons when applied to functional and structural imaging.

Two popular automated brain normalization packages for brain analysis are automated image registration (AIR) and statistical parametric mapping (SPM). However, both methods have limited dimensions in brain deformation. AIR adopts a polynomial basis function of low dimension, SPM uses a geometric transformation model with low-dimensional discrete cosine transformation (DCT) basis functions.

However, Chen proposed a high-dimensional method [65] (referred to as the fully deformable normalization method), which combines the piecewise linear registration and dense voxel-by-voxel geometric transformations, and allows each voxel to move without any constraint. The fully deformable method has the potential precision to match each cortical feature with substantial fine-scale deformation. Therefore, the normalization method may be very important in studying AD since only fine brain cortical structures may be affected for the disease especially

like AD. But the accuracy of the normalization methods needed to be evaluated and to be applied in the CASL brain normalization.

1.5 THE CHANLLENGE OF STATISTICAL ANALYSIS

Most neuroscience imaging researchers use SPM to perform the statistical analysis of functional MRI (fMRI) data. The SPM package assumes that all the voxels which are used to make statistical inferences contain valid data. However, the statistical inference may make no sense without justifying the valid data assumption from all subjects for each analyzed voxel.

There are some practical considerations in regard to the valid data assumption if complete brain coverage is not adopted. First, there are variations in brain acquisition coverage. It is difficult to get exactly the same slice coverage even if the same person is scanned twice. It is not possible for some elderly subjects to put their head in the predetermined direction or orientation (e.g. due to some disease). Second, there are large variations in brain dimensions. Even if the head is put in the scanner parallel to one direction perfectly and the slice starts from the same anatomical structure with the same slice thickness and interslice spacing, it will not end at the equivalent anatomical structure due to the variance of longitudinal length. These practical issues make the SPM data processing package invalid to apply directly.

Another alternative approach is to apply the SPM data processing package to a common brain volume for all subjects. However, this approach may leave out large areas of cortical region. To get larger cortical regions analyzed statistically, one can choose to exclude brain data of some subjects which have less overlap with others. However, researchers normally suffer

with small samples. Based on those considerations, we implemented the voxel-level statistical analysis in separate code to analyze the valid data only and utilize the available data maximally.

1.6 RESEARCH DESIGN

To resolve the above research issues, we summarize our research design for the issues in Table 1.1. The significance of our research design is also listed in the Table.

Table 1.1. Summary of research issues, research designs and significance

Topics	Issues from Previous Studies	Research Design	Significance
Subjects	Studied only normal controls and very diseased AD subjects.	Studied normal controls, MCI and early AD patients.	Examine the incipient perfusion changes in MCI and AD patients for early diagnosis and therapy.
Postlabeling Delay	Used long delay: reduces the signal amplitude and SNR, time cost is large, need two 8-minute acquisitions to cover the brain, and is limited by tracer T_1 relaxation.	Used shortened delay: only need one acquisition to cover the whole brain.	Increased perfusion signal amplitude and SNR; time cost is reduced to almost half; whole brain in one acquisition reduced possible motion; Increased complexity of quantification.
MT Effects & Residual Off-resonance Saturation Effects	Assumed negligible residual off-resonance saturation effects.	Established a dual-Lorentzian MT model to fit the experimental data and model the residual effects from *in vivo* measurements. Apply models to correct individual data sets based on their experiment conditions (B_1, label distance)	MT, residual off-resonance saturation, and nonadiabatic effects vary between subjects and experiments. These effects can be significant especially for short postlabeling delays.
Inversion Efficiency	Assumed that it is constant.	Established an analytical model and validated with the experiments.	Varies between subjects and experiments significantly. Offer the researcher the ability to correct the perfusion

			quantification due to the variance of clinical conditions.
Arrival Time	Assumed the inserted postlabeling delay is long enough for the labeling blood to be delivered to the imaging slice.	Measured the arrival time indirectly for each individual subject.	Get the arrival time of each individual subject measured at the mean time. Avoid wasted time after tracer arrival (early arrivals of tracer) or insufficient postlabeling delay (e.g. for diseased subjects)
Acquisition Order	From inferior to superior	From superior to inferior.	Keep the blood tracer intact and alleviate the off-resonance saturation effects and crosstalk.
Brain Normalization	Corrected for global brain shape differences.	Allowed transformation of each voxel unconstrained for fine matches of cortical features.	Better detection of perfusion abnormalities of fine cortical structures.
Statistical Analysis	Only analyzed the voxels in which all subjects have valid data.	Analyze the voxels in which the majority of the subjects have valid data.	Maximize the brain volume that is evaluated.

1.7 RESEARCH STATEMENT

The first objective of this research is to improve the accuracy and speed of cerebral blood flow (CBF) measurements acquired using CASL, a non-invasive endogenous tracer technique. We achieved this by characterizing or modeling kinetic variables and improving image analysis techniques.

The second objective is to evaluate perfusion changes using CASL among age-matched normal controls, MCI and early Alzheimer's disease (AD) subjects, and probe the hypothesis that perfusion drops as dementia progresses. We achieve this objective by applying the fully

deformable normalization method to warp the improved perfusion maps to the standard space and using image-based voxel-by-voxel analysis and cluster-level statistical analysis to detect regional perfusion abnormalities.

One recent study suggests that people with hypertension or hypercholesterolemia are more likely to develop Alzheimer's disease. Therefore, the third objective of this research is to compare the perfusion changes related to hypertension to evaluate risk factors of hypertension and cardiovascular disease to dementia.

1.8 RESEARCH OUTLINE

Chapter 1 provides a high level motivation for the dissertation research to be conducted, and outlines the research objectives. Chapter 2 presents basic concepts of CASL and further exposes the issues surrounding CASL. Chapter 3 establishes the dual-Lorentzian model of off-resonance saturation. Chapter 4 introduces and verifies an analytical model for inversion efficiency. Chapter 5 discusses the CASL kinetic model for perfusion quantification. Chapter 6 adopts a fully deformable registration technique to CASL perfusion analysis. Chapter 7 applies these quantitative techniques to the study of CBF in the progression of dementia. Chapter 8 evaluates risk factors of hypertension and cardiovascular disease to dementia.

2.0 FOUNDATION

2.1 INTRODUCTION OF MRI BASIC CONCEPTS

2.1.1 What is MRI?

MRI is a tomographic imaging technique that produces images using nuclear magnetic resonance (NMR) signals [66].

MRI formation can be described as follows: First, nuclear spin angular magnetic moments (collectively called magnetization) are polarized by a main static magnetic (B_0). Second, the orientation of the magnetization is tipped or nutated by tuning RF (B_1) to the resonant (precession) frequency and measured using magnetic field induction. Third, a magnetic field gradient is used to spatially encode and readout the magnetization by creating linearly-varying precessional frequencies. The MRI signal is readout or sampled in conjugate k-space and converted into an image typically using Fourier transformation.

2.1.2 Magnetized nuclear spin system

A physical object is composed of nuclei and electrons. These nuclei possess a spin angular momentum. At room temperature, the spin orientations are completely random in the absence of an external magnetic field, due to thermal random motion.

The nuclear spin vectors μ is lined up to activate macroscopic magnetism from an object by exposing the object to a strong external magnetic field B_0. For spin-1/2 nuclei (normally referred to as a nuclear spin system) like ^1H, ^{13}C, ^{19}F and ^{31}P, a spin takes one of two possible orientations: parallel or antiparallel to the B_0 direction, as shown in Fig 2.1. The angle θ between μ and B_0 is $54^0 44'$ based on the relation of magnetic moment number and spin quantum number. The angular frequency of nuclear precession is

$$\omega_0 = 2\pi f_0 = \gamma B_0 \qquad (2.1)$$

where γ is physical constant known as the gyromagnetic ratio. ω_0 is known as the Larmor precession rate and f_0 is called the Larmor frequency.

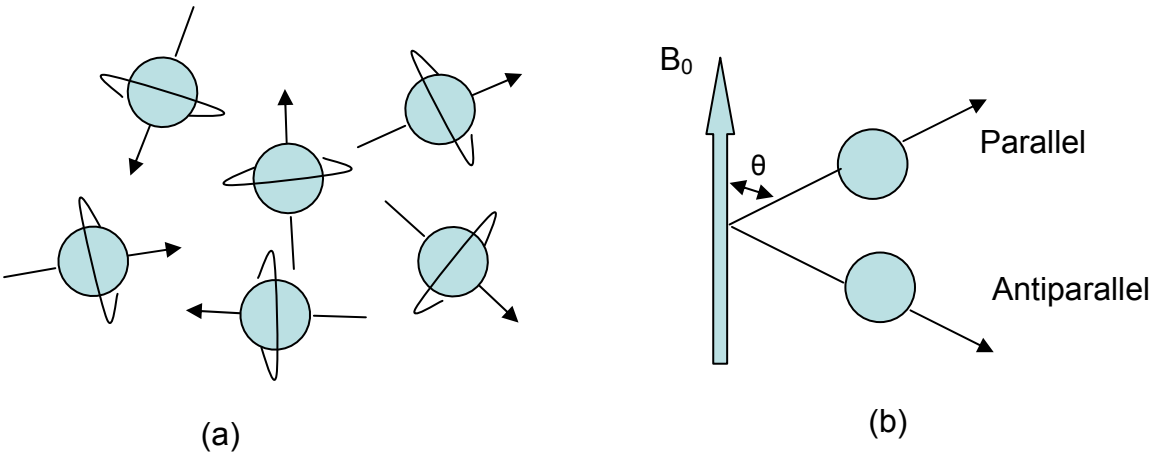

Figure 2.1. Nuclear magnetic moment vectors. (a) pointing in random directions and (b) aligned in the direction of an external magnetic field.

Quantum theory indicates that the parallel state is the lower energy state, while the antiparallel state is the higher energy state. The Boltzmann relationship is:

$$\frac{N_{para}}{N_{anti}} = \exp(\frac{\Delta E}{kT_s}) \qquad (2.2)$$

where N_{para} is the number of spins parallel to B_0, N_{anti} is the number of spins antiparallel to B_0, T_s is the temperature of the spin system (in Kelvin), $\Delta E = \gamma h B_0/(2\pi)$ is the energy difference

between the two states, k is the Boltzmann constant, γ is the spin gyromagnetic ratio, h is the Planck constant. Equation (2.2) indicates that there is small excess of a spins in the low-energy state near room temperature (T_s=300K). The population difference between the two spin states generates an observable macroscopic magnetization pointing along the direction of B_0 from a spin system. Such a spin system is said to be magnetized or polarized.

2.1.3 RF excitations

For a polarized spin system, the observable bulk magnetization is pointing along the direction of B_0. There is no net transverse component of the bulk magnetization at equilibrium because each microscopic magnetic moment vector has a random phase. Establishment of a phase coherence among these randomly precessing spins in a polarized spin system is referred to as resonance.

An external force, an oscillating magnetic field denoted as B_1, is added into the magnetized spin system to generate the resonance condition. The resonance condition based on classical physics is that B_1 rotates in the same manner as the precessing spins. i.e., the radiation frequency ω_{rf} of B_1 is equal to the Larmor frequency ω_0.

$$\omega_{rf} = \omega_0 \tag{2.3}$$

Equation (2.3) is known as the resonance condition.

The B_1 field is typically applied as an RF pulse, which is normally turned on for a few microseconds or milliseconds. Morever, the B_1 field is much weaker compared with the static B_0 field.

The change of bulk magnetization M with time after applying magnetic field $B_1(t)$ is described quantitatively by the Bloch equation, ignoring relaxation.

$$\frac{d\vec{M}}{dt} = \gamma\vec{M} \times \vec{B} \tag{2.4}$$

As a result of the RF pulse, the bulk magnetization is tipped away from the B_0 direction, creating a measurable transverse magnetization component. The flip angle is defined as the resulting angle between M and the B_0 direction. The flip angle depends on both the magnitude of $B_1(t)$ and the duration that B_1 is applied on. When $\omega_{rf} \neq \omega_0$, the RF excitation is called off-resonance excitation.

2.1.4 Free precession and relaxation

The tipped magnetization after an RF pulse will return to its thermal equilibrium state according to the laws of thermodynamics if given sufficient time and the RF pulse is removed. This process is characterized by a precession of M about the B_0 field, called free precession; a recovery of the longitudinal magnetization M_z, called longitudinal precession; and the destruction of the transverse magnetization M_{xy}, called transverse relaxation. The Bloch equation takes the general form after adding the relaxation process:

$$\frac{d\vec{M}}{dt} = \gamma\vec{M} \times \vec{B} - \frac{M_x\vec{i} + M_y\vec{j}}{T_2} - \frac{(M_z - M_z^0)\vec{k}}{T_1} \tag{2.5}$$

where T_1 and T_2 are time constants characterizing the longitudinal and transverse relaxation process of the spin system, respectively, after it has been disturbed from its thermal equilibrium state. Both the decay of transverse magnetization and the recovery of longitudinal magnetization after an RF perturbation follow an exponential function from Equation (2.5).

2.2 PERFUSION AS PHYSIOLOGICAL STATUS

The term perfusion describes the amount of blood delivered to the capillary beds of a block of tissue in a certain period of time. Its units are nominally milliliter of blood per 100 g of tissue per minute. Perfusion is blood flow at the capillary level, different from bulk blood flow which occurs along major arteries and veins. It reflects the delivery of oxygen and other nutrients to the tissue, and so is related to the energy status or metabolism of the tissue.

2.2.1 Measurement (Models) of Perfusion & current status

Researchers have put much effort into the measurement of perfusion since perfusion is an essential hemodynamic parameter. Numerous diagnostic imaging techniques (such as PET, SPECT, and MRI) have been devised to measure tissue perfusion. Some of the studies targeted relative perfusion. However, this research will only concentrate on the quantification of absolute perfusion. Each technique is based on the principles of tracer kinetics.

PET quantitative measurement of perfusion involves the intravenous injection of a radioactive tracer (such as $H_2{}^{15}O$). Perfusion was calculated using either the time-weighted integral method [67], a method not requiring arterial blood data [68], or a method based on tracer-washout rate [69]. The three methods are based on the one-tissue compartment model for $H_2{}^{15}O$ represented by the differential equation:

$$\frac{dC(t)}{dt} = K_1 C_a(t) - k_2 C(t) \tag{2.6}$$

where *C(t)* denotes tissue activity concentration. *Ca(t)* is the measured arterial input function (AIF), K_1 is the influx rate constant for washin (regional perfusion) and k_2 is the outflux rate constant for washout (regional perfusion/partition coefficient). Assuming no tissue activity before tracer application at time zero, the solution of Eq. (2.6) is given by:

$$C(t) = K_1 C_a(t) \otimes e^{-k_2 t} = K_1 \int_0^t C_a(u) e^{k_2 (u-t)} du \qquad (2.7)$$

SPECT perfusion also uses an intraveneous radiolabeled tracer (such as ^{99m}Tc-ECD). A three-compartment model was used to describe the tracer kinetics [70-72] (Fig. 2.2). The following equation can be used to describe the model:

$$C_b(t) = \frac{K_1 \times k_3}{k_2 + k_3} \int_0^t Ca(\tau) d\tau + \frac{K_1 \times k_2}{k_2 + k_3} \int_0^t Ca(\tau) e^{(k_2 + k_3)(\tau - t)} d\tau \qquad (2.8)$$

where *Ca(t)* and $C_b(t)$ are the respective concentrations of the tracer in arterial blood and brain tissue corrected for physical decay. K_1 is the influx rate constant for washin (regional perfusion) and k_2 is the outflux rate constant for washout (regional perfusion/partition coefficient). k_3 is the lipophilic-to-hydrophilic conversion constant and k_4 is the hydrophilic-to-lipophilic conversion constant. The reverse conversion constant, k_4, is hypothetic, and its value is assumed to be zero in these studies. It is not difficult to see that the SPECT three-compartment model (Equation 2.8) can be simplified into the PET one-tissue compartment model assuming k_3 to be zero.

Two main MRI approaches for perfusion quantification have been developed: dynamic susceptibility contrast (DSC) MRI and arterial spin labeling (ASL). DSC MRI involves the injection of a bolus of contrast agent. Since the arrival time of the bolus through the tissue is only a few seconds, a fast imaging technique is required to obtain sequential images during the washin and washout of the contrast material. Single-shot echo planar imaging (EPI) or spiral

acquisitions, a fast imaging technique, allows an improved characterization of the passage of the bolus and facilitates the acquisition of multislice data, thus increasing the regional coverage of the technique. The DSC model relies on the assumption that in the presence of an intact BBB, the contrast material remains intravascular. The concentration $C_{VOI}(t)$ of tracer in given volume of interest (VOI) can be described by the following equation [73]:

$$C_{VOI}(t) = (\frac{\rho}{k_H})F_{VOI}(C_a(t) \otimes R(t)) \qquad (2.9)$$

where $C_a(t)$ is the concentration of contrast agent entering VOI at time t. R(t) is the residue function, the fraction of injected tracer still present in the VOI at time t following an ideal instantaneous unit bolus injection at time t = 0. F_{VOI} is the perfusion in the VOI, ρ is the density of brain tissue and k_H accounts for the difference in haematocrit (H) between capillaries and large vessels.

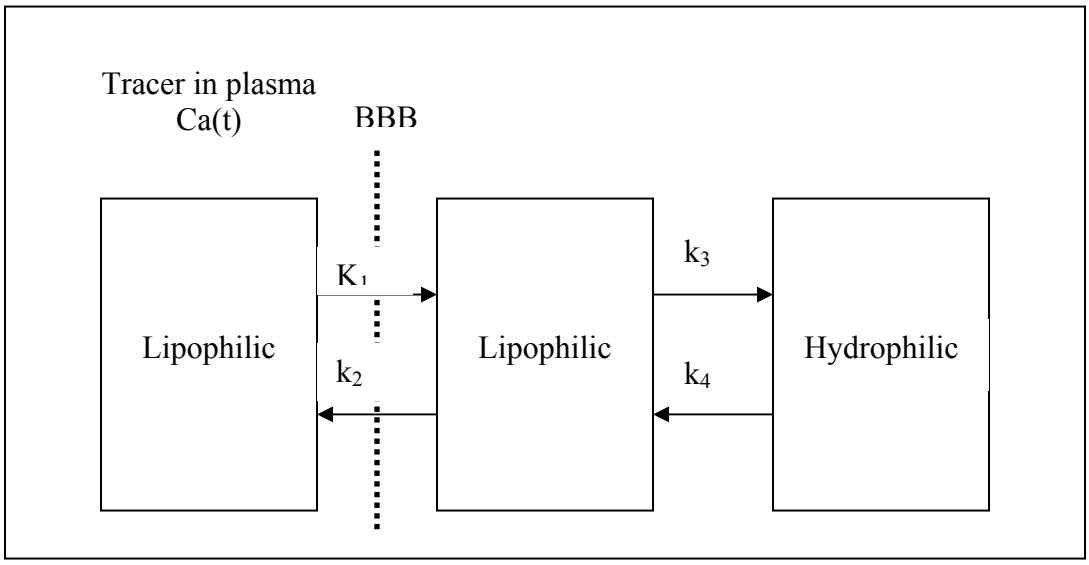

Figure 2.2. Kinetic model of the tracer with three compartments and four parameters. K1 to k4 are rate constants for transport of tracer between compartments. Ca(t) and Cb(t) are respective concentrations of the tracer in arterial blood and brain tissue corrected for physical decay. BBB = blood-brain barrier.

ASL employs endogenous blood water as the tracer. An MR image can be made sensitive to the effect of inflowing blood spins if those spins are polarized differently than the tissue water spins. ASL fulfills this idea by saturating or inverting the magnetization of the arterial blood [45, 47]. Blood water carrying the labeled magnetization flows into the image slice and exchanges with tissue water. Perfusion is directly related to the subtraction of an image in which inflowing blood spins have been labeled from an image (the labeled image) in which inflowing spins are intact (the control image). The tissue model for quantification of perfusion with ASL can be derived from the Bloch equation for longitudinal relaxation when it is modified to include the effects of flow [47]:

$$\frac{dM_b(t)}{dt} = \frac{M_b^0 - M_b(t)}{T_1} + fM_a(t) - \frac{f}{\lambda}M_b(t) \qquad (2.10)$$

where $M_b(t)$ is the longitudinal magnetization per gram of brain tissue water, M_z^0 is the magnetization of fully relaxed tissue, T_1 is the longitudinal relaxation time, f is the perfusion (converted to ml /100g-min), $M_a(t)$ is the magnetization of the inflowing arterial blood per ml, λ is the blood:brain partition coefficient. The first term [$fM_a(t)$] represents the gain of magnetization by the tissue caused by inflows, and the second term $\frac{f}{\lambda}M_b(t)$ accounts for the loss of magnetization due to outflow. This tissue model can be subsumed into the general kinetic model as a special case with appropriate assumptions (1. the arrival of labeled blood at a particular voxel is via uniform plug flow; 2. the kinetics of water exchange between tissue and blood is described by a single-compartment; 3. the water is completely extracted from the vascular space.)[74]. The general model for quantitative perfusion imaging with ASL is described as:

$$\Delta M(t) = 2\alpha M_{0b} f\{c(t) * [r(t)m(t)]\} = 2\alpha M_{0b} \int_0^t c(t')r(t-t')m(t-t')dt' \qquad (2.11)$$

where $\Delta M(t)$ is the difference in control and labeled longitudinal magnetization due to blood that entered the voxel during the interval [*0, t*] and still present in the voxel; M_{0b} is the magnetization of fully relaxed arterial blood; α is the inversion efficiency, a fraction accounts for the imperfect inversion; f is the perfusion rate; *c(t)* is the arterial delivery function, i.e. the normalized arterial concentration of magnetization arriving at the voxel at time *t*; *r(t, t')* is the residue function, the fraction of labeled water that arrived at time *t'* and is still in the voxel at time *t*; *m(t, t')* is the magnetization relaxation function, i.e. the fraction of original longitudinal magnetization carried by water that arrives at time t' that remains at time *t*. Assuming that the physiological state of the tissue is not changing, then *r(t, t')* and *m(t, t')* are functions of just the interval *t-t'*, and are written as *r(t)* and *m(t)*. $\Delta M(t)$ is constructed as a sum over the history of delivery of magnetization to the tissue weighted with the fraction of that magnetization that remains in the voxel. After the inversion pulse, the arterial magnetization difference is ideally $2M_{0b}$ but practically $2\alpha M_{0b}$ due to the imperfect inversion. The amount of magnetization delivered to a particular voxel between *t'* and *t'+ dt'* is $2\alpha M_{0b} fc(t')dt'$, the fraction of that magnetization that remains at time *t* is $r(t-t')m(t-t')$. The kinetic model takes into account a finite arrival time and limited bolus width.

In all of these perfusion models, the tracer concentration at time *t* can be expressed as a superposition of the tracer arterial input function weighted with the residue function over the time interval [*0, t*], which we see in convolution form in the models; the perfusion is proportional to the tracer concentration and inversely proportional to the convolution.

2.2.2 Measurement of perfusion using ASL

In ASL, arterial magnetization is usually achieved by spin inversion. The various ASL techniques can be distinguished by different ways in which the spin inversion is achieved. Two techniques have been developed: CASL and PASL.

CASL: The first CASL proposed by Detre et al. [47] used a train of RF pulses to continuously saturate (or label) the blood water as it flowed into the brain for several seconds. A steady state of brain tissue magnetization developed and a labeled image was acquired. A control image was acquired without labeling the arterial water. The difference between these two images led to the perfusion map from Equation (2.10) [45]:

$$f = \frac{\lambda}{T_{1app}} \frac{(M_b^{cont} - M_b^{label})}{2\alpha M_b^{cont}} \tag{2.12}$$

where M_b^{cont} and M_b^{label} were the steady state control and labeled tissue magnetizations respectively, T_{1app} was the longitudinal relaxation time of brain tissue including the effect of flow:

$$\frac{1}{T_{1app}} = \frac{1}{T_1} + \frac{f}{\lambda} \tag{2.13}$$

Equation (2.13) describes the relationship of the apparent longitudinal relaxation time to perfusion.

Willams et al. [45] improved the first CASL technique by replacing the spin saturation with adiabatic first passage (AFP). The blood water proton spins flowing through magnetic field gradient G at velocity v are inverted if the adiabatic condition [48] is satisfied, i.e.

$$1/T_{1a}, 1/T_{2a} << (1/B_1)Gv << \gamma B_1 \tag{2.14}$$

where T_{1a}, T_{2a} are the longitudinal and transverse relaxation times of arterial blood water; B_1 is the amplitude of the RF pulse; G is the amplitude of the field gradient; v is the blood velocity;

and γ is the gyromagnetic ratio of the nuclei. In practice, this means that inversion must take place in a major artery where the blood velocity is sufficient to satisfy the above condition. Some of the velocities may not meet the adiabatic condition since a range of velocities may be present, resulting in imperfect inversion of arterial blood magnetization. The inversion efficiency α was introduced to Equation (2.11) and (2.12) to account for the imperfect inversion effect. α is 1 if all flowing water spins are inverted and 0 if no spins are inverted at all.

Several additional factors affect the accuracy of perfusion quantification using CASL. The most important of these are addressed below. The first factor is the arterial arrival time. Equation (2.12) assumes that blood water reaches the tissue of interest in a state defined by α, the inversion efficiency. However, the blood spin takes time to travel from the place where the spin is originally inverted to where it reaches the tissue, and the degree of blood spin inversion decreases during the arrival time due to the T_1 relaxation. Zhang et al. [52] took this effect in account by measuring the arrival time and incorporating it into the Bloch equation analysis. An arrival time map on a voxel-by-voxel basis is necessary since a range of arrival times will exist across an image. However, SNR and time restrictions do not typically allow the accurate estimate of arrival time on a voxel-by-voxel basis. Alsop and Detre modified the standard CASL technique by putting a delay between the end of labeling period and the image acquisition [54]. They showed this approach prevents the quantification of perfusion from being sensitive to differences in arrival time, as long as the delay is longer than arrival times for the whole image. However, the long delay will cause a loss of SNR and is limited by the T_1 relaxation.

The second factor affecting perfusion accuracy is magnetization transfer (MT). The long off-resonance RF pulse used to invert the arterial blood water, results in off-resonance saturation of water. Although no direct saturation of the observed water magnetization occurs in the

imaging slice due to the narrow resonance peak of free water and several kHz off-resonance of the RF pulse, the magnetization of water bound to macromolecules is affected because of the very wide resonance peak of this group of spins. MT through chemical exchange or coupled cross-relaxation between free water and water bound to macromolecules causes the observed MRI signal to drop.

MT effects decrease the signal magnitude of both label and control images. If the off-resonance saturation effects are matched for the label and control, the residual MT (ΔMT) is zero. If the saturation effects are not matched, ΔMT can mask the perfusion signal. MT effects need to be removed from the control-label difference signal for accurate quantification of perfusion [52, 75].

The CASL control image must experience exactly the same MT effects as the labeled image. One can place the control plane above brain either by changing Δf polarity or gradient polarity, The former is preferable to maintain the same gradient-induced eddy current effects between the label and control. Certainly no blood inversion occurs in this case, but only a single slice could satisfy the MT matching condition, making this method hard to extend to multislice acquisition (Figure 2.3a).

A two-coil setup can be used to prevent the saturation of macromolecules [76]. A small surface coil is placed on the neck for arterial blood labeling, and no off-resonance saturation effects are noticed in the brain since the B_1 of the small coil is only limited in the neck region. A separate RF coil is used for imaging. This approach can be extended to multislice perfusion imaging since there is no off-resonance saturation effect in either the control image or the labeled image. However, this method requires specialized hardware that is not available from commercial scanners. In addition, macromolecules are not saturated so chemical exchange of labeled spins becomes a significant concern in perfusion kinetics.

The third factor affecting perfusion accuracy is the intravascular signal contamination. Both MRI ASL perfusion models describe the relation between perfusion and tissue water magnetization. However, a MRI voxel signal may come from capillaries and from large vessels. The signal in large vessels will contribute to a signal difference between control and labeled image, which is not desirable for the perfusion calculation. If a significant amount of signal emanates from the large vessels, perfusion will be overestimated. Flow-sensitive crusher gradients have been used to eliminate signal from these large vessels [47, 53], but these tend to reduce the perfusion signal resulting in an underestimation of perfusion.

Another alternative approach is the arrival time insensitive sequence as mentioned above from Alsop and Detre. The long postlabeling delays allow most of the labeled blood to either exchange with the tissue or wash through the large vessels. However, the resulting difference signal is smaller or the tracer may relax altogether resulting in an underestimation of perfusion. In addition, it is unclear how to ensure the postlabeling delay is larger than the transit time if the latter is unknown.

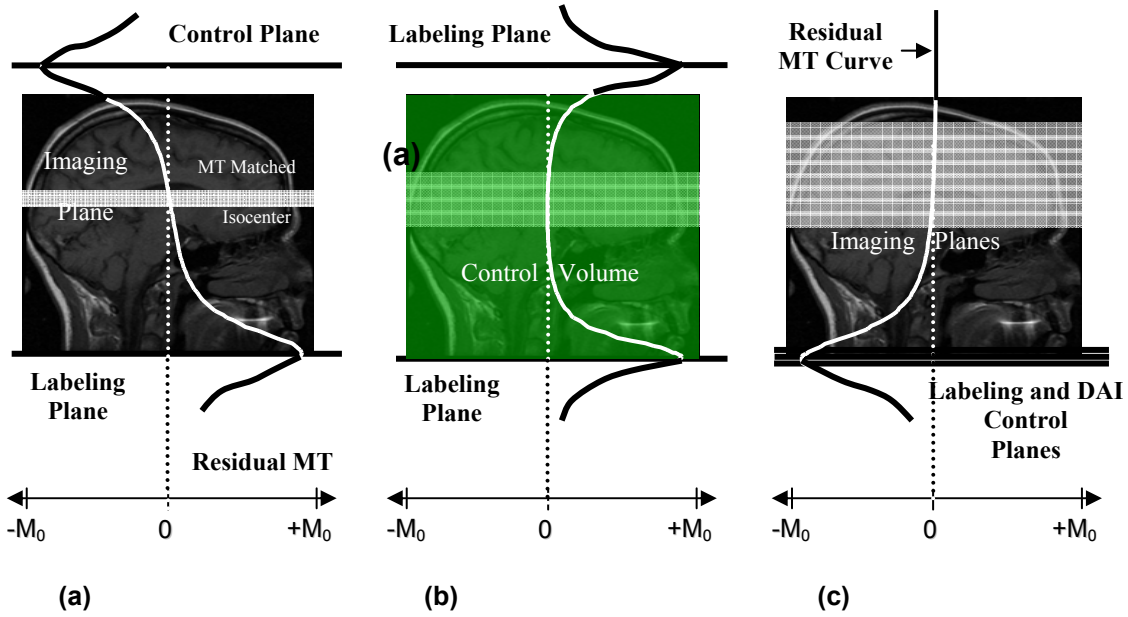

Figure 2.3. Off-resonance saturation effects of control and label planes of CASL: (a) single-slice alternating proximal and distal irradiation (APDI), (b) multislice simultaneous proximal and distal irradiation (SPDI), (c) multi-slice alternating single adiabatic inversion and double adiabatic inversion (ASD).

2.2.3 Advantages and disadvantages of perfusion MR techniques

Although neither ASL nor DSC-MRI requires ionizing radiation, ASL has the extra benefit of using an endogenous contrast agent. Therefore, multiple measurements can be performed, in principle, without any restriction. The complete noninvasive character of ASL makes it superior to DSC for research studies. Although multiple bolus injections of contrast agent can be performed, the acceptable maximum dose is typically limited to 0.3 mmol/kg per exam. A lower dose which must be administered in multiple measurements reduces the sensitivity of the technique. An advantage of DSC is that the change in signal intensity is generally 10-50%. In ASL, the intrinsic perfusion signal is normally only 0.5-3% so that excellent SNR is required for accurate perfusion measurements.

Although both MRI techniques behave reasonably well in the range of normal perfusion values, they have difficulties in dealing with very high or very low perfusion. With very low flow, the first obvious limitation is the low SNR of the measurement. This can be improved in the ASL technique by increasing the number of averages, which is not optional in typical single DSC studies because of its dynamic character.

The second problem is related to the presence of long arrival delays for the arterial blood to the region of interest, which is the case for collateral circulation in stroke regions. Extra delays of up to several seconds can be observed in the ischemic tissue. The very long arrival delays are one of the fundamental limitations of the ASL technique for measuring perfusion [46, 52-54, 77]. It may be impossible to have the tagged tracer arriving at the tissue before relaxation and,

therefore, no effect will be observed. For DSC studies, the presence of long bolus arrival times is also a problem. The transit of the bolus from the site of injection (typically a vein) to the VOI can introduce a delay, as well as dispersion (spread of the bolus shape). If one does not account for this delay and dispersion, it may cause an underestimation of the perfusion [43, 44, 73, 78]. Although one can account for the dispersion from the site of injection (vein) to the artery where AIF is measured, the extra dispersion from the artery to the input of the VOI (where the true AIF should be obtained) cannot be ascertained easily. The extra dispersion is particularly significant in cases of collateral flow to ischemic areas. To address this problem, a mathematical vascular model has been incorporated into the DSC analysis [43]. However, further validation is needed for a large number of patients with cerebrovascular diseases.

The case of very high flows can be problematic for both MRI techniques. For ASL, the assumption of complete exchange may not be valid for high CBF [79, 80]. If this incomplete exchange is not taken into account, the perfusion will be underestimated since only a fraction of the arterial magnetization is exchanged. For DSC, the response curve is narrowed, resulting in potential difficulty to accurately characterize perfusion for a given time resolution. However, dispersion from the site of injection causes the bolus to be widely spread even when the perfusion is high.

Both ASL and DSC techniques ca n be used in a multislice protocol, although there is a limitation to the maximum number of slices in each case. In DSC, coverage is given by a compromise between the number of slices and the time sampling resolution. For typical repetition time values (TR) of 1-2 s, a coverage of 10 to 15 slices can be achieved using EPI. In ASL, the maximum number of slices is limited by arrival times and the relaxation of the endogenous tracer. Typically a coverage of 5 to 10 slices can be obtained depending on the

spatial resolution, yet we get 19 slices. Another possibility for the whole brain coverage is 3D image acquisition [81, 82], though the spatial resolution tends to be reduced.

3.0 A MODEL OF MAGNETIZATION TRANSFER IN SINGLE-COIL CASL

3.1 INTRODUCTION

The magnetization of macromolecular protons cannot be easily measured directly with MRI since the T_2 of the macromolecules in biological tissues is too short (i.e. less than 1 ms). However, the magnetization of macromolecular spins can be transferred to the free water spins through the exchange of magnetization by either chemical exchange or cross-relaxation. As shown in Fig. 2.3, one can choose to saturate the macromolecular spins by using off-resonance radio frequency adiabatic pulses because the macromolecular spins have a much broader line shape than the free water spins. Only macromolecular spins are saturated and further their magnetization is transferred to the water spins which can be detected with MRI.

Single-coil CASL techniques employ the same RF coil for labeling and imaging. Examples include the traditional single-slice Alternating Proximal and distal Irradiation (APDI) [45], multi-slice Simultaneous Proximal and Distal Irradiation (SPDI) [60], and multi-slice CASL with Alternating single adiabatic inversion (SAI) label and double adiabatic inversion (DAI) control irradiations (ASD) [61] (see Fig. 2.3). Although there are some variances about the design of their label and control sequences, all of them suffer off-resonance saturation effects from the RF pulses employed for the label and control sequences.

The off-resonance saturation causes the loss of MRI control and label signals, on which quantification of perfusion is based. Therefore the signal difference of control and label images includes both perfusion and residual MT signals. The MT effects must be quantified and accounted for to permit accurate quantification of perfusion.

A quantitative analysis of off-resonance saturation has been developed by a number of investigators using a two-pool model consisting of a free water pool and a semi-solid macromolecular pool with restricted mobility. Various line shapes have been used to describe the absorption probability of the semi-solid pool: Lorentzian [83], Gaussian [55], superLorentzian [56], "Kubo-Tomita" [84, 85] and a flexible line shape [86]. Each line shape was shown to have quantitative correspondence to experimental measurements.

In previous *in vitro* MT experiments [55, 56, 86], off-resonance irradiation was applied using a long continuous wave irradiation (~ 7 s) to ensure a steady state. For practical *in vivo* imaging experiments, the continuous-wave irradiation is not yet widely available because imaging RF transmitters are currently designed for pulsed RF, not continuous, operation. Pulsed off-resonance irradiation is necessary because of limitations in RF driver performance to keep the power deposition (SAR) within acceptable limits. MT effects with pulsed RF irradiation were also studied [87].

In CASL experiments, the off-resonance adiabatic RF pulses are used in conjunction with a gradient to label the inflowing blood spins. The pulses saturate the macromolecules based on their resonance offset from the labeling plane. The RF pulses cannot be performed continuously due to hardware limitations and therefore a pulse RF train with high duty cycle (~90%) was achieved in our experiments. The duration of the RF train (3.7 s) may be too short to reach the steady state. Therefore, off-resonance saturation effects associated with CASL have to be

characterized separately since saturation is heavily dependent on the specific details of the pulse sequence and scanner imaging hardware.

3.2 THEORY

A tissue may be modeled by a pair of proton spin pools, named as pool A and B. Pool A is a free water pool. Pool B is a semi-solid macromolecular pool. Pools A and B interact via dipole-dipole interaction. These coupled pools can be described by the set of Bloch equations in the presence of an RF field [83]:

$$\frac{dM_z^a}{dt} = (R_a + R_{ba})(M_0^a - M_z^a) - \frac{R_{ba}}{f}(M_0^b - M_z^b) + \omega_1 M_y^a \tag{3.1}$$

$$\frac{dM_z^b}{dt} = (R_b + \frac{R_{ba}}{f})(M_0^b - M_z^b) - R_{ba}(M_0^a - M_z^a) + \omega_1 M_y^b \tag{3.2}$$

$$\frac{dM_x^{a,b}}{dt} = -\frac{M_x^{a,b}}{T_{2a,b}} - 2\pi\Delta M_y^{a,b} \tag{3.3}$$

$$\frac{dM_y^{a,b}}{dt} = -\frac{M_y^{a,b}}{T_{2a,b}} - 2\pi\Delta M_z^{a,b} + \omega_1 M_z^{a,b} \tag{3.4}$$

where $M_0^{a,b}$ is the equilibrium longitudinal magnetization in the absence of any RF field from pools A and B respectively. $M_{x,y,z}^{a,b}$ are the x, y, z components of the magnetization of pools. $T_{2a,b}$ is the transverse relaxation time. $R_{a,b}$ is the longitudinal relaxation rate ($1/T_{1a,b}$). R_{ba} is a pseudo-first-order cross-relaxation rate constant from pool B to pool A. ω_1 is the amplitude of off-resonance saturation pulse. Δ is the frequency offset of saturation pulse. f is the ratio of the number of B spins and the number of A spins. The steady-state solution gives a Lorentzian line

shape for both free water and macromolecular pools. The experiment was demonstrated in samples of bovine serum albumin [83].

Henkelman et al., [55] modified the model by keeping the model symmetric with respect to the two pools. Noticing $R_{ab} = R_{ba}/f$ and $f = M_0^b/M_0^a$, we know that $R_{ba}/R_{ab} = M_0^b/M_0^a$. So Henkelman et al. introduced a fundamental rate constant R such that $R_{ba} = RM_0^b$ and $R_{ab} = RM_0^a$. Therefore (3.1) and (3.2) can be written symmetrically as:

$$\frac{dM_z^a}{dt} = R_a(M_0^a - M_z^a) - RM_0^b M_z^a + RM_0^a M_z^b + \omega_1 M_y^a \tag{3.5}$$

$$\frac{dM_z^b}{dt} = R_b(M_0^b - M_z^b) - RM_0^a M_z^b - RM_0^b M_z^a + \omega_1 M_y^b \tag{3.6}$$

The steady state solution was solved by making all time derivatives equal to zero of Eq. (3.6) - (3.9). By noting that $(2\pi\Delta T_{2a}) >> 1$, the solution can be simplified as:

$$M_z^a = \frac{R_b[\frac{RM_0^b}{R_a}] + R_{rfb} + R_b + R}{[\frac{RM_0^b}{R_a}](R_b + R_{rfb}) + (1 + (\frac{\omega_1}{2\pi\Delta})^2[\frac{1}{R_a T_{2a}}])(R_b + R_{rfb} + R)} \tag{3.7}$$

where:

$$R_{rfb} = \frac{\omega_1^2 T_{2b}}{1 + (2\pi\Delta T_{2b})^2} \tag{3.8}$$

As seen from Eq. (3.8), the pool B is of Lorentzian line shape. However, they showed that a Lorentzian line shape is not adequate to describe their MT data acquired from agar gel. They proposed a Gaussian line shape for pool B:

$$R_{rfb} = \omega_1^2 \sqrt{\pi/2} T_{2b} e^{-\frac{(2\pi\Delta T_{2b})^2}{2}} \tag{3.9}$$

The Gaussian line shape was shown to agree well with their agar gel data. Morrison et al., found the superLorentzian line shape can adequately describe the *in vitro* MT data of the tissues from bovine:

$$R_{rfb} = \omega_1^2 \int_0^{\frac{\pi}{2}} d\theta \sin\theta \frac{\sqrt{2\pi} T_2}{3\cos^2\theta - 1} e^{-2\left[\frac{2\pi\Delta T_2}{3\cos^2\theta - 1}\right]^2} \qquad (3.10)$$

However, Li et al., showed that a nonparametric flexible line shape improves the fits noticeably by using the same bovine tissues. All these methods utilized steady state off-resonance continuous wave (CW) saturation techniques with variable offset saturation frequencies and amplitudes.

Due to the restriction of specific absorption rate (SAR) and the inability to generate CW irradiation on most clinical scanners, this technique is difficult to implement *in vivo* for humans. Holt et al. [88], proposed off-resonance pulsed irradiation. However, the steady-state Bloch model does not provide an adequate theoretical description of pulsed MT. A general mathematical description of the time-dependent pulsed MT was proposed, but the data processing was very complicated.

Sled and Pike developed [87] an approximated signal equation for a spoiled gradient-echo imaging sequence. Sled and Pike [57] demonstrated this method in uncooked beef and *in vivo* in human. The superLorentzian yielded a close fit compared to Gaussian or Lorentzian line shape for their uncooked beef experiment. The superLorentzian line shape is then used to derive parameters for in vivo measurements. However, the experiment protocol includes a large number of MT-weighted scans and time-consuming acquisitions. Moreover, the model still remains complicated since it requires a numerical solution of the Bloch equations to estimate a direct saturation.

Our CASL experiment utilized off-resonance saturation using pulsed trains. We derive the CASL-related non-steady state model from the Eq. (3.3) - (3.6). The pulse duration of our CASL experiments was 3.7 s, which is equal to more than 3 times T_1 (approximately 1 s) of Gray matter, but more than 5 times T_2 (approximately 100 ms) of Gray matter. The transverse magnetization should be in the steady state; the longitudinal magnetization may not reach the steady state. Therefore, we need to introduce two constant, (C_a and C_b) to describe the instantaneous longitudinal relaxation rate.

For transverse steady state, the time derivatives from Eq. (3.3) and (3.4) must be zero. We can express M_y^a and M_y^b by M_z^a and M_z^b respectively. From the assumed longitudinal relaxation rate, we replace the above obtained expression of M_y^a and M_y^b into Eq. (3.5) and (3.6) :

$$C_a = R_a(M_0^a - M_z^a) - RM_0^b M_z^a + RM_0^a M_z^b - \frac{\omega_1^2 T_{2a}}{1+(2\pi\Delta T_{2a})^2} M_z^a \qquad (3.11)$$

$$C_b = R_b(M_0^b - M_z^b) - RM_0^a M_z^b + RM_0^b M_z^a - \frac{\omega_1^2 T_{2b}}{1+(2\pi\Delta T_{2b})^2} M_z^a \qquad (3.12)$$

M_z^a can be solved by eliminating M_z^b:

$$\frac{M_z^a}{M_0^a} = \frac{R_b RM_0^b - RC_b + (R_{rfb} + RM_0^a + R_b)(R_a - \frac{C_a}{M_a^0})}{(R_a + R_{rfa})(R_{rfb} + RM_0^a + R_b) + RM_0^b(R_b + R_{rfb})} \qquad (3.13)$$

where:

$$R_{rfa} = \frac{\omega_1^2 T_{2b}}{1+(2\pi\Delta T_{2b})^2}, R_{rfb} = \frac{\omega_1^2 T_{2b}}{1+(2\pi\Delta T_{2b})^2} \qquad (3.14)$$

For the comparison of parameters, we simplify the Eq. (3.13) by using $(2\pi\Delta T_{2a}) >> 1$ condition and replacing the parameters by $\widetilde{M}_0^b = \frac{M_0^b}{M_0^a}$ (relative magnetization) and $\widetilde{R} = RM_0^a$:

$$\frac{M_z^a}{M_0^a} = \frac{R_b\left[\frac{\tilde{R}\tilde{M}_0^b}{R_a}\right] - \tilde{R}\left[\frac{C_b}{R_a M_0^a}\right] + (R_{rfb} + \tilde{R} + R_b)(1 - \left[\frac{C_a}{R_a M_0^a}\right])}{(R_{rfb} + \tilde{R} + R_b)(1 + (\frac{\omega_1}{2\pi\Delta})^2\left[\frac{1}{R_a T_{2a}}\right] + \left[\frac{\tilde{R}\tilde{M}_0^b}{R_a}\right](R_{rfb} + R_b)} \qquad (3.15)$$

There are seven parameters to be determined: $\tilde{R}$, R_b, RM_0^b / R_a , $1/R_aT_{2a}$, T_{2b}, $C_a/R_aM_0^a$ and $C_b/R_aM_0^a$.

To account for the use of a pulse train, we defined the CW power equivalent amplitude of the MT pulse, which is equal to the mean saturating power of a pulse [58, 89].

3.3 MATERIALS AND METHODS

All data were acquired using a 1.5 T GE Signa system (Milwaukee, WI, LX). The GE quadrature head coil was used for labeling as well as image acquisition. Human subjects were scanned in accordance with approved Institutional Review Board (IRB) protocols after providing informed consent and passing MRI screenings. MT measurements were acquired in healthy normal volunteers (ages 20-50).

Off-resonance saturation measurements: A modified CASL sequence was used to measure off-resonance saturation (Fig. 3). Because of hardware limitations associated with the clinical scanner (e.g., RF amplifier and transmit/receive switch), the irradiations were applied using a train of 44 pulses, each pulse with an 85 ms period and 93% duty cycle for AM frequencies 0 and 125 Hz. The maximum input RF amplitude was limited to 51 mG.

Except where noted, each off-resonance RF excitation was followed by the same 15 slice echo planar imaging (EPI) acquisition (64×64 matrix, 20 cm FOV, 5 mm thick, 0 spacing, MinFull (28 ms) TE, 62.5kHz receiver bandwidth (rBW), 1 s acquisition time, 90^0 Flip angle), with a sequential superior to inferior slice acquisition order. A 100 ms delay was placed between the off-resonance saturation and image. In this research, slice 1 corresponds to the superior slice; slice 15 corresponds to the inferior slice.

Off-resonance saturation was characterized using three experiments described below. First, the dependence of the z-spectra on B_1 was measured using variable RF amplitudes and offset frequencies (250 Hz - 17 kHz) to simulate APDI (f_{AM}=0) and DAI (f_{AM}=125 Hz) RF waveforms. Images were also acquired without off-resonance saturation for normalization of the MT data. A minimum of 15 repetitions was acquired for each frequency and amplitude. A different individual was used to characterize each f_{AM} because each exam typically lasted 90 minutes (including structural images, and T_1 and B_1 maps). A strong crushing gradient was used to eliminate any residual transverse magnetization between repetitions.

B_1 maps: Multi-slice B_1 map data were acquired for the image slices using EPI (8 s TR and MinFull 28ms TE, 62.5 kHz rBW) with varying nutations (20 different input flip angles varying from 18-189^0 in increments of 9^0) [90]. B_1 maps were used to calibrate data acquired from the different experiments and determine the mean amplitude of the saturation RF for each image plane (designated herein as B_{1sat}).

Structural Images: Coronal T_1-weighted spoiled gradient-recalled echo (SPGR) images covering the whole brain were acquired (124 slices with Matrix: 256 × 192; 1.5 mm thick and zero spacing, MinFull TE, 25 ms TR, 24 x 18 cm FOV, 16 kHz rBW). The structural images were used in gray and white matter segmentation of the image data.

3.4 IMAGE PROCESSING AND DATA ANALYSIS

Image processing: Statistical Parametric Mapping (SPM) (Wellcome Department of Imaging Neuroscience) was used for EPI motion correction, gray and white matter segmentation, and co-registration with the SPGR images. MATLAB (The MathWorks, Inc.) programs were used to perform the statistical analysis of the EPI data.

B_1 maps: B_1 map data were fitted voxel-by-voxel to the three-parameter model:

$$M_z(\phi_j) = A + B\sin(C\phi_j) \tag{3.16}$$

using a nonlinear algorithm, where ϕ_j is the incremented nutation angle; and A, B, and C are the fitting coefficients. Each B_1 field map was converted to B_{1sat} based on the ratio of the saturating RF amplitude to the prescan calibration reference B_1, corrected for any changes in transmit gains between the RF saturation and B_1 map sequences.

Saturation curves: Saturation spectra were calculated separately for gray and white matter. For each image plane, the signal distribution was fit to a Gaussian curve to determine the mean (M_z) and standard deviation for each offset frequency, and then normalized to the mean equilibrium signal (M_0):

$$M_{z,norm}(t) = \frac{M_z(t)}{M_0(t)} \tag{3.17}$$

All of the saturation curves were corrected for signal increases caused by T_1 relaxation that occurred during the delay between off-resonance saturation and image slice acquisition using:

$$M_{z,norm}(\tau) = 1 - \left[\left(1 - M_{z,norm}(\tau + w + t_{acq})\right)e^{\frac{w+t_{acq}}{T_{1t}}}\right] \tag{3.18}$$

where τ is the RF saturation period, *w* is the post-saturation delay, t_{acq} is the acquisition time with respect to the beginning of the acquisition window, and T_{1t} is the relaxation time of the tissue (1.065 and 0.800 s for gray and white matter, respectively, based on our 1.5 T brain studies).

Equation (3.15) was fitted to the experimental results using a least squares technique. A set of seven parameters (R_b, T_{2b}, $\tilde{R}$, $[RM_0^b/R_a]$, $[1/R_aT_{2a}]$, $C_a/R_aM_0^a$ and $C_b/R_aM_0^a$) can be obtained. Henkelman et al., suggested that parameter R_b be fixed since R_b is insensitive to the residual sum of squares and its accurate value cannot be determined. The parameter was also fixed in our work to save the time of fitting for an unnecessary parameter ($R_b = 1\ s^{-1}$).

One off-resonance irradiation power measurement was not sufficient for uniquely determining the fitting parameters for the model. The experiment was performed at three different irradiation amplitudes $\omega_1/2\pi$ (78Hz, 110Hz and 156Hz for APDI, 128Hz, 181Hz and 256Hz for DAI). For CASL, irradiation amplitudes of ~110Hz for APDI and ~180Hz for DAI are typically used. We used 12 different offset frequencies Δ, distributed from 0.25 to 15 kHz. We performed a global fit to Equation (3.14) of each data set with 12 different offset frequencies and 3 irradiation powers with the superLorentzian, Gaussian, and Lorentzian line shapes. Unique sets of seven model parameters cannot be obtained from the experimental data. However, for each initial value of the pair of (C_a, C_b), unique sets of five model parameters can be determined. Each initial value of (C_a, C_b) reaches a local minimum. The right initial value of pair (C_a, C_b) would lead to the minimum average residual deviation from the experimental data. Therefore, we chose the initial value of pair (C_a, C_b) that minimizes the average residual deviation for a global fit.

Quality of the fit was evaluated as the average residual deviation per point between the fit and experiment, $\sigma = \sqrt{ssq/N}$ [86] (where ssq is the sum of squares, N is the number of data points).

The error of fitted parameters was determined by finding the maximum and minimum value of the parameters for an increase of 1 in χ^2, while keeping all other parameters fixed [91].

3.5 RESULTS & DISCUSSION

Average residual derivation σ values for the fits to the two-pool model using superLorentzian, Gaussian and Lorentzian line shapes are shown in Table 3.1. For both gray and white matter with different RF waveforms, the average residual deviation with the Lorentzian fit is reduced 60% compared with the Gaussian fit, and 92% compared with the superLorentzian fit. The average residual deviation (average 0.0125) from the parametric fit is comparable with the best reported value from nonparametric fit (average 0.013) [86]. Figure 3.2 shows the comparison of representative fits (human gray matter saturation curve at f = 0 Hz) using the superLorentzian, the Gaussian, and the Lorentzian line shapes. The fits with superLorentzian line shape deviate significantly from the experiment. The Gaussian line shape does not result in as good a fit as the Lorentzian line shape. There is overall improvement in the fit using Lorentzian line shape compared with either the Gaussian or superLorentzian line shape.

For steady-state off-resonance continuous-wave irradiation, researchers have suggested that the Gaussian line shape is appropriate for solids and gels [55]; superLorentzian is suitable for tissues [56]. However, Li et al., suggested a non-parametric flexible line shape because the average behavior of a variety of macromolecular types may not be adequately represented by any analytical line shape. Another disparity between our study and previous studies is that we used all gray and white matter tissues from one axial slice instead of sampling several points or

drawing a region. The heterogeneity of the gray and white matter will affect the line shape of the semi-solid pool.

Both Tozer et al. [58] and Ramani et al. [89], reported that the Gaussian line shape provides a superior fit than the superLorentzian for the tissue off-resonance non-steady state (14.6 ms MT pulse) saturation data in their pulsed RF sequence. They indicated that the tissue off-resonance saturation may have different line shapes for different pulse sequences and imaging hardware. The non-steady state may affect the line shape of off-resonance saturation.

Figure 3.3 shows the fit of gray matter and white matter saturation data of human brain for APDI and DAI RF waveforms to the two-pool model with a Lorentzian line shape for the semi-solid pool. The two-pool model with Lorentzian line shape for the semi-solid pool is very good for even different RF waveforms. All the fitted parameters for the gray and white matter at two different modulation frequencies are shown in Table 3.2.

The differences of parameters between APDI and DAI further prove that the off-resonance saturation is also heavily sequence-dependent, as we mentioned in the introduction. The values of $C_a/R_aM_0^a$ and $C_b/R_aM_0^a$ less than 10^{-6} indicate that the saturation pulse achieves a condition very close to the steady state. We compared the average residual derivation σ by setting both $C_a/R_aM_0^a$ and $C_b/R_aM_0^a$ to zero. The average residual derivation σ only increases 1.6% for the RF saturation data of white matter at f = 125 Hz if we set both $Ca/R_aM_0^a$ and $C_b/R_aM_0^a$ to zero. We cannot assert whether these two parameters are truly zeros or not. The T_2 times for the gray and white matter semisolid pools are short (~40 μs), and are in the range of T_2 that was measured by Tozer et al. for tissue white matter (18 μs) [58] and reported by Caines et al. for rat muscle (58 μs) [92]. The values of $1/R_aT_{2a}$ of white matter are in the range of $1/R_aT_{2a}$ measured by Sled and Pike for white matter tissue [57](16) and reported by Tozer et al. for white

matter tissue (44) [58]. The values of RM_0^b/R_a for gray and white matter are in the range [1.7-3.5] and [1.5-3.7] respectively, calculated within the error range [57]. The exchange rate R of the saturation data ($f = 0$) is also comparable to those measured for human gray matter ($33\,s^{-1}$) and white matter ($27\,s^{-1}$) [57]. The heterogeneity of the gray and white matter from the large region of interests will contribute to the variance of the parameters.

The CASL MT Lorentzian model offers us the ability to calculate the off-resonance saturation effects for different frequency offsets corresponding to each slice. The pure perfusion signal can be separated from the signal difference between the control and label images. The signal from the control images can also be compensated back to the original signal for the signal drop from the CASL off-resonance saturation model. The detailed compensation formula is list on Equation (5.16). Therefore, the quantification of perfusion will be improved by predicting off-resonance saturation effects for each of our experiments.

Table 3.1. Essential particles Average residual derivation σ for the best fits using superLorentzian, Gaussian, Lorentzian line shape for the semi-solid pool

Data Source	SuperLorentzian σ	Gaussian σ	Lorentzian σ
Gray matter at $f = 0$ Hz	0.15	0.030	0.0124
White matter at $f = 0$ Hz	0.15	0.034	0.0124
Gray matter at $f = 125$ Hz	0.16	0.030	0.0140
White matter at $f = 125$ Hz	0.14	0.034	0.0111

Table 3.2. Parameters for the Fit of Eq.[3.14] to the magnetization transfer data.($R_b = 1s^{-1}$)

	$T_{2b}(\mu s)$	$R(s^{-1})$	$\frac{RM_0^b}{R_a}$	$\frac{1}{R_a T_{2a}}$	$\frac{C_a}{R_a M_0^a}$	$\frac{C_b}{R_b M_0^b}$	σ
Gray at f = 0 Hz	34.2 ± 1.0	31.9 ± 0.6	2.44 ± 0.04	28.3 ± 1.2	$<10^{-6}$	$<10^{-6}$	0.0124
White at f = 0 Hz	41.6 ± 1.1	28.4 ± 0.5	3.02 ± 0.04	28.1 ± 1.4	$<10^{-6}$	$<10^{-6}$	0.0124
Gray at f = 125 Hz	34.1 ± 1.2	45.1 ± 1.0	1.90 ± 0.03	15.3 ± 0.8	$<10^{-6}$	$<10^{-6}$	0.0140
White at f = 125 Hz	44.8 ± 1.1	46.7 ± 1.1	2.69 ± 0.04	17.6 ± 1.0	1.8×10^{-6}	1.9×10^{-6}	0.0111

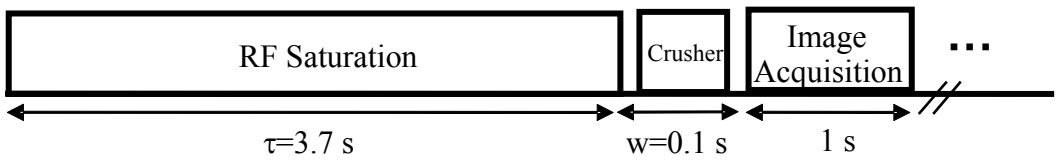

Figure 3.1. Saturation Pulse Sequence and Timing. Crushers are applied after the RF saturation during the delay.

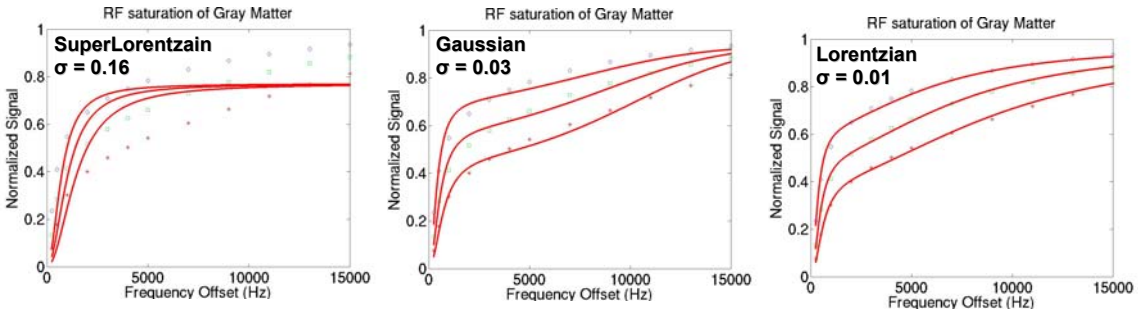

Figure 3.2. RF saturation data and fits for human gray matter at f = 0 Hz. Data are shown for three different RF amplitudes ($\omega_1/2\pi$ =78Hz (◊), 110Hz (□), 156Hz (*) Hz) and 12 different offset frequencies. (a) The data fitted to Eq. (3.14) with a superLorezian line shape; (b) the same data fitted with a Gaussian line shape (c) the same data fitted with a Lorezian line shape for the semi-solid pool. The average residual deviations per point (σ) are 0.16, 0.03, and 0.01, respectively, for the three fits.

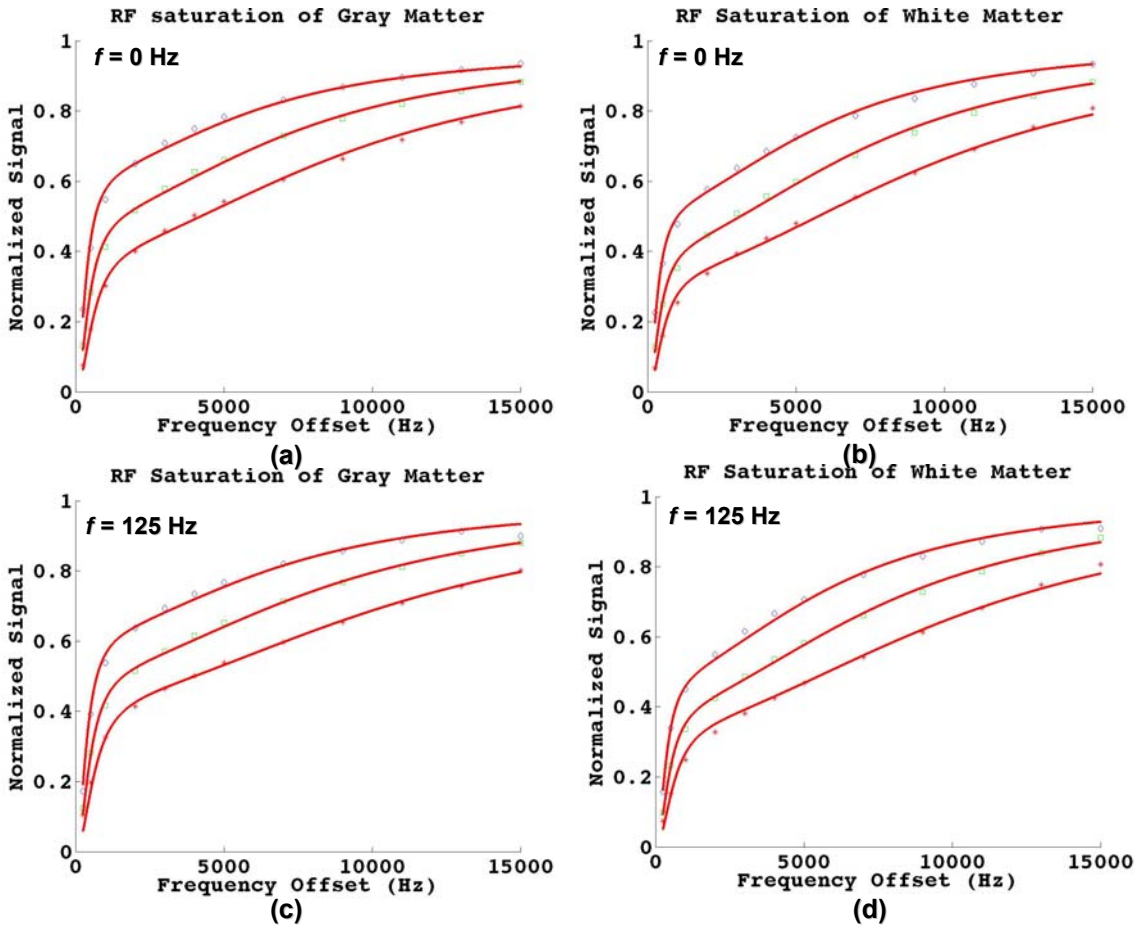

Figure 3.3. (a) RF saturation data and fits for human (a) gray matter at f = 0 Hz; (b) white matter at f = 0 Hz; (c) gray matter at f = 125 Hz; (d) white matter at f = 125 Hz. Solid red lines result from a global fit to Eq. (3.14) with the Lorentzian line shape for semi-solid pool. In graphs (a) and (b), the marked points are the data for three different RF amplitudes ($\omega_1 / 2\pi$ =78Hz (◊), 110Hz (□), 156Hz (*) Hz) and 12 different offset frequencies. In graphs C and D, the marked points are the data for three different RF amplitudes ($\omega_1 / 2\pi$ =128Hz (◊), 181Hz (□), 256Hz (*) Hz) and 12 different offset frequencies.

4.0 A SIMPLE MODEL OF CASL INVERSION EFFICIENCY

4.1 BACKGROUND

Multi-slice continuous arterial spin labeling (CASL) using ***A***lternating single adiabatic inversion (***S***AI) label and double adiabatic inversion (***D***AI) control acquisitions (ASD) has become a valuable noninvasive technique for measuring cerebral perfusion in the normal and diseased brain [61, 62, 93-95]. The advantages of ASD are: 1) the technique uses conventional hardware (i.e., single RF head coil) and is simple to employ in a clinical setting and 2) its residual magnetization transfer (MT) characteristics permit the perfusion in the entire cerebrum to be sampled. However, one disadvantage of ASD is that the DAI control suffers from inefficiencies that reduce the perfusion signal-to-noise ratio (SNR) [62, 63] relative to conventional single-slice CASL using alternating proximal and distal irradiations (APDI) (i.e., SAI label and control acquisitions) [45] or multi-slice simultaneous proximal and distal irradiation (SPDI) [60].

Two published studies have considered the improvement of the efficiency of the DAI control by computer simulations of the Bloch equations. One focused on assessing the influence of each pulse parameter (RF pulse amplitude, B_1; phase, φ and frequency, f), spin velocity, and spin relaxation on the performance of DAI control [96]. However, no quantitative measurement or verification was provided for the derivation of optimal parameters. The other work [97] introduced a dimensionless parameter α, which is obtained from the labeling parameters (RF

gradient strength G, RF pulse amplitude B_1, and frequency f) and the flow velocity. The parameter provided a simple measurement for distinguishing three separate regimes, each characterized by a different magnetization trajectory, and therefore gained extra insight to derive optimal parameters for the DAI control. However, Utting et al., [96] pointed out that unless $f > 2\pi B_1$, φ determines the performance of the DAI control, but this relation has not been included in the optimization of parameters. Therefore, more adequate measurements may be needed for the optimization of DAI control.

The efficiencies for the SAI label and DAI control are required in calculating absolute perfusion rates from the CASL signals. Currently, there is no standard method for estimating the DAI efficiency specific to each experiment. Previously, researchers cited relative ASD and APDI efficiencies from earlier *in vivo* measurements, without compensation for varying clinical conditions. Given that DAI and SAI planes tend to lie in the inhomogeneous region of the RF head coil for brain studies, the actual DAI and SAI efficiencies may vary significantly between subjects. Relative efficiencies based on comparing ASD and APDI signals are subject to significant errors from MT asymmetry [64] and residual MT gradients associated with APDI.

Accurate *in vivo* measurements of absolute adiabatic inversion efficiency are challenging because of the small arterial lumen size, the presence of pulsatile flow, and the need to minimize the exam time. Simulations based on the Bloch equations have been employed for SAI [98-100] and DAI [96, 97] based on adiabatic fast passage (AFP) but implementation is time-consuming and may not adequately describe the behavior of in vitro or in vivio experiments. Instead, simple models for inversion efficiencies are desirable. The efficiency of SAI has been previously measured and modeled using the simple Zhernovoi model [101, 102]. Herein, we extend the Zhernovoi model

to DAI. The primary advantage of these models over relative measurements is the ability to calculate the absolute inversion efficiency for each experiment with minimal scan time.

4.2 THEORY

ASD and APDI use a constant amplitude adiabatic RF envelope for SAI. The envelope for the DAI control is amplitude-modulated at a low frequency (f_{AM} < 500 Hz), thus creating two closely spaced sidebands separated in frequency by $2f_{AM}$, with each sideband receiving half of the envelope's amplitude. The envelope for SPDI is amplitude modulated at a high frequency (f_{AM} > 10 kHz) to create two widely spaced sidebands, one of which is typically used for SAI. These waveforms are further modulated at the desired Larmor frequency to adiabatically invert the arterial blood as it passes through the prescribed inversion region(s). The labeling field amplitudes at the respective inversion region will depend on the B_1 distribution of the coil, the input SAI and DAI RF amplitude settings, and the RF transmit gain.

4.2.1 DAI Efficiency

For a single inversion region, the adiabatic condition for a spin moving at velocity v, is:

$$\frac{1}{T_1}, \frac{1}{T_2} << \frac{\vec{G}_l \bullet \vec{\mathrm{v}}}{B_l} << \gamma B_l \qquad (4.1)$$

where B_l is the labeling RF amplitude measured at the inversion region (designated herein as B_{lSAI} for SAI and B_{lDAI} for DAI), G_l is the labeling gradient amplitude, T_1 and T_2 are the respective spin-lattice and spin-spin relaxation times, and γ is the spin gyromagnetic ratio. The

root-mean-square (rms) amplitudes of the SAI label and DAI control should be equal to minimize residual MT in the imaging volume [46, 61]. Therefore, $B_{lDAI} = B_{lSAI}/\sqrt{2}$ for each of the two DAI inversion regions.

Previously, we presented a general expression for the mean inversion efficiency in AFP based on Zhernovoi [102, 103]:

$$\langle \alpha \rangle = 1 - e^{-\frac{\pi \beta'}{2}} \tag{4.2}$$

where β' is the effective adiabaticity factor based on the mean flow velocity <v> measured across the channel or artery:

$$\beta' = \frac{\gamma B_l^2}{\vec{G}_l \bullet \langle \vec{v} \rangle} \tag{4.3}$$

In general, the relationship between the final (M_f) and initial (M_i) magnetic moment associated with one or more inversions is:

$$M_f = M_i \prod_{j=n} w_j \left(1 - 2\langle \alpha_j \rangle\right) \approx M_i \left(1 - 2\langle \alpha \rangle\right)^n \tag{4.4}$$

where α_j is the inversion efficiency for each inversion indexed by j, w_j is a weighting factor that accounts for relaxation and other losses that occur between successive inversions, n is the number of inversions [typically n=1 for SAI, n=2 for DAI for steady or biphasic (positive velocity) flow]. The approximation (right side of equation) assumes minimal losses between inversions (w_j = 1) and a constant efficiency ($\alpha_j = \alpha$). These assumptions may not hold for cycled RF pulse trains (i.e., duty cycle less than 100%), fluids with short relaxation times relative to the inversion time [98], insufficient distance between inversion sites, or triphasic flows (containing positive and negative velocities).

Our simple model assumes that DAI is simply two successive adiabatic inversions, each with inversion efficiency α_C. The efficiency of DAI is then given by:

$$\langle \chi \rangle = 1 - 2\langle \alpha_C \rangle + 2\langle \alpha_C \rangle^2 \qquad (4.5)$$

Note that the definition of efficiency is different between SAI and DAI. The SAI efficiency (α) represents the ratio of inverted spins to the equilibrium magnetization. The DAI efficiency (χ) represents the ratio of uninverted spins to the equilibrium magnetization. The SAI and DAI efficiencies do not include relaxation between the inversion and imaging regions. For other CASL techniques (e.g., APDI, SPDI, or decoupled labeling and imaging coils [104]) that do not suffer from control inefficiencies, α_C is 0 and χ is 1.

4.2.2 Calculation of Aggregate Efficiency for CASL

Using Equation (4.4), the aggregate efficiency for CASL with SAI label and DAI control is:

$$\alpha_{eff} = \frac{M_{DAI} - M_{SAI}}{2M_e} \approx 2\left(\alpha_c^2 - \alpha_C\right) + \alpha_L \qquad (4.6)$$

where α_L is the inversion efficiency of the SAI label, and α_C is the inversion efficiency of each DAI labeling site (sideband).

The labeling field (B_l) can be measured *in vivo* using the B_1 map sequence described above in less than 3 minutes. The B_1 field map is converted to B_{lSAI} and B_{lDAI} based on the ratio of the SAI and DAI labeling amplitudes to the prescan calibration reference B_1, corrected for any changes in transmit gains between the CASL and B_1 map sequences. B_l should be measured in the labeling plane adjacent to the artery, not inside the lumen, to avoid flow-induced errors.

The arterial velocities can be measured using a commercial phase contrast (PC) Cine velocity mapping sequence, with a scan time under 30 seconds. The image plane should be co-planar to the labeling plane, preferably transverse to the supply arteries for effective labeling and visualization of the lumen. The sequence should measure the velocity component that is parallel to G_l. We typically acquire 20 cardiac phases using peripheral gating to sample the arterial velocity as a function of time, averaged across the vessel lumen. α_C and α_L should be calculated for each cardiac phase, and then averaged across the cardiac cycle to determine $<\alpha_{eff}>$ for the experiment.

4.2.3 DAI Amplitude Modulation Frequency

Ideally, the DAI sidebands should be spaced such that the spins can be inverted by the first sideband and uninverted by the second sideband. The spatial separation of the DAI sidebands is proportional to f_{AM} and inversely proportional to G_l. Both the spin inversion time and distance are proportional to B_l, and inversely proportional to G_l [105]. If the sidebands are spaced too close together relative to the spin inversion distance, the spins may be incompletely inverted by the first sideband and then incompletely uninverted by the second sideband. By contrast, if the sideband spacing is too large, the spins are susceptible to relaxation effects in transit between sidebands that will also prevent the spins from returning to their equilibrium state.

4.3 MATERIALS AND METHODS

All MRI experiments were conducted on a 1.5 T GE whole-body Signa LX MRI (Milwaukee, WI).

4.3.1 Phantom Experiments

The flow phantom and imaging methods used in this experiment have been previously described for similar SAI efficiency measurements [102]. The T_1 and T_2 of the flowing fluid (30 mM saline) were measured to be 2.36 s and 1.50 s, respectively.

The gradients were fixed at either 0.25 or 0.5 G/cm for both the label (herein defined using DAI RF for our experiments) and control (herein defined without adiabatic RF) to match eddy currents. The RF duty cycle was either 90 or 93% using a train of 44 pulses. Each pulse was 80 ms in duration. The center between the inversion regions was located 6 cm upstream of the axial image plane (i.e., oriented transverse to the direction of flow). No transit delay was used and only a single echo-planar image slice was acquired.

DAI efficiencies were measured in three experiments for different values of the DAI amplitude (A_C) and: 1) labeling gradient (G_l); 2) flow velocity (<v>); and 3) DAI AM frequency (f_{AM}). Note: A_C is defined herein as $2 \cdot B_{lDAI}$. We assumed that B_{lDAI} was equal between the two DAI inversion regions based on their close proximity.

For the first experiment, we maintained laminar flow with a mean velocity of 18 cm/s in the flow apparatus and used two different values of labeling gradient (0.25 and 0.5 G/cm) while varying the DAI amplitude from 0 to a maximum of 60 mG. In the second experiment, DAI efficiencies were measured for four flow velocities (mean velocities of 18, 26, 35, 44 cm/s) while

A_C was varied from 0 to a maximum of 80 mG. G_l was fixed at 0.25 G/cm. In the third experiment, the DAI efficiency was measured for four different DAI AM frequencies (62.5, 125, 250, 500 Hz) while B_{lDAI} was varied from 0 to a maximum of 65 mG. G_l was fixed at 0.25 G/cm.

B_1 maps: B_1 maps were used to calibrate data acquired from the different experiments and determine B_{lDAI} at the DAI region. Multi-slice B_1 map data were acquired for the image and DAI slices using EPI (TR: 8 s and TE: MinFull 28ms, BW: 62.5 kHz) with varying nutations (20 different input flip angles varying from 18-189^0 in increments of 9^0) [90]. B_1 map data were fitted voxel-by-voxel to the three-parameter model:

$$M_z(\phi_j) = A + B\sin(C\phi_j) \tag{4.7}$$

using a nonlinear algorithm, where ϕ_j is the incremented nutation angle, A, B, and C are the fitting coefficients. The mean B_1 for the inversion region was used to calculate β' using Equation (4.3).

Image Processing: Interactive Data Language (IDL, Research Systems, Boulder Colorado) routines were used in image processing and analysis to select the flow region of interest (ROI) and to calculate the ROI statistics. The DAI efficiency was measured by drawing a ROI within the flow tube lumen located downstream of the DAI region. The DAI efficiency was calculated as:

$$\chi_{measured} = 1 - \frac{|M_e - M_{DAI}|}{2\langle A\rangle |M_e|} \tag{4.8}$$

where the numerator is the magnitude of the complex difference between the unlabeled control (M_e) and DAI image (M_{DAI}) signals, and $<A>$ represents the fraction of the signal remaining after

T_1 relaxation during transit from the inversion regions to the measurement plane. Models for <A> were presented previously for different flows [102].

Computer Simulations: Numerical solutions of the Bloch equations including AFP were conducted using IDL in an effort to replicate the MRI results. The simulations included different values of f_{AM} (62.5, 125, 250, and 500 Hz), A_C, <v> (9 – 35 cm/s in increments of 4.5 cm/s) to replicate the dispersion in flow, and fluid relaxivities. The results were averaged over the component spin velocities.

4.3.2 In Vivo Measurements

ASD and SPDI cerebral CASL data were acquired in 28 elderly subjects after informed consent, in accordance with the University of Pittsburgh Institutional Review Board (IRB). Nineteen image slices were acquired using ramp-sampled EPI (64×64 matrix, 20 cm FOV, 5 mm thick, 0 spacing, MinFull (21 ms) TE, 1 s acquisition time, 90^0 Flip angle) after a 700 ms transit delay. The ASD irradiations were applied using a 44 pulse train with an 85 ms period and 93% duty cycle. SPDI used a 49 pulse train with a 76 ms period and 92% duty cycle. The input RF amplitude was 35 mG for SAI (ASD label), and 49.5 mG for DAI (ASD control, f_{AM} = 125 Hz) and 51 mG for SPDI (25.5 mG/sideband, f_{AM} = 15.625 kHz). ASD used a G_l of 0.25 G/cm while SPDI used a G_l of 0.37 G/cm. The label was placed 10 cm below the center of the imaging volume, superior to the common carotid bifurcation. B_l and arterial velocities were measured at the labeling planes using B_1 map and conventional phase contrast (PC) cine velocimetry sequences.

Statistical Parametric Mapping (SPM) (Wellcome Department of Imaging Neuroscience) was used for EPI motion correction, gray and white matter segmentation, and co-registration

with the high-resolution structural images. MATLAB (The MathWorks, Inc.) programs were used to determine the mean gray matter CASL signals from the central image (10^{th}) slice for the 49 difference pairs (control – label) acquired for ASD, and 11 difference pairs acquired from SPDI. Relative efficiencies were calculated using the ratio of the SPDI/ASD difference (control-label) signals. A regression analysis was performed using the ratio of the aggregate SPDI/ASD efficiencies calculated from the efficiency models using the B_1 map and PC Cine results.

4.4 RESULTS

Phantom Experiments

The dependence of the percent difference signals ($100 \cdot |M_e - M_{DAI}|/|M_e|$) on the labeling gradient is illustrated in Fig. 4.1 (top). Difference signals were converted into DAI efficiencies (χ) and plotted as a function of β' after correction for T_1 relaxation attenuation in transit from the inversion regions to the imaging plane (Fig. 4.1 bottom) [102]. In general, the DAI efficiency starts from 1 at $\beta'=0$ (when the DAI control is turned off), drops to 0.5 at $\beta'=0.5$, then rises again to a peak at $\beta' \sim 3$, and subsequently oscillates at higher β' (Fig. 4.2).

The effect of f_{AM} can be observed in Fig. 4.3. For the lowest f_{AM} (62.5 Hz), χ inflects at $\beta' \sim 2$. The peak inflection point for 125 Hz is also noticeable at $\beta' \sim 3.6$, indicating an oscillation as well. The DAI efficiency drops as f_{AM} is increased, presumably due to losses (e.g., relaxation and spin locking) that occur as the two inversion sites move apart.

The numerical solutions of the Bloch equations (Fig. 4.4) also demonstrate the oscillatory behavior of χ. The simulations grossly mimic the behavior of our experimental results only when many different velocities are averaged together.

***In Vivo* Measurements**

The *in vivo* measurements are summarized in Table 4.1. The mean ratio of the SPDI/ASD difference signals measured in the gray matter was 1.16 +/- 0.05. The mean ratio calculated from the simple efficiency models was 1.13 +/- 0.02. Analysis of variance (ANOVA) yielded a correlation coefficient of 0.974.

4.5 DISCUSSION

The experimental data verify that χ is dependent on β' (consisting of the B_{lDAI}, G_l, and <v>), and f_{AM} (i.e., the separation of inversion sidebands). Bloch equation simulations and flow phantom and *in vivo* measurements are required to further assess the effects of the following on χ [98]: RF pulse durations and duty cycles; different flow types (e.g., triphasic pulsatile flows) and velocities, fluids that simulate blood properties (T_1 and T_2 of 1.4 s and 0.24 s, respectively, measured at 1.5 T) [106]; and pulse sequence parameters (A_C, G_l, f_{AM}).

Adiabaticity

The simple model provides an excellent fit for β' less than 1, and remains accurate to within 10% for β' less than 2. Similar divergent behavior was also observed for the Zhernovoi-based model of SAI [102] for $\beta' > 3$ and was attributed to the increasing inversion time.

DAI Modulation Frequency

Our experimental data show that the values of β' at which χ inflects depends on f_{AM} for 62.5 and 125 Hz. Numerical simulations (not shown) reveal that this behavior also occurs for f_{AM} greater than 125 Hz. Therefore, the oscillating behavior of the DAI efficiency appears to be related to the separation of the sidebands and is also dependent on the inversion time for the spins. Oscillations in AFP were reported by Zhernovoi [107] to occur when the adiabatic sweep was truncated. This condition may exist for DAI in the region between the two inversion planes.

Bloch Equation Simulations

Simulations of the Bloch equations are challenging for real flows since they must address the timing of the pulse train, the characteristics of the blood flow including the dispersion in flow velocities, and the scanner performance (e.g., gradient ramps, RF phase and amplitude stability). The results of the Bloch equation simulations grossly mimic the behavior of our experimental result only when many different velocities are averaged together. So far, we have not found the Bloch equation numerical simulations to be useful in estimating either SAI or DAI efficiencies for real flows since the nonlinear equations are highly sensitive to the experimental conditions.

***In Vivo* Measurements**

The high correlation coefficient indicates good agreement between relative efficiencies measured in the brain and the efficiency models. Therefore, the models provide a valuable and simple method to calculate the experimental inversion efficiencies with less error and time associated with alternative techniques. The aggregate efficiency calculated from Equation (4.6) for 60 elderly subjects can vary from 0.4597 to 0.9973 with mean 0.8392 and deviation 0.1106 (which is 13% of the mean). This further verifies that inversion efficiencies between subjects vary significantly.

In conclusion, the DAI model derived from AFP provides a reasonable estimate of our flow phantom data for $\beta'<2$, and a good estimate of relative *in vivo* efficiencies. Therefore the model can be used to calculate the absolute inversion efficiency for the quantification of absolute perfusion rate of each CASL experiment. The model does not distinguish between f_{AM}, duty cycle, pulse duration, and fluid flow and relaxation properties. Nevertheless, no other simple DAI efficiency model has yet been proposed.

Two other studies based on computer simulations investigated the DAI efficiency to improve the performance of the DAI control. One study [96] investigated the dependence of DAI control on each pulse sequence parameter, spin velocity and spin relaxation. It was found that unless $f > 2\pi B_1$, φ determined the performance of the DAI control. The other study [97] introduced a dimensionless parameter α, which divides magnetization trajectory into three separate regimes. By taking advantage of this phenomenon, they derive optimal parameters for the DAI control. However, conflicts appear between these two investigations: the dominance of phase φ to the AM control (if $f < 2\pi B_1$) is not accounted for in the second optimization parameters α and $\beta_{1/2}$, which indicates that the optimization strategy may not be adequate in some conditions.

Our experimental design for the parameters of CASL is near optimal efficiency according to the optimization strategy [97]. It was pointed out that the assumed inversion efficiency (0.7 and 0.8) overcompensates rCBF in some animals, which indicates the necessity of measuring the inversion efficiency in an individual basis [96]. An inconsistency was reported regarding the predicted magnetization between our model and their computer model. However, computer simulations of Bloch equation only grossly mimic the behavior of our experimental results as we reported. Therefore, the *in vivo* application of the computer model still needs further investigation.

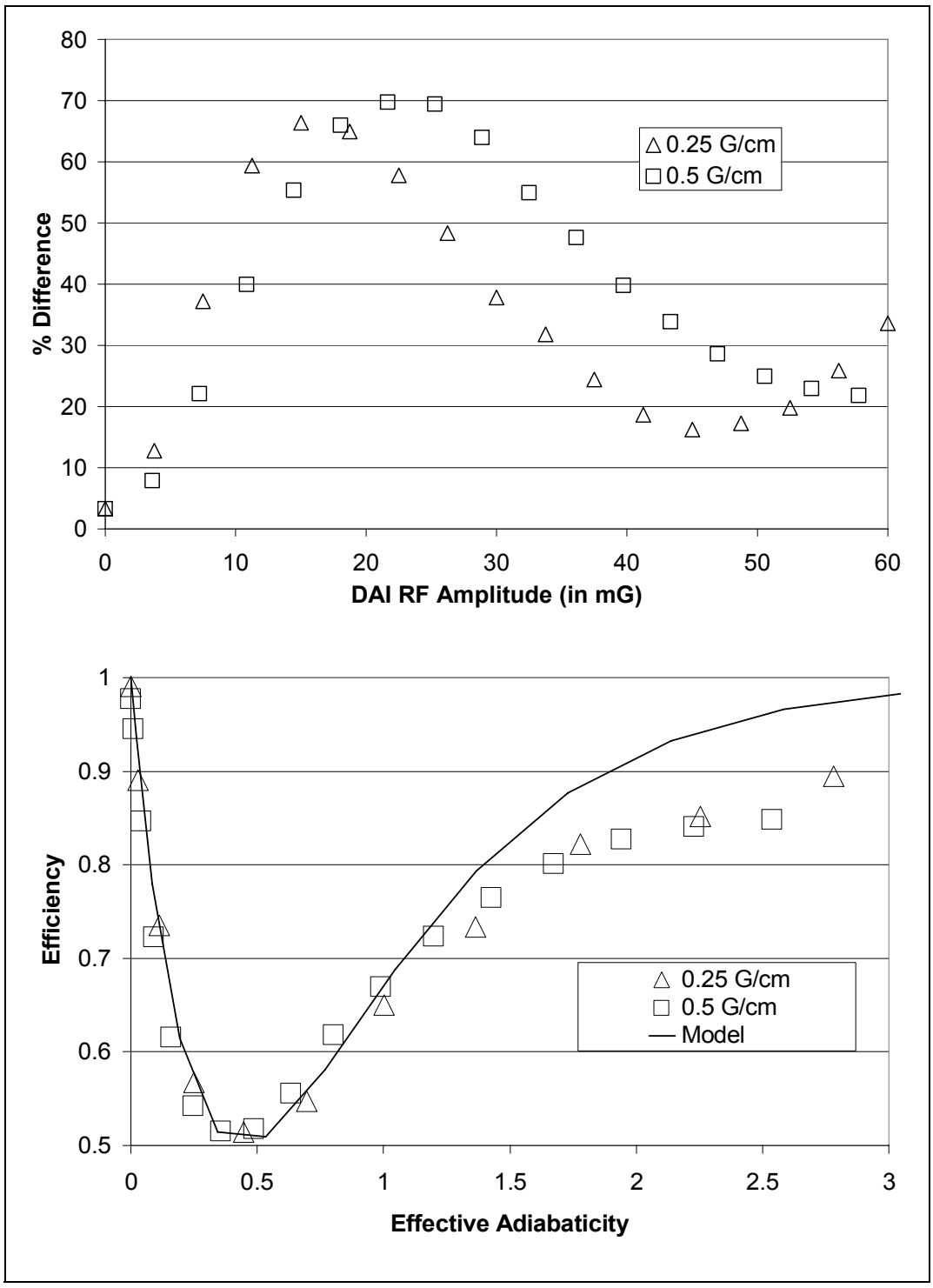

Figure 4.1. Experimental DAI data measured for a Gl of 0.25 and 0.5 G/cm illustrates the advantage of lower labeling gradients for minimizing B_1. The flow had a mean velocity of 18 cm/s. The percent differences between the unlabeled and DAI images are plotted versus A_C (top). Oscillation of the difference signal (for 0.25 G/cm) is apparent from the second inflection

point at A_C ~ 45 mG. The resulting DAI efficiencies (χ) are plotted versus the effective adiabaticity (β' < 3) (bottom). f_{AM} was 125 Hz with a RF duty cycle of 90%.

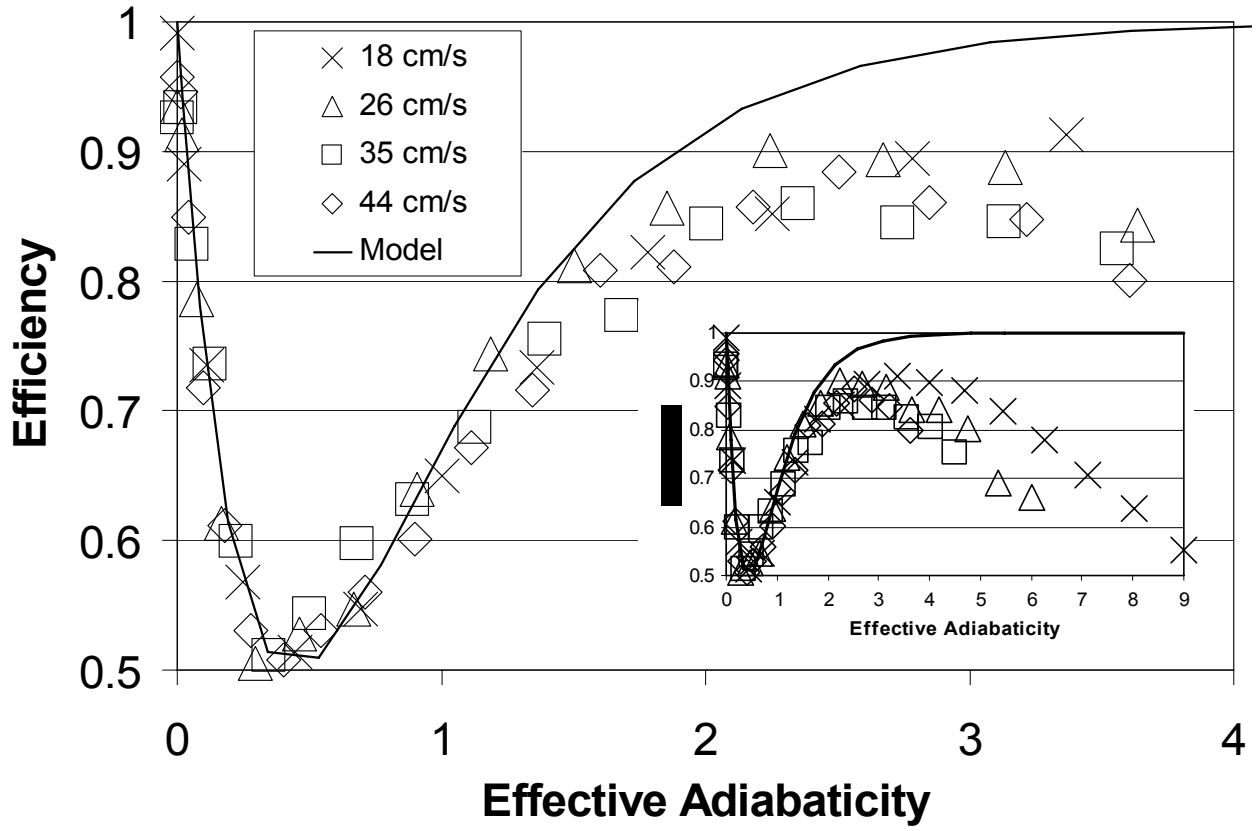

Figure 4.2. Experimental χ for different mean flow rates versus β'<4 and β'<9 (inset). The RF duty cycle was 93%. G_l was 0.25 G/cm and f_{AM} was 125 Hz. The data were corrected for T_1 relaxation in transit.

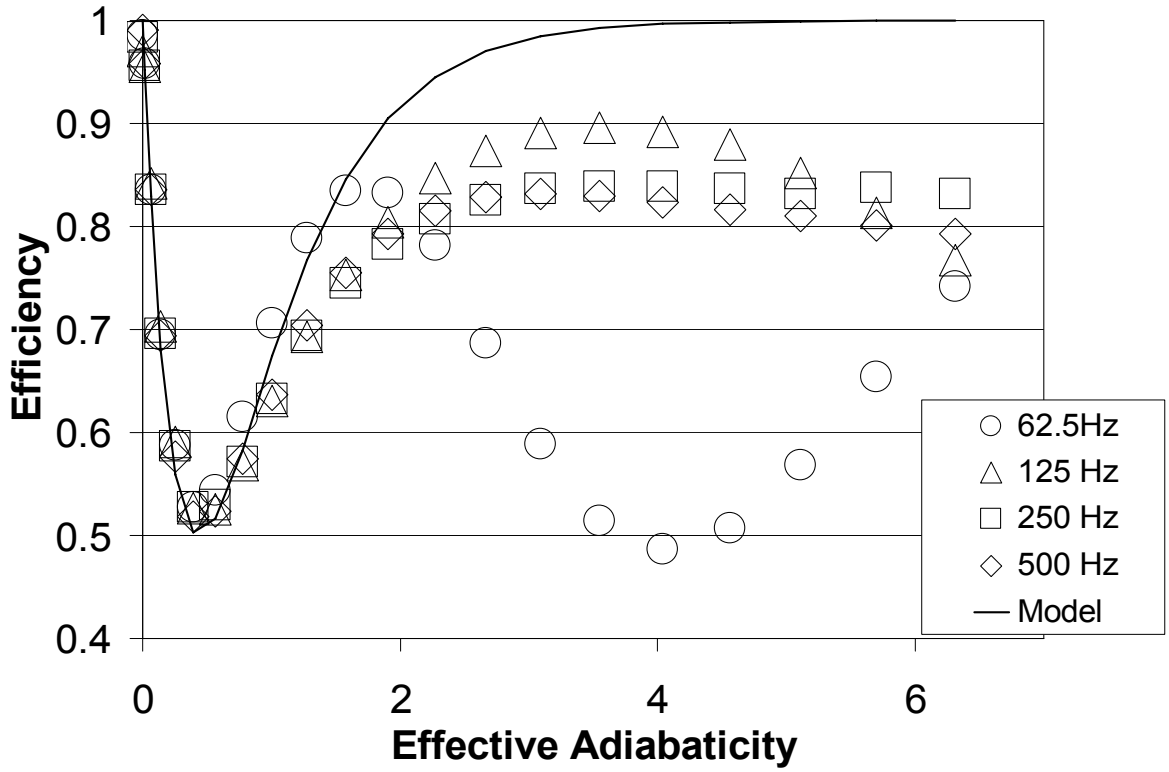

Figure 4.3. Experimental DAI efficiencies for different f_{AM} versus β'. χ was measured using flow with a mean velocity of 18 cm/s, G_l of 0.25 G/cm, and a 90% RF duty cycle. The data were corrected for T_1 relaxation in transit.

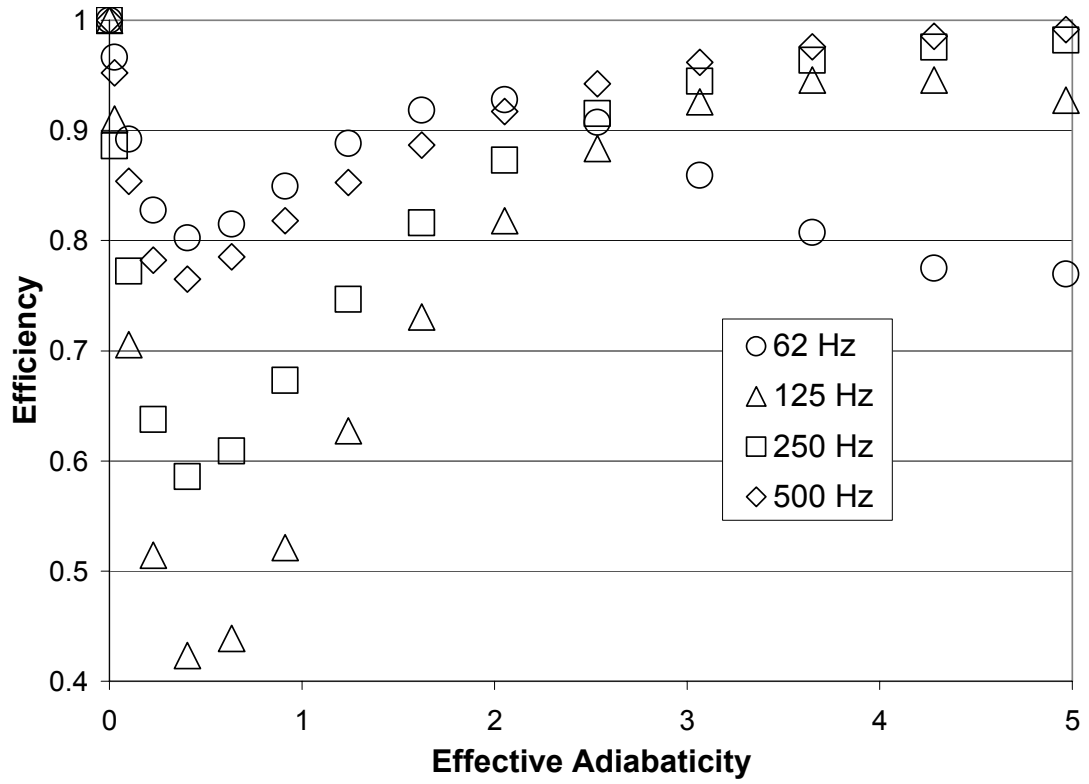

Figure 4.4. Simulated χ for four different f_{AM} versus β'. The efficiencies represent the mean from 7 component velocities for the laminar flow (<v> = 18 cm/s) used for the f_{AM} measurements (0.5<v> – 2<v> in increments of 0.25<v>) and include losses due to T_1 and T_2 relaxation during DAI. Gl was 0.25 G/cm.

Table 4.1. *In Vivo* Study Results

Experimental Parameter	**Mean**	**Stdev**	**Max**	**Min**
<v(t)> (cm/s)	19.85 +/- 0.67	4.98	28.90	10.36
B_1 at labeling plane (units of β_{1max})	0.72 +/- 0.02	0.08	0.88	0.54
β' SAI (SPDI)	1.31 +/- 0.09	0.49	2.85	0.63
β' SAI (ASD)	3.62 +/- 0.26	1.36	7.85	1.75
β' DAI (ASD)	1.82 +/- 0.13	0.68	3.95	0.88
$(SPDI/ASD)_{Gray\ Matter}$	1.16 +/- 0.05	0.28	1.81	0.78
$(SPDI/ASD)_{Model}$	1.13 +/- 0.02	0.09	1.31	1.00
Correlation Coefficient	0.974			

5.0 ADVANCED CASL MODEL IN PERFUSION

5.1 BACKGROUND OF CASL PERFUSION MODEL

Perfusion quantification using CASL requires a kinetic model to convert the CASL data to a perfusion map. Williams et al.[45], proposed a steady-state model based on Bloch equations in which macromolecules were saturated and there was no arrival delay between the end of labeling period and the image acquisition. However, Williams' model was applied to cerebral blood flow measurement in rats. The endogenous tracer arrival times are short (the mean value is 266 ms [108]) in rats. Arrival times in humans are approximately 1 s. T_1 relaxation of the labeled blood water occurs during the delay between the labeling blood at the labeling plane and its arrival at the vascular compartment. Zhang et al., [52] made an initial attempt to account for the arrival time effect by incorporating a T_1 relaxation attenuation factor into the inversion efficiency α. In principle, the arrival time for each voxel is needed to produce quantitative perfusion maps. However, perfusion SNR and time restrictions for the exam may make the acquisition and estimation of the arrival time impractical.

Alsop and Detre [54] proposed adding a transit delay between the end of labeling period and the image acquisition. The transit delay makes the perfusion maps insensitive to arrival times as long as the delay is greater than the arterial arrival times across the image. If the delay is greater than the arrival times, the flow model reduces to Williams' perfusion model while

taking into account the arrival time effect. However, both the Williams' and Alsop's kinetic models assume the duration of labeling to be infinitely long.

An alternative perfusion general kinetic model was proposed by Buxton et al. [74]. The proposed model is more general than previously used models but reproduces the earlier models under the appropriate assumptions: 1. the arrival of labeled blood at a particular voxel is via uniform plug flow; 2. the water exchange between tissue and blood is described by single-compartment kinetics; 3. the water is completely extracted from the vascular space. The labeling duration τ is taken into account. If the labeling duration is infinite, the perfusion model is reduced to Alsop's kinetic model.

Wang et al. [109] incorporated the labeling duration τ back into Alsop's perfusion model. The model is consistent with Buxton's model by replacing $T_{1t}^{'}$ by T_{1a} in the case of $w > \delta_a$, which is equivalent to assuming that the time to pass through the vasculature and into the tissue is long compared with T_1 and the labeling delay duration w, i.e., $m(t) = exp(-t/T_{1a})$ in Buxton's model. All above mentioned perfusion models are summarized in Table 5.1.

Table 5.1. the developments of rCBF quantification models. All equations are of the form $rCBF = \frac{\lambda Signal_{diff}}{Signal_{cont} 2\alpha} \frac{1}{C}$. α is added to account for inversion efficiency.

C in Perfusion Equation	Theory basis	reference
T_{1t}'	$\frac{dM_t}{dt} = \frac{M_t^0 - M_t}{T_1} + fM_a - \frac{f}{\lambda} M_t$	William 1992*
$\begin{cases} T_{1t}' \exp(-\delta_a / T_{1a}) & w < \delta_a \\ T_{1t}' \exp(-w / T_{1t}') \exp(-\delta_a (\frac{1}{T_{1a}} - \frac{1}{T_{1t}'})) & w > \delta_a \end{cases}$	$\frac{dM_t}{dt} = \frac{M_t^0 - M_t}{T_1} + fM_a - \frac{f}{\lambda} M_t$	Alsop 1996

$T_{1t}' \exp(-\delta_a / T_{1a})(1-\exp(-(\tau+w-\delta_a))) \quad w<\delta_a$ $T_{1t}' \exp(-w/T_{1t}') \exp(-\delta_a(\frac{1}{T_{1a}}-\frac{1}{T_{1t}'}))(1-\exp(-\tau/T_{1t}')) \quad w>\delta_a$	$M_t^0 - M_t = 2M_b^0 f\{c(t) \otimes [r(t)m(t)]\}$	Buxton 1998
$T_{1a}(\exp(-w/T_{1a}) - \exp(-(\tau+w)/T_{1a})) \quad w>\delta_a and\, \tau+w<\delta$	$\frac{dM_t}{dt} = \frac{M_t^0 - M_t}{T_1} + fM_a - \frac{f}{\lambda}M_t$	Wang 2002

5.2 BUXTON'S CASL KINETIC MODEL

The perfusion signal (S_f) is proportional to the cerebral perfusion rate (f) from the general kinetic model [74]:

$$S_f = f \cdot c \cdot k(t) \tag{5.1}$$

where $c = 2\alpha_{eff} M_a^0$ and $k(t) = a(t) \otimes [r(t) \bullet m(t)]$ (5.2)

In the above equations, M_a^0 is the equilibrium arterial blood magnetization, α_{eff} is the effective inversion efficiency, f is the perfusion rate, $a(t)$ is the delivery function, i.e., the normalized arterial concentration of magnetization arriving at the voxel at time t. $r(t)$ is the residue function, i.e., the fraction of labeled water molecules that remains in the voxel after t time unit from the arrival time, $m(t)$ is the magnetization relaxation function based on the T_1 relaxation times, i.e., the fraction of longitudinal magnetization of labeled water that remains in the voxel after t time unit from the arrival time. With the following assumptions, the factors of $k(t)$ of the general kinetic model are simplified to previous standard models.

Uniform plug flow assumption: The arrival of labeled blood at a particular voxel is assumed to occur via uniform plug flow. After the blood is labeled, it has to experience a time

delay t_z to arrive at the voxel in the image plane from the labeling plane. Therefore, no labeled blood arrives before the delay t_z. During the time $t_z < t < t_z + \tau$ (where τ is the labeling duration), the arriving blood is labeled uniformly; and after time $t_z + \tau$, the arriving blood is again unlabeled. The arterial function *a(t)* is written as:

$$a(t) = \begin{cases} 0 & 0 < t < t_z \\ \exp(-t / T_{1a}) & t_z < t < t_z + \tau \\ 0 & t_z + \tau < t \end{cases} \tag{5.3}$$

where T_{1a} is the blood longitudinal relaxation time.

Single-compartment kinetics assumption: Water exchange between tissue and blood are assumed to be so rapid that their concentration ratios remain constant. In particular, the ratio of total tissue concentration to the venous concentration is a constant equal to the equilibrium tissue/blood partition coefficient of water λ. With this assumption, the residue function is:

$$r(t) = \exp(-ft / \lambda) \tag{5.4}$$

Immediate and complete extraction from the vascular space assumption: The water is completely extracted from the vascular space immediately after arrival in the voxel. With this assumption, the relaxation function is:

$$m(t) = \exp(-t / T_{1t}) \tag{5.5}$$

5.3 OUR CASL KINETIC MODEL

No-exchange assumption: There has been evidence that spin labeled water substantially relaxes prior to exchange with tissue water in humans at 1.5 T [95, 110-112]. The inverted protons relax via T_1 before they leave the intravascular space, especially for white matter where the arrival times are

longer than gray matter. The no-exchange hypothesis may not hold in animals models where the blood flows are typically higher and arrival times are typically lower than humans.

Under the assumption of no-exchange, the residue function can be modeled as:

$$r_{no\_ex}(t) = 1 \tag{5.6}$$

since the labeled blood relaxes before exchanging with the tissue. The labeled water protons are still in the vasculature when the protons relax, and so the assumption for immediate and complete extraction from the vascular space is invalid. Therefore, the relaxation function *m(t)* needs to be modified to:

$$m_{no\_ex}(t) = \exp(-(t + t_z)/T_{1b}) \cdot u(t) \tag{5.7}$$

where *u(t)* is the unit step function. T_{1t} is replaced by T_{1b} in the Equation (5.5) since the magnetization still decays with the relaxation time of blood after an initial arrival time t_z. The arrival time t_z is added to address the magnetization attenuation that occurs between labeling and the arrival time. The arterial function *a(t)* must be similarly adjusted to include a nonzero arrival time t_z. *a(t)* can be modified accordingly.

$$a(t) = u(t - t_z) - u(t - \tau - t_z) \tag{5.8}$$

Hence, the definition of *m(t)* is the normalized magnetization after time *t* unit from the arrival time t_z, and *a(t)* represents whether the label blood arrives at the voxel at time t or not. The definitions of *m(t)* and *a(t)* are more logical and hemodynamically sound.

E**xchange assumption:** There is also evidence that the labeled blood water exchanges with tissue water before it relaxes at fields greater than 1.5 T [113]**.** The water exchange between tissue and blood can be described by an equilibrium tissue/blood partition coefficient of water, λ. With this assumption, the residue function can be modeled as:

$$r_{ex}(t) = \exp(-ft/\lambda) \tag{5.9}$$

The magnetization decays with the relaxation time of tissue after an initial arrival time t_z if we assume that blood water exchanges with the tissue water immediately after its arrival. In this case, the relaxation function can be modeled as:

$$m_{ex}(t) = \exp(-t/T_{1t} - t_z/T_{1b}) \cdot u(t) \tag{5.10}$$

The theoretical curves of the arterial functions, the relaxation functions, and the residue functions for no-exchange model vs. exchange model are shown in Figure 5.1.

Off-resonance saturation effects: In the above models, we have ignored the effects of off-resonance saturation on image intensity. The off-resonance RF saturation at the imaging slices is minimal for a separate labeling RF coil [59]. For single-coil CASL, the RF saturation may be significant. The application of off-resonance RF causes a decreased signal at the image slices even in the absence of perfusion. The signal attenuation may not match perfectly between the control and labeling RF irradiation.

The signal attenuation difference between the control and label images is referred to as residual MT ($S_{\Delta MT}$) herein. For a single-coil CASL, the difference signal (ΔM) between control and label images is composed of the perfusion (S_f) and residual magnetization transfer ($S_{\Delta MT}$) signals.

$$\Delta M(t) = S_f + S_{\Delta MT} \tag{5.11}$$

By combining Equation (5.1), (5.2) and (5.11), the perfusion rate f can be calculated as:

$$f = \frac{\frac{\Delta M(t) - S_{\Delta MT}}{M_C}\frac{M_C}{M_a^0}}{2\alpha_{eff}k(t)} \tag{5.12}$$

5.4 ESTIMATION OF PARAMETERS IN OUR CASL PERFUSION MODEL

Estimation of M_a^0: For absolute quantification, the difference signal should be normalized to the blood magnetization and not the steady-state tissue signal. However, M_a^0 cannot be measured easily and directly. Traditionally, the relationship between M_a^0 and tissue magnetization M_t^0 was based on the partition coefficient λ [47, 54, 114]:

$$M_a^0 = \frac{M_t^0}{\lambda} e^{(\frac{1}{T_{2t}^*} - \frac{1}{T_{2a}^*})TE} \tag{5.13}$$

where the exponent corrects for imaging sequence effects (assumes a gradient-echo pulse sequence), λ_{brain}, λ_{GM} and λ_{WM} having values of 0.90, 0.98 and 0.82 ml/g, respectively [115]. The T_2 relaxation times (including B_0 inhomogeneities) for tissue (T_{2t}^*) and blood (T_{2a}^*) are 55 ms and 100 ms [116] respectively at 1.5 T. T_2* depends on the actual magnet homogeneity and voxel size and may vary between systems. However, Buxton [74] argues that the use of partition coefficient is not accurate. The current standard is to calculate the blood magnetization (M_a^0) from white matter magnetization (M_t^0) [116]:

$$M_a^0 = M_t^0 \frac{\rho_a}{\rho_t} e^{(\frac{1}{T_{2t}^*} - \frac{1}{T_{2a}^*})TE} \tag{5.14}$$

where density of arterial blood (ρ_a) is 1.06 g/ml; density of tissue (ρ_t) is 1.05 g/ml for both gray and white matter. With these values and a TE of 21 ms for ramp-sampled EPI in our CASL experiments:

$$M_a^0 \approx \Lambda M_t^0 \quad \text{with } \Lambda = 1.2 \tag{5.15}$$

Tissue magnetization (M_t^0): We normalize the difference signal (M_C-M_L) to the control image to correct for the RF inhomogeneity and system instability and save acquisition time by avoiding the separate acquisition of tissue magnetization. The control image includes signal

losses from off-resonance RF saturation. We can calculate the tissue magnetization M_t^0 based on the control magnetization and our RF saturation model:

$$M_t^0 = \frac{M_c}{1-(1-MT)e^{\frac{-(w+\Delta t_{acq})}{T_{1t}}}} \tag{5.16}$$

where w is the postlabeling delay, Δt_{acq} is the acquisition time measured from the start of the multi-slice acquisition in s. T_{1t} is the longitudinal relaxation time of the tissue. Based on our 1.5 T brain studies, mean gray and white T_1 values of 1.065 and 0.800 s, respectively, were used for the T_1 relaxation correction. MT is the signal loss $M_{z,norm}(\Delta)$, which can be calculated by Equation (3.4).

By simple arithmetic from Equation (5.15) and (5.16), we have

$$\frac{M_c}{M_a^0} = [1-(1-MT)e^{\frac{-(w+\Delta t_{acq})}{T_{1t}}}]/\Lambda \tag{5.17}$$

Arrival time & convolution model: The arrival time (t_z) of the labeled blood at the imaging plane from the labeling plane should be measured directly, by varying the transit delay. This time should not include the time for the tracer to exit the intravascular space and enter the extravascular space. The arrival time varies for different individuals. In the normal human brains, t_z values typically range from 0.7 to 1.5s in gray matter and higher in white matter[54, 95]. We only calculate the gray matter perfusion map due to the long tracer arrival time and poor SNR in white matter.

The convolution *k(t)* is directly related to the arrival time t_z. Let us take a look at the convolution *k(t)* more carefully to see the relation. From Equation (5.2) and the definition of convolution, we have:

$$k(t) = \int_{-\infty}^{\infty} a(t-t')[m(t')r(t')]dt' \tag{5.18}$$

The convolution *k(t)* for the no-exchange model and exchange model can be written in an analytical format as Equation (5.19) and (5.20):

$$k_{no\_ex}(t) = \begin{cases} 0 & t < t_z \\ T_{1b}(e^{-t_z/T_{1b}} - e^{-t/T_{1b}}) & t_z < t < t_z + \tau \\ T_{1b}(e^{-(t-\tau)/T_{1b}} - e^{-t/T_{1b}}) & t > t_z + \tau \end{cases} \tag{5.19}$$

$$k_{ex}(t) = \begin{cases} 0 & t < t_z \\ T'_{1t} e^{-t_z/T_{1b}}(1 - e^{-(t-t_z)/T'_{1t}}) & t_z < t < t_z + \tau \\ T'_{1t} e^{-t_z/T_{1b}} e^{-(t-t_z-\tau)/T'_{1t}}(1 - e^{-(t-\tau)/T'_{1t}}) & t > t_z + \tau \end{cases} \tag{5.20}$$

where T'_{1t} is the effective tissue relaxation time, by incorporating the effect of flow in T_1 shortening:

$$\frac{1}{T'_{1t}} = \frac{1}{T_{1t}} + \frac{f}{\lambda} \tag{5.21}$$

t represents the slice acquisition time, measured from the beginning of the sequence:

$$t = \tau + w + \Delta t_{acq} \tag{5.22}$$

w is the postlabeling delay (typically 0.7 s for our experiments), Δt_{acq} is the acquisition time (measured from the start of the multi-slice acquisition in s):

$$\Delta t_{acq} = TE + (n-1) \cdot TR_{slice} \tag{5.23}$$

where *TE* is the echo time (0.021s in our rampsampled EPI, 0.028 s in our regular EPI, 0.008 ms for our single-shot spiral), *n* is the slice index (1 to 19 for rampsampled EPI, 1 to 15 for regular EPI), and TR_{slice} is the acquisition time per slice (1/19 s (second) for rampsampled EPI, 1/15 s for regular EPI).

The graphs of $k_{no\_ex}(t)$ and $k_{ex}(t)$ with the effects of varying t_z are shown in Figure 5.2. The maximum point of the convolution for both $k_{no\_ex}(t)$ and $k_{ex}(t)$ is reached at time $t_z + \tau$ (arrival time plus pulse labeling duration). All the curves of $k_{no\_ex}(t)$ with varying t_z merge together if the acquisition time is larger than the pulse duration time plus the longest arrival time. If we acquire the image slices after all the labeled blood tracers arrives ($t > t_z + \tau$), $k_{no\_ex}(t)$ for all the image voxels will be described by a mathematical formula without dependency on the arrival time variable t_z (see $t > t_z + \tau$ part of Equation 5.17). As previously reported by Alsop and Detre [54], acquiring the slices after $t_z + \tau$ will make the perfusion maps completely insensitive to arrival times. We can estimate the value of $k_{no\_ex}(t)$ at any acquisition time $t > t_z + \tau$. However, the value of k_{no_ex}(t) depends on the arrival times of the image slices if $t_z < t < t_z + \tau$. (see $t_z < t < t_z + \tau$ part of Equation 5.17).

The convolution k_{ex}(t) is not completely insensitive to the arrival time after $t_z + \tau$. The convolution depends on the difference in the blood relaxation time T_{1b} and the tissue relaxation time T_{1t}.

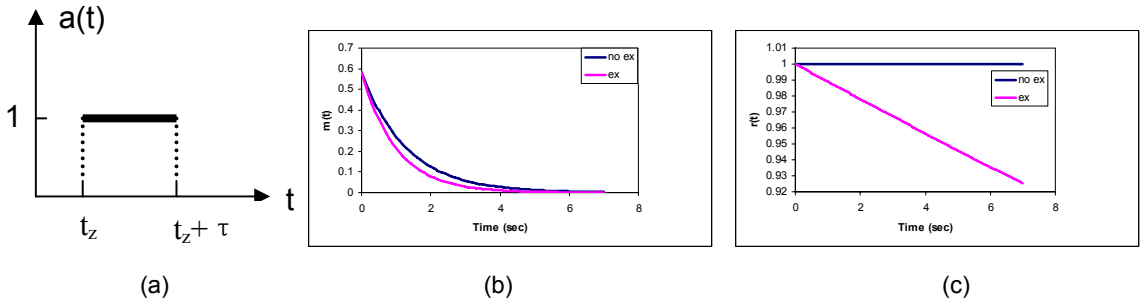

Figure 5.1. Depictions of (a) idealized artery delivery function a(t), (b) magnetization relaxation function m(t), and (c) residue function from no-exchange model vs. exchange model. Parameters for the curves are T1b = 1.3 s, tz = 0.7 s, f = 60 ml/100g/min corresponding to f = 0.01 s-1, and λ = 0.9.

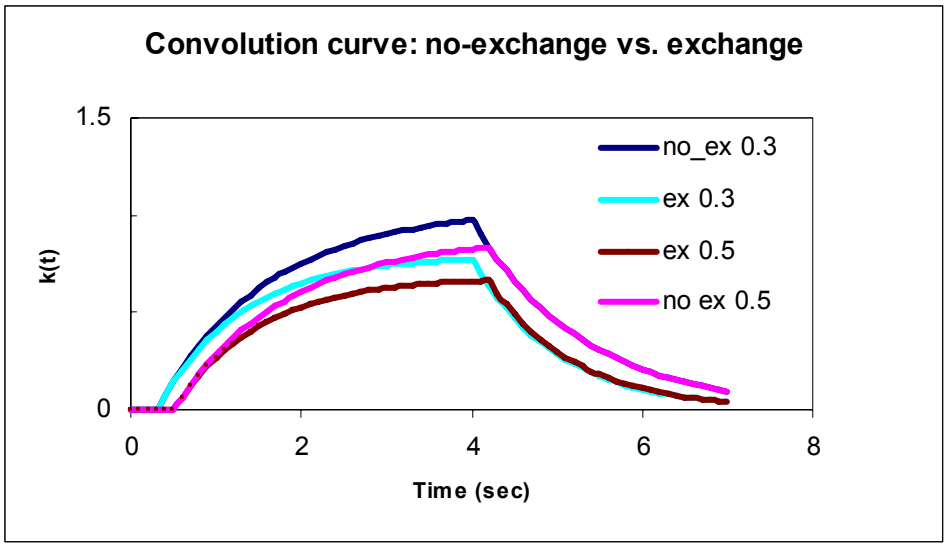

Figure 5.2. Theoretical curves of the convolution k(t) of CASL versus time with varying arrival time for no-exchange model vs. exchange model. Parameters for the three curves are T_{1b} = 1.3 s, T_{1t} = 1.0 s, τ = 3.7 s.

5.5 THE ISSUE OF PREVIOUS CASL PERFUSION & OUR SOLUTION

There are several issues in the quantification of CASL MRI perfusion bring concerns to us beside those described in Chapter 3 and 4. First, the introduction of a long transit delay greatly decreases the sensitivity of the perfusion technique to the arrival time. However, the insensitivity comes at the expense of decreased SNR and increased exam time. Moreover, the transit delay is limited by the T_1 relaxation time and may not be adequate for subjects with cerebrovascular disease.

Second, an assessment of cerebral perfusion between normal controls and AD subjects was performed by assuming that the blood tracer fully relaxes before it exchanges with the tissue water [26]. However, it is important to investigate whether the blood tracer exchange occurs and determine whether the no-exchange model or exchange model fits for the perfusion

quantification. Third, the residual off-resonance saturation effects were previously assumed to be negligible [26]. Fourth, the inferior-to-superior acquisition was adopted in previous perfusion experiments. The acquisition direction is same as the blood tracer flow orientation. Hence, imaging may perturb the blood tracer and the difference signals. Fifth, the multislice CASL difference signals contain information on the blood arrival time for each slice.

5.5.1 The issue of acquisition direction

An inferior-to-superior acquisition was used (shown in Figure 5.3(a)) in earlier perfusion experiments [26]. However, the acquisition order can perturb the blood tracer and exacerbate off-resonance saturation effects. A simulation was carried out to compare the off-resonance saturation effects between inferior-to-superior and superior-to-inferior acquisition order. A 100 ms delay was placed between the off-resonance saturation (for SAI) and image acquisition (with different acquisition order). Images were also acquired without off-resonance saturation for normalization of the RF saturation data. The RF saturation curves were corrected for signal increases caused by T_1 relaxation that occurred during the delay between off-resonance saturation and image slice acquisition using Equation (3.17). The simulation comparison of RF saturation effects between the two different acquisition orders is shown in Figure 5.3(b). The 1.5 s postlabeling delay reduces the degree of the RF saturation effects, but the saturation effects still vary ten percent (which can be calculated from the values in Figure 5.3(b).

The RF saturation effects caused by the inferior-to-superior acquisition order are severe and vary from slice to slice. The varying RF saturation effects from slice to slice affect the accuracy of three-dimensional motion correction. The motion correction algorithm may fail because the algorithm may have difficulty in finding matching voxels due to large variance of

adjacent slices. Even if the algorithm can proceed, the varying RF saturation effects from adjacent slices will contaminate the signals of the motion-affected voxels, and thus perfusion signals.

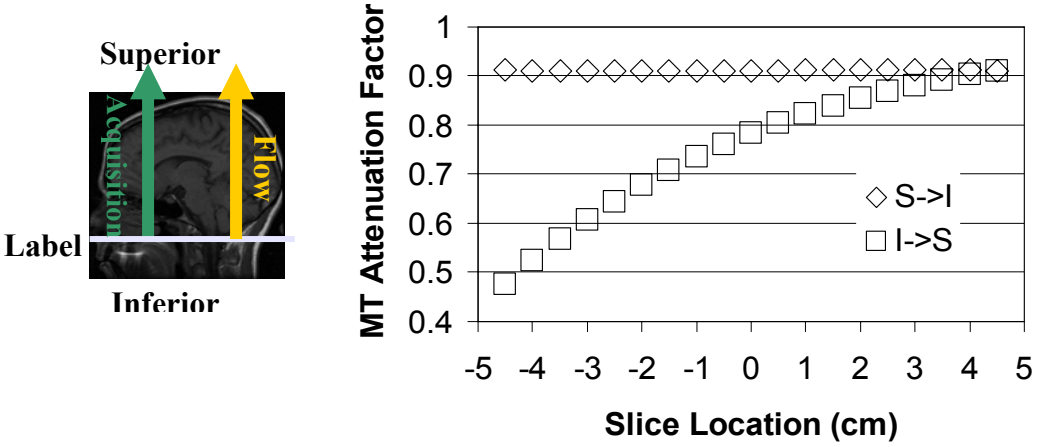

Figure 5.3. (a) Representation of blood flow and acquisition directions. (b) The comparison of RF saturation effects measured in agar phantom between inferior-to-superior and superior-to-inferior acquisition direction.

5.5.2 The issues of long delay & our solution

A long postlabeling delay (1.5 s) was adopted by Alsop et al. after the labeling period to reduce the arrival time sensitivity [26, 54]. The choice of postlabeling delay 1.5 s may not be long enough for some diseased subjects or white matter. The arrival time can vary from 0.9363 to 1.6063 with mean 1.1566 and standard deviation 0.1385 according to our CASL perfusion measurements in elderly subjects. In order to get the perfusion maps of all subjects quantified accurately, the postlabeling delay needs to be longer than the longest arrival time in the population of the subjects, which is not known without direct measurements. A longer postlabeling delay leaves less time for the brain image acquisition. In principle, two or more separate acquisitions are required to provide the complete coverage of the brain since the

endogeneous tracer is relaxing. The length of the postlabeling delay, and thus the tolerance of long arrival time are limited by T_1 relaxation and SNR. The theoretical value of *k(t)* (which is proportional to the CASL signal) is decreased to 0.3862 at the time t = 1.5 + 3.7 s from Equation (5.19). In summary, one must trade-off the insensitivity of the arrival time with perfusion SNR and brain coverage.

A recent rat study [117] determined the arrival times as part of CASL measurements to choose the delay more efficiently for each subject. This method helps to determine the delay but doubles the time cost of CASL measurements. Large bipolar gradients were used to destroy signal from moving arterial water spins [53] instead of having postlabeling delay. However, the inclusion of a bipolar gradients in the imaging sequence has been shown to reduce the perfusion signal and cause a lengthening of the measured arrival time [46].

We acquire the image volume earlier by inserting a short postlabeling delay (700 ms) between labeling and imaging to gain more SNR for image slices. The whole brain volume can be covered in one acquisition. The total time for acquiring CASL perfusion images is less than 10 minutes for 50 pairs of control and label images, which is half of the acquisition time used previously [61]. However, our approach will be sensitive to the arrival time, so the kinetic model related to arrival time needs to be considered.

In our approach, we used a superior-to-inferior acquisition order. Figure 5.4 illustrates the convolution curves with different arrival times, and the derived curve of convolution signal changes from superior to inferior slices. At 700 ms postlabeling delay, the superior slice (assuming that the arrival time of the slice is 1.5 s for the illustration purpose) was sampled first, the average convolution signal intensity for the slice corresponds to a dot of the convolution curve with arrival time = 1.5 s at the time t = 3.7 + 0.7 s (the first yellow dot in Figure 5.4). The

convolution signal intensities for the later slices correspond to the dots from other convolution signal curves with shorter arrival time (compared to the arrival time of the first superior slice). We obtained the theoretical curve of interslice convolution signal changes by connecting the convolution signals from all slices in the superior-to-inferior acquisition order (the pink line in Figure 5.4). We assumed that the superior slices have longer tracer arrival times.

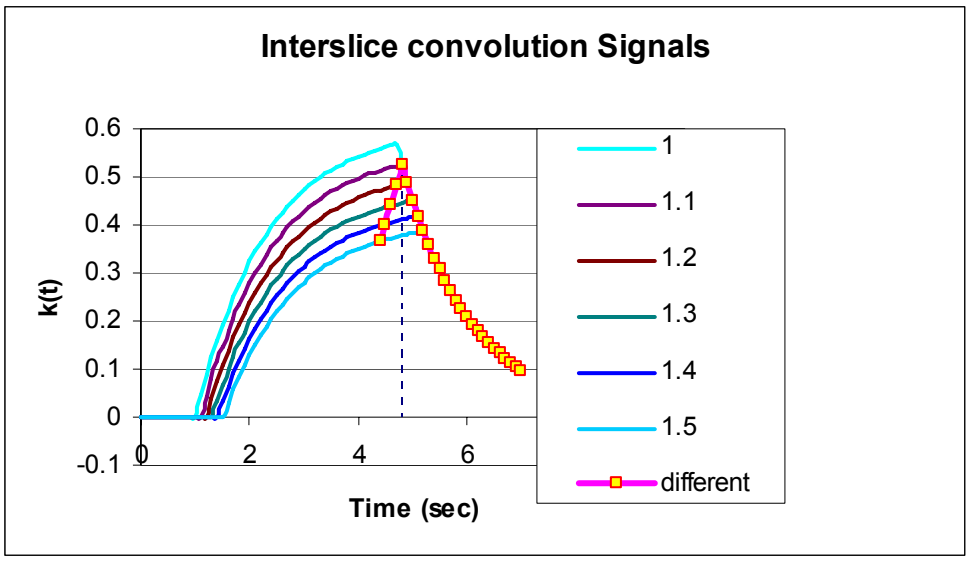

Figure 5.4. The curve of interslice convolution signal with varying acquisition time. The pink line stands for interslice signal changes from the superior-to-inferior acquisition order.

For the maximum point of the interslice convolution curve, the slice acquisition time coincides with the tracer arriving at the slice ($\tau + t_z$).

Our perfusion measurement is based on two key observations of the interslice convolution curve $k_{IS}(t)$: (I) When the slice acquisition time coincides with the arrival time ($\tau + t_z$), the maximum point of the interslice convolution curve is achieved; and (II) At the slice with coincident arrival time and acquisition time, the achieved maxima is same as the maxima of the convolution curve of the slice itself.

The normalized interslice CASL difference signals have the same curve shape (only a constant factor $2\alpha_{eff}$ difference) as the interslice convolution curve, assuming the gray matter CBF is a global constant for each subject (i.e., in the absence of significant cerebrovascular disease) [46, 110, 116]. Therefore, CASL interslice signals reach the maxima at the same time as the interslice convolution signals.

We can search for the time that the CASL interslice signals reach the maxima. According to the observation (I) of the interslice convolution curve, the calculated time is the summation of postlabeling delay and the tracer arrival time. Thus, the tracer arrival time can be obtained by subtracting the postlabeling delay time from the calculated time t_z^0.

According to the observation (II) of the interslice convolution curve, the maxima of the interslice convolution curve can be obtained by calculating the maxima of the convolution curve for the slice acquired at the above calculated tracer arrival time t_z^0. The convolution curve is described by Equation (5.19) or (5.20) (please refer section 5.5.3 to choose which Equation). The maxima of the convolution equation for the slice is obtained at the time $t = t_z^0 + \tau$. The blood relaxation time T_{1b} and $T_{1t}^{'}$ are needed to measure the maxima of the convolution equation. T_{1b} can be calculated based on individual hemotocrit. $T_{1t}^{'}$ can be calculated based on the average value of the gray matter T_1 map.

The maxima of the interslice convolution curve can be obtained from the above calculation; the shape of the interslice convolution curve is same as the CASL interslice signal curve by assuming gray matter perfusion as a global constant. Therefore, the practical interslice convolution curve can be obtained by shifting the CASL interslice signal curve by a factor so that the maxima matches with the above calculated theoretical value.

A couple of issues are related to the perfusion quantification. The model assumes that gray matter perfusion is a global constant for each subject. This is not likely to be true if the subject has significant cerebrovascular disease. However, cerebovascular disease is one of the exclusion criteria for the perfusion study.

A potential inaccuracy can arise from the quantification of the interslice convolution curve. The convolution curve is based on the average gray matter signals from the left/right half axial slices. We used average arrival time for the left/right side of each axial slice. However, the blood arrival times may have large variance, which will, in turn, lead to inaccuracies in perfusion measurements.

5.5.3 Which model: exchange model versus no-exchange model?

The crucial task to figure out is whether the blood tracer exchanges with the gray matter tissue in elderly brains. This is equivalent to asking whether the no-exchange model or exchange model (Equation (5.19) or (5.20)) needs to be adopted for the perfusion model.

CASL interslice data were analyzed to determine if tracer exchange occurs in gray matter in elderly brains. CASL difference signal for each single slice was calculated based on an average difference signal for the whole gray matter volume. From Equation (5.12) and (5.19), the CASL difference signal without exchange depends on the blood relaxation time T_{1b}, acquisition time t and perfusion rate f. From Equation (5.12) and (5.20), the CASL difference signal incorporates tissue relaxation time T_{1t} besides the above mentioned three variables in the exchange model.

Based on the published values and our DSC data (averaged over the whole gray matter volume), the blood arrival time can be modeled as the power function of the distance from the labeling plane:

$$t_z(z) = a(z - z_0)^b \qquad (5.24)$$

where z_0 is the location of the labeling plane, z is the slice location, and a and b are fitting parameters. In a 2D CASL acquisition, each image plane contains both spatial and temporal information since each slice is acquired at a different time with respect to the beginning of the label generation. The acquisition time t is linearly dependent on the slice location z by recalling the Eq. (5.22) and (5.23).

The CASL difference signal is a function of blood relaxation time (T_{1b}) (and tissue relaxation time T_{1t} in the exchange case), the slice location (z, from the t_z and acquisition time t), parameters of the power function (a and b) and perfusion f. The left and right hemisphere perfusion were calculated separately by fitting the CASL signals with respect to the slice location to a spatio-temporal model based on the convolution tracer model, the signal acquisition timing, and the assumption that gray matter perfusion is a global constant [74]. Fitting was performed using the Levenburg-Marquardt method of least square. Three fits were performed: 3-parameter fits (a, b, and f) with no tracer exchange, 4-parameter fits with (including T_{1t}) and without exchange (including T_{1b} as a variable). T_{1b} was calculated based on individual hemotocrit [118] when not fitted as a variable ($\langle T_{1b} \rangle$ = 1.41 ± 0.2 s). Fifteen normal subjects (age 82 ± 3) were selected to study the tracer model.

The representative fits of interslice CASL difference signals in gray matter with exchange (4-parameter) and without tracer exchange (3 parameters) are shown in Figure 5.5. The 4-parameter model with tracer exchange provides the best fit. Summary of findings for 15 subjects

from the three models are shown (Table 5.3). Average gray matter perfusion of 15 subjects were 53 ± 13 ml/100g/min and 51 ± 14 ml/100g/min for left and right hemisphere, respectively. These values are slightly lower than the published PET perfusion of 67 ± 13 ml/100g/min for gray matter of young brain [119]. However, perfusion was shown to decrease with age [120]. The average fitted T_{1t} was 1.06 ± 0.19 s. The 4-parameter fit (no-exchange) overestimated the gray matter perfusion by 45% compared to PET while the fitted $<T_{1b}>$ of 0.93 ± 0.16 s was lower than the literature. The results indicate that the tracer exchanges with the tissue water, before it decays, for the elderly brain gray matter at 1.5 T.

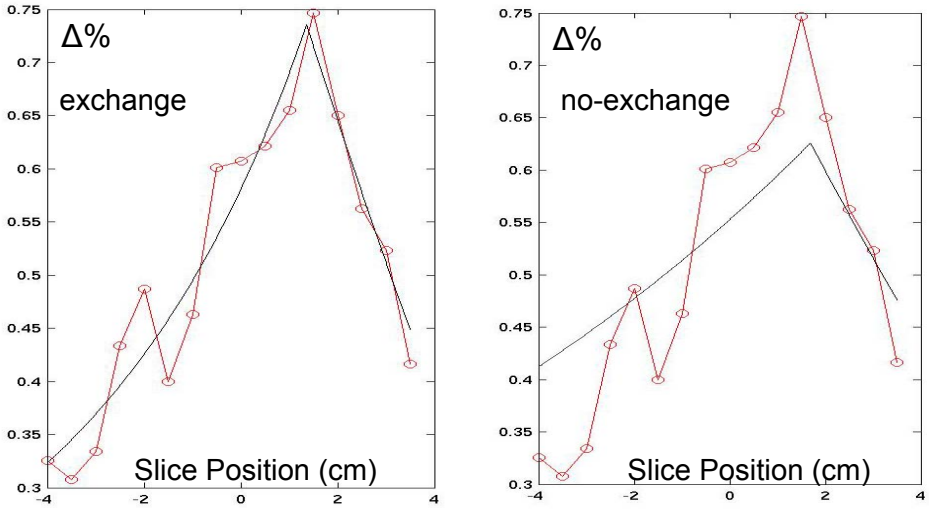

Figure 5.5. Illustrative fits of interslice CASL difference [(control-label)/control] signals in gray matter with exchange and without tracer exchange. T1b was calculated based on the subject's hematocrit. The exchange model provides a superior fit, indicating that the blood water is exchanging with the tissue water.

Table 5.2. Summary of Findings for 15 subjects.

Model	Gray matter perfusion (ml/100g/min)	Mean R^2	T_{1b} (s)
4-parameter (no-exchange)	92 ± 40 (L) 89 ± 39 (R)	0.68 ± 0.15 0.63 ± 0.17	0.93 ± 0.16 (Fitted)
3-parameter (no-exchange)	34 ± 6 (L) 33 ± 7 (R)	0.55 ± 0.18 0.54 ± 0.13	1.41 ± 0.02
4-parameter	53 ±13(L)	0.72 ± 0.17	1.41 ± 0.02

(exchange)	50 ±14(R)	0.65 ± 0.19	

5.5.4 Inference of blood arrival time

From section 5.5.3, the CASL difference signals should be fitted with respect to the slice location by the exchange model. The fitted parameters (*a* and *b*) can be used to calculate the blood left and right arrival times of each slice separately by Equation (5.24). The blood left and right arrival times of each slice can be inferred in the process of perfusion calculation with no extra time cost. Furthermore, the method can be extended to infer the arrival times for smaller clusters if the SNR of images is large enough.

One perfusion study was selected to investigate the differences of arrival times for each slice and its potential error in the perfusion calculation. Four regions (upper left (ul), upper right (ur), lower left (ll), lower right (lr)) were divided for each axial slice. The blood relaxation time of 1.4328 s is based on the hematocrit [118]. The fitted gray matter tissue relaxation time was 1.0041 s in the original perfusion calculation (The gray matter T_1 was 1.1260 s when calculated separately from the non-saturated T_1 map). The gray matter tissue relaxation time was fixed for the arrival time calculation of each region.

The arrival time for each of four regions is listed on Table 5.3. The arrival times heavily depend on the regions: the upper left and lower left sides only change 1.6%, but the upper right and lower right sides change 6.0%. The global perfusions for the upper left and the lower left are 58.7102 ml/100g·min and 57.3034 ml/100g·min, which is a 2.03% and 0.42% change from the global perfusion (57.5426 ml/100g·min) for the left side. The global perfusions for the upper right and the lower right are 53.6945 ml/100g·min and 56.7990 ml/100g·min, which is a 2.66% and 2.96% change from the global perfusion (55.1641 ml/100g·min) for the right side. The

perfusion changes due to the arrival time difference were calculated from Equation (5.12) and (5.20) (Table 5.4). The differences of arrival times caused larger changes in perfusion for the superior slices. The perfusion of the upper right region on slice 3 changes 7.5% from the original right side perfusion.

The blood arrival times of four clusters (upper left, upper right, lower left, lower right) for each axial slice were calculated in this case. The arrival times of clusters have large variance even within the slice. We need to take the arrival time differences into account to improve the perfusion quantification. The improved perfusion quantification can be achieved by dividing each axial slice into several small clusters in the same manner and calculating the perfusion map for each cluster by taking advantage of the interslice signals as mentioned in section 5.5.2. Moreover, the arrival time for each small cluster can be calculated the same as the arrival time of the four clusters in this section. Therefore, the cluster-wise arrival time map can be generated.

Table 5.3. The difference of arrival times of four regions. Δ stands for the relative changes of the arrival times (e.g. $\Delta t_z\_ul = (t_z\_ul - t_z\_l)/t_z\_l$. *ul* stands for upper left, *ur* for upper right, *ll* for lower left, *lr* for lower right)

Slice	t_z_l	Δt_z_ul (%)	Δt_z_ll (%)	t_z_r	Δt_z_ur (%)	Δt_z_lr (%)
3	1.7903	-1.62	1.62	1.7073	-6.02	5.09
4	1.5986	-1.62	1.62	1.536	-6.02	5.09
5	1.4212	-1.63	1.62	1.3762	-6.02	5.09
6	1.2574	-1.62	1.61	1.2275	-6.01	5.09
7	1.1067	-1.63	1.62	1.0896	-6.02	5.08
8	0.9685	-1.62	1.62	0.962	-6.02	5.09
9	0.8423	-1.61	1.63	0.8445	-6.02	5.09
10	0.7276	-1.61	1.62	0.7366	-6.01	5.09
11	0.6239	-1.62	1.62	0.6381	-6.02	5.08
12	0.5305	-1.62	1.6	0.5484	-6.02	5.09
13	0.4469	-1.63	1.61	0.4673	-6.03	5.07
14	0.3726	-1.64	1.61	0.3943	-6.01	5.1
15	0.307	-1.63	1.6	0.3291	-6.02	5.07
16	0.2496	-1.64	1.6	0.2713	-6.04	5.09
17	0.1998	-1.6	1.65	0.2204	-5.99	5.08
18	0.1572	-1.65	1.59	0.1761	-6.02	5.11

Table 5.4. The change of perfusion due to the change of arrival times.

N	Δf_ul(%)	Δf_ll(%)	Δf_ur(%)	Δf_lr(%)
3	2.2	-2.25	-7.5	6.87
4	1.93	-1.97	-6.66	6.05
5	1.69	-1.72	-5.92	5.32
6	1.48	-1.5	-5.24	4.68
7	1.3	-1.31	-4.64	4.1
8	1.12	-1.14	-4.08	3.6
9	0.97	-0.99	-3.57	3.13
10	0.83	-0.85	-3.11	2.71
11	0.72	-0.72	-2.7	2.33
12	0.61	-0.61	-2.31	2
13	0.52	-0.51	-1.98	1.69
14	0.43	-0.43	-1.66	1.43
15	0.35	-0.35	-1.39	1.19
16	0.29	-0.28	-1.15	0.98
17	0.23	-0.23	-0.93	0.79
18	0.18	-0.18	-0.74	0.64

5.5.5 The issue of residual off-resonance saturation effects

The residual off-resonance saturation effects are typically assumed to be negligible [26, 61] in CASL experiments. However, our residual off-resonance saturation measurements (including non-adiabatic effects) demonstrate that it can vary from 0.0501% to 0.2821% with mean 0.1596% and standard deviation 0.0781%, which is around 15% of the signal with an insertion of 700 ms postlabeling delay (Figure 5.6). The residual off-resonance saturation effects will decay to several percents for the 1.5 s postlabeling delay used by other investigators, but it will vary with different frequency offsets. Therefore, the residual effects need to be characterized and corrected, or it will introduce error in the CBF quantification.

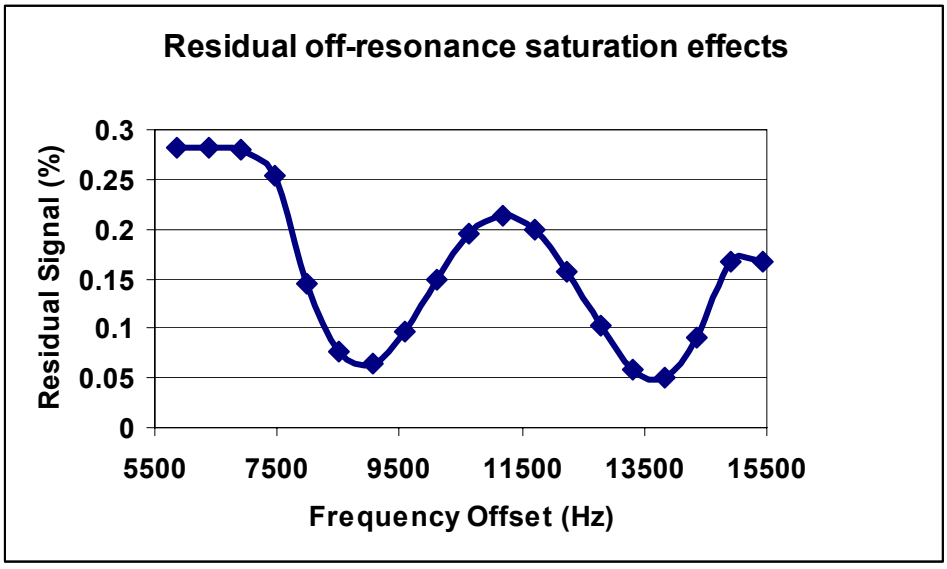

Figure 5.6. The effects of residue off-resonance saturation with different frequency offsets and 700 ms postlabeling delay from human data.

5.6 ENHANCEMENTS TO CASL PERFUSION MODEL

5.6.1 Materials and Methods

All data were acquired using a 1.5T GE Signa system (Milwaukee, WI, LX). The standard GE quadrature head coil was used for labeling as well as image acquisition in humans and flow phantoms. Human subjects were scanned in accordance with approved Institutional Review Board (IRB) protocols after providing informed consent and passing MRI screenings. Measurements of residual RF saturation were acquired in healthy normal volunteers (ages 20-50) while perfusion data were acquired in elderly volunteers (aged 70 and higher) as part of an NIH study of cognitive deterioration. Patients were divided into normal controls, MCIs and early ADs according to the classification standard [121, 122] from the clinical doctors.

Our exclusion criteria to maximize case reliability and validity were: radiological evidence of structural CNS lesions (e.g., brain infarcts, CNS neoplasms, prior brain surgery), history of strokes or head trauma encephalopathy, consumption of caffeine within 8 hours prior to exam, inability to segment images using semi-automated tools, placement of the labeling plane was not orthogonal to both carotid arteries and/or the difference between left and right carotid arterial mean velocities exceeded 20%, excessive patient motion as evidenced in structural images, excessive image artifact (e.g., hair oil or dental implant), poor scanner performance (e.g. instability or noise).

5.6.2 Magnetic Resonance Imaging

The imaging protocol is described below:

Sagittal Localizer: A rapid sagittal T_1-weighted image was performed to determine patient position.

Multi-slice CASL: Multi-slice CASL used Alternating Single and Double adiabatic inversions (ASD) [61]. Due to the hardware limitations associated with the clinical scanner, the irradiations were applied using a 44 pulse train with an 85 ms period and 94% duty cycle for ASD, In addition, the maximum B_1 was limited to 50 mG. Amplitude modulation of DAI waveforms caused the B_1 for each site (or sideband) to be half of the waveform amplitude. The DAI control was amplitude modulated (AM) at 125 Hz. The label was typically applied 10 cm below the center of the imaging volume, near the cervicomedullary junction, based on a coronal MRA to ensure the labeling plane orthogonal to carotid flow.

ASD employed a 19-slice EPI acquisition (64×64 matrix, 20 cm FOV, 5 mm thick, 0 spacing, TE: MinFull 21 ms TE with ramp-sampling, 76kHz effective receiver bandwidth (rBW),

1 s acquisition time, 700 ms transit delay, 90^0 flip angle), with a sequential superior to inferior slice acquisition order. The pulse sequence was repeated 50 times for ASD for signal averaging.

Residual MT: Residual off-resonance RF saturation used the modified muti-slice CASL sequence except the ASD inversions were applied above the center of the imaging volume (the offsets were from 7 cm to 10 cm) to obtain the same saturation effects but avoid labeling the blood (see the details from Chapter 3). These measurements were performed separately from the regular elderly perfusion measurements.

B_1 maps: Multislice B_1 map data were acquired for 20 slices (the same 19 slices as in the CASL, plus the labeling plane) using regular EPI (TR: 8 s and TE: MinFull 28ms, rBW: 62.5 kHz) with varying nutations (20 different flip angles varying from 18-189^0 in increments of 9^0) [90].

Velocimetry: Phase Contrast (PC) Cine data were acquired at the labeling plane using a fast gradient-recalled echo sequence (TE: MinFull, FA: 30^0, FOV: 20 cm, Thickness: 5mm, Matrix: 256 x 128, rBW: 31.2 kHz). The sequence generated phase maps and the structural images for 20 cardiac phases.

Structural Images: Coronal T_1-weighted spoiled gradient-recalled echo (SPGR) images covering the whole brain were acquired (124 slices with Matrix: 256 × 192; Thickness: 1.5 mm and zero spacing, TE: min Full, TR: 25 ms, FOV: 24 x 18 cm, rBW: 16 kHz).

5.6.3 Image Processing & data analysis

Image Reconstruction: EPI images were constructed off-line from the raw k-space data P-files using a reconstruction program written in C. The reconstruction program converts the ramp-sampled EPI data to a regular square matrix, sorts k-space lines and performs the Fourier Transformation of k-space data.

Image motion correction and segmentation: EPI and SPGR images were converted to the Analyze format for processing with Statistical Parametric Mapping (SPM2) (Wellcome Department of Imaging Neuroscience). SPM2 image realignment corrected physiologic motion between acquisitions. Non-overlapping volumes that normally appear on the superior slice (1st slice) or the inferior slice (the 19th slice) tend to be discarded in the realignment process. The superior slice was typically discarded by us due to the lack of gray matter content. The SPGR images were then segmented to get 256 × 256 gray matter, white matter, and CSF masks. SPGR images were aligned to the mean images to determine the warping parameters. The warping parameters were applied to the gray and white matter masks to obtain gray and white matter masks in the EPI images (64 x 64).

Signal percentage differences: For each repetition, the signal difference was calculated voxel-by-voxel by the subtraction of the label image from its corresponding control image. The signal difference and control image were averaged for all repetitions for improved SNR. The signal percentage difference image ($\Delta M(t)/M_C$) was obtained by dividing the difference image by the control image. The mean values of percentage differences for gray and white matter were fitted separately for left and right side of the brain by using a normal distribution function. The fitting was used to get rid of the effects of intraluminal signals from the large vessels since a very small percentage of intraluminal signal may exist for postlabeling delay of 700 ms [54]. The residual MT measurement ($S_{\Delta MT}/M_C$) for each slice was calculated in the same manner as $\Delta M(t)/M_C$. The corrected signal percentage difference image (($\Delta M(t)- S_{\Delta MT}$)/$M_C$) was obtained by subtracting the residual MT from the signal percentage difference image.

B_1 maps: B_1 map data were fitted on voxel-by-voxel basis to the three-parameter sine model by using a nonlinear least square algorithm, the three-parameter model is as follows:

$$y(t) = a + b\sin(Ct) \tag{5.25}$$

B_1 maps of all slices were calculated including the labeling plane (at the carotids) from the parameter C in Equation (5.25):

$$B_1 = 0.146/\pi \times C/90^0 \times F \tag{5.26}$$

where F is 43^0 and 30.5^0 for label and control respectively.

T_1 maps: T_1 map data were fitted on a voxel-by-voxel basis to the three-parameter model:

$$y(t) = a + b \cdot e^{-t/T_1} \tag{5.27}$$

Blood velocities of carotids: Carotids were identified from the phase contrast (PC) cine velocimetry maps and the blood velocities of carotids were calculated as a function of cardiac phase. The blood velocities of left and right carotids were calculated, respectively, by averaging the corresponding velocities from different cardiac phases.

Tissue-to-arterial ratio correction: MT effects due to off-resonance RF saturation were calculated by Equation (3.4), which takes the B_1 map and the off-resonance frequency of each slice as input parameters. The tissue-to-arterial blood magnetization ratio was calibrated by Equation (5.15).

Labeling inversion efficiency: The inversion efficiencies α_{eff} in the left and right internal carotid arteries were calculated for each subject based on B_1 maps and blood velocities at the label plane by Equation (4.5).

Convolution $k_{Is}(t)$: The theory of interslice convolution function was introduced in Section 5.5.2. Polynomial fits were performed on CASL difference signals to filter out extreme values. We determined the maxima of the polynomial fit instead of calculating the maxima directly from the CASL difference signals. The value of Equation (5.20) at $t = t_z + \tau$ needs to be calculated to calibrate the convolution $k_{Is}(t)$. The calculation of the value requires the value of

T_{1b} and T_{1t}. T_{1b} was calculated based on the individual hematocrit. T_{1t} was calculated as the average T_1 of gray matter T_1 map.

CBF map: Each perfusion map was obtained from Equation (5.12) by using the corrected signal percentage difference map $(\Delta M(t)-S_{\Delta MT})/M_C$, tissue-to-arterial ratio (M_C/M_a^0), labeling inversion efficiency (α_{eff}) and convolution $k(t)$. A representative brain perfusion is shown in Figure 5.7. Only gray matter perfusion was used for the CBF analysis because of the low perfusion SNR and the long tracer arrival time of white matter.

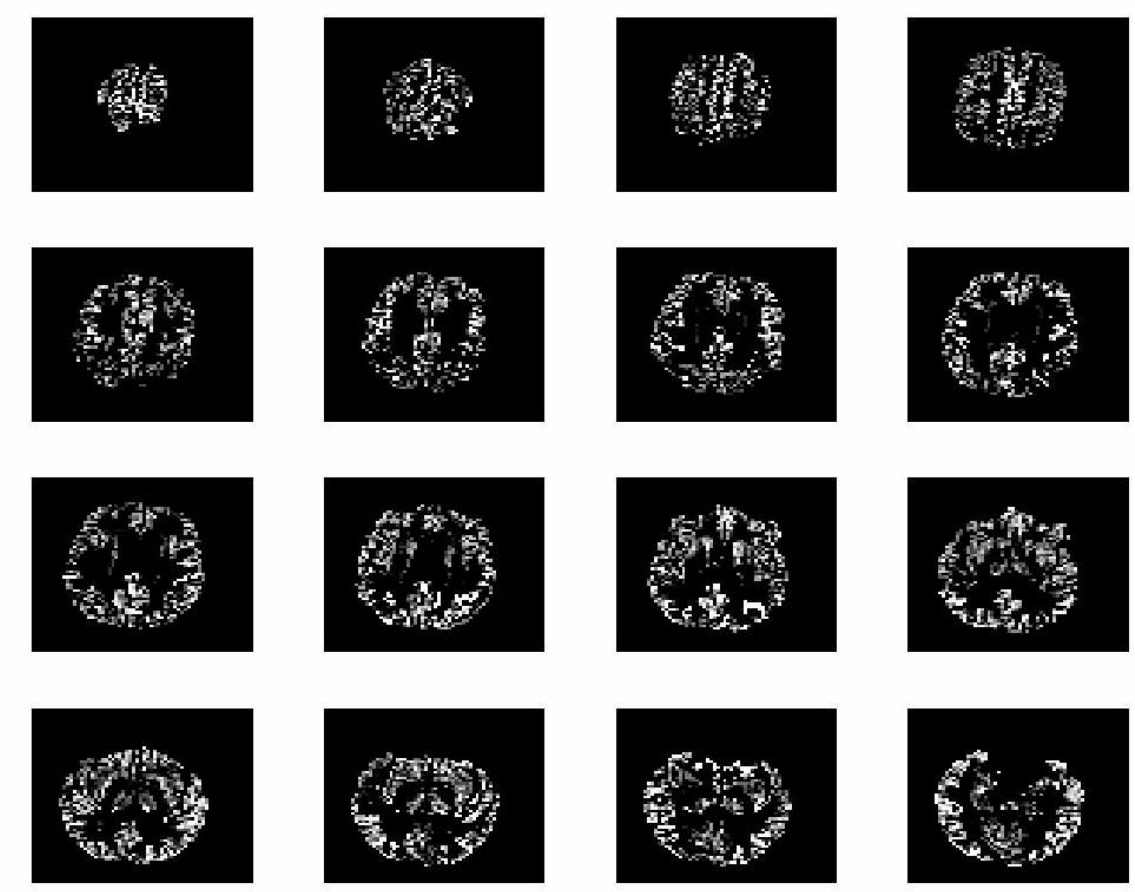

Figure 5.7. Representative CBF maps from one subject for image slices 3 through 18.

5.7 SENSITIVITY OF PERFUSION AND ΔM SIGNAL TO PARAMETERS

By combining Equation (5.12) and (5.17), we have

$$f = \frac{\frac{\Delta M(t) - S_{\Delta MT}}{M_C}[1-(1-MT)e^{\frac{-(w+\Delta t_{acq})}{T_{1t}}}]}{2\Lambda\alpha_{eff}k_{ex}(t)} \tag{5.28}$$

The perfusion signal depends on the parameters $t_z, T_{1t}^{'}$, T_{1b}, α_{eff}, Λ. The inaccuracies of the parameters will propagate to produce errors in the perfusion values. The relative error in perfusion was calculated using the Equation (5.28) by varying each parameter by a certain percentage. The assumed values are based on the average value from our subjects: t_z = 1.15 s, T_{1t} = 1.06 s, T_{1b} = 1.41 s, α_{eff} = 0.83, Λ = 1.2.

The propagated error in the perfusion measurement for each parameter is shown in Figure 5.8. For the acquisition time 4.6 s, the parameters must be known to the following accuracy: t_z: 5.8%, T_{1t}: 5.5%, T_{1b}: 6.6%, α: 5.1%, Λ: 5%, while for the measurement time 5 s, the parameters must be known to the following accuracy: t_z: 18.6%; T_{1t}: 4.9%; T_{1b}: 5.6%; α: 5.1%; Λ: 5% for less than 5% error (an acceptable limit) in perfusion measurements in gray matter. The inversion efficiency α and Λ yield large errors (5%) regardless of the measurement time. It is important to accurately determine α and Λ because they have a large effect on the perfusion measurements. The effect in the parameters T_{1t}, T_{1b} and t_z varies with the measurement times. As the longer delay is inserted before the acquisitions, the perfusion is more sensitive to T_{1t} and T_{1b} variations, but less sensitive to t_z variations.

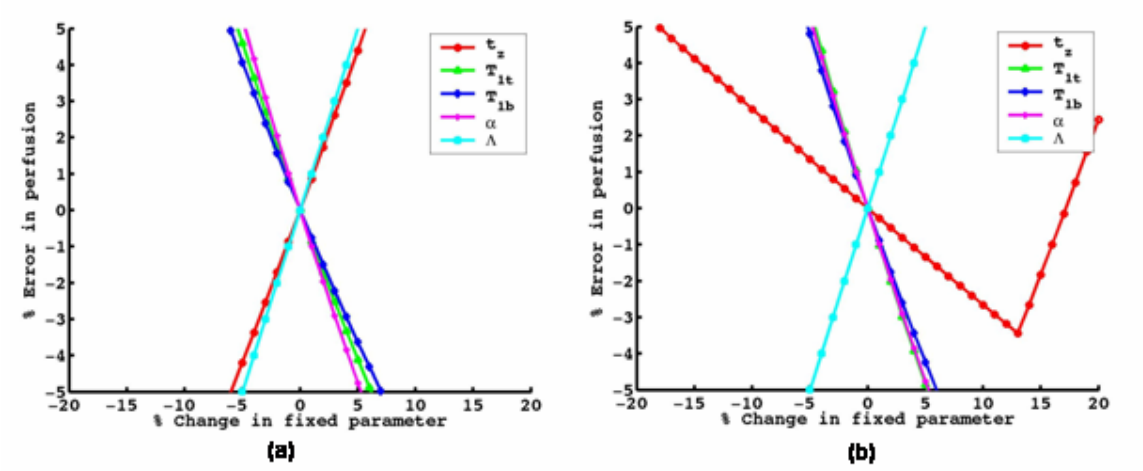

Figure 5.8. Propagation errors in perfusion measurements to parameters: tz, T1t, T1b, α, Λ. Acquisition time is (a) 4.6 s and (b) 5 s.

To compare the sensitivity of the CASL perfusion signal to errors in t_z, T_{1t} and T_{1b}, the slope of ΔM with respect to these parameters was calculated using a relatively large range of t_z and acquisition time t. The ratio of change in ΔM to 0.1 s error in the corresponding parameters was displayed as a function of t_z (Figure 5.9). The ΔM signal is more susceptible to T_{1b} variations and less susceptible to T_{1t} variations as the tissue takes a longer time to arrive in the tissue. The change in susceptibility due to the difference in arrival time is because the labeled blood tracer takes longer to enter into the tissue in the longer arrival time than in the shorter arrival time.

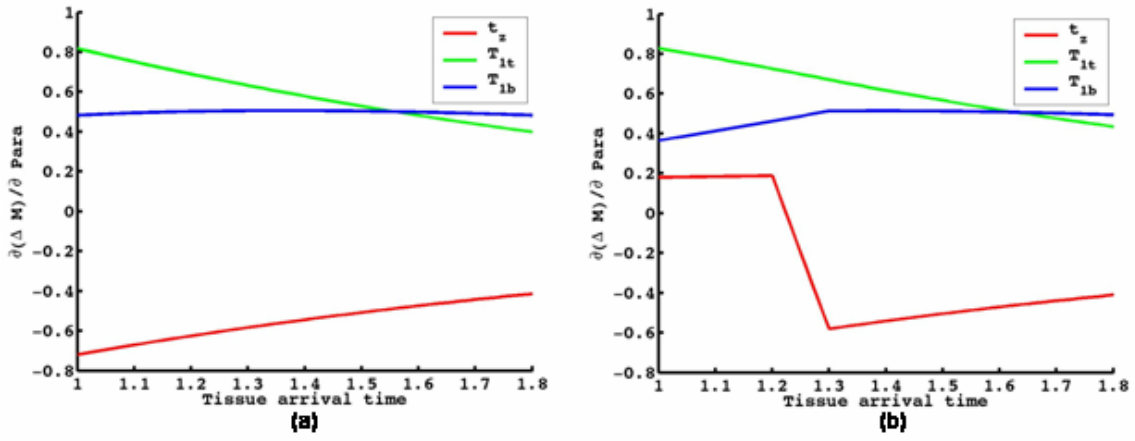

Figure 5.9. Sensitivity of ΔM to parameters t_z, T_{1t}, T_{1b} as a function of t_z. Acquisition time is (a) 4.6 s and (b) 5 s.

The ratio of change in ΔM to 0.1 s error in the corresponding parameters was displayed as a function of the acquisition time t (Figure 5.10). The ΔM signal is less susceptible to the arrival time t_z as the longer delay is inserted before the image acquisition. The image must be acquired early (i.e., before all the blood tracers arrive in the imaging volume) to measure the blood tracer arrival time during the CASL experiment.

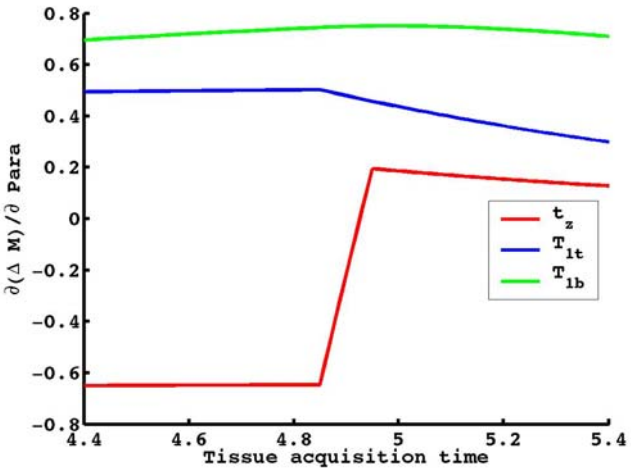

Figure 5.10. Sensitivity of ΔM to parameters t_z, T_{1t}, T_{1b} as a function of t.

5.8 SUMMARY OF CASL PERFUSION MODEL

We summarize our research achievements for the CASL perfusion model by analyzing the previous issues in CASL in Table 5.5. We improved the perfusion quantification by inserting a short postlabeling delay, modeling off-resonance effects & residual off-resonance saturation effects, measuring the individual inversion efficiency, estimating the arrival time, verifying the exchange model, and optimizing the acquisition order.

There are limitations to our perfusion quantification. First, as we indicated in the section 5.5.4, more accurate perfusion measurements requires knowing the arrival times at the voxel level. However, the SNR in difference images only allow us to calculate the cluster-wise arrival time map. Second, the evidence of exchange means that we have an admixture of partially-saturated macromolecules and chemical exchange. There is no literature addressing these perturbations. The perturbations complicate the kinetics. The effects of chemical exchange are not considered in our CASL perfusion model, the effects are not addressed in other CASL models either.

Table 5.5. Summary of CASL perfusion issues, our achievements and significance.

Topics	Issues from Previous Studies	Research Achievements	Significance
Postlabeling Delay	Used long delay: reduces the signal amplitude and SNR, time cost is large, need two 8-minute acquisitions to cover the brain, and is limited by tracer T_1 relaxation. Recent 3D-acquisition technique takes lesser time, but very motion sensitive.	Used shortened delay: only need one acquisition to cover the whole brain.	Increased perfusion signal amplitude and SNR; time cost is reduced to almost half; whole brain in one acquisition reduced possible motion; Increased complexity of quantification.
MT Effects & Residual Off-resonance Saturation Effects	Assumed negligible residual off-resonance saturation effects.	Established a dual-Lorentzian MT model to fit the experimental data and model the residual effects from *in vivo* measurements. Apply models to correct individual data sets based on their experimental conditions (B_1, label distance) **See Chapter 3.**	MT, residual off-resonance saturation, and nonadiabatic effects vary between subjects and experiments. These effects can be significant especially for short postlabeling delays.
Inversion Efficiency	Assumed that it is constant.	Established an analytical model and validated with the experiments. Use the model to measure it for	Significantly varies between subjects and experiments. Offer the researcher the ability to correct the perfusion

		each subject. **See Chapter 4.**	quantification due to the variance of clinical conditions.
Arrival Time	Assumed the inserted postlabeling delay is long enough for the labeling blood to be delivered to the imaging slice. Measuring the arrival directly doubles the acquisition time.	Measured the arrival time indirectly for each individual subject.	Get the arrival time of each individual subject measured at the mean time. Avoid wasted time after tracer arrival (early arrivals of tracer) or insufficient postlabeling delay (e.g. for diseased subjects)
Acquisition Order	From inferior to superior	From superior to inferior.	Keep the blood tracer intact and alleviate the off-resonance saturation effects and crosstalk.
Exchange vs. no-exchange model	Use no-exchange model without validation.	Use the interslice signal to verify whether the blood tracer exchange occurs or not.	Capture the kinetic model more accurately and improve the perfusion quantification.

6.0 IMPACT OF IMAGE REGISTRATION ON PERFUSION ANALYSIS

6.1 INTRODUCTION

Brain perfusion is an important hemodynamic parameter. The changes of perfusion in the development of Alzheimer 's disease (AD) is crucial for the detection of early makers. Most of the studies used a conventional region of interest (ROI) to evaluate regional changes. The ROI technique is not always automated and might be intrinsically prone to error because of operator *a priori* assumptions and subjective choice. The ROI analysis may lack sensitivity because the regional changes within the defined ROI are diluted when averaged across the ROI [123].

Voxel-based morphometry (VBM) makes no assumption on the topography of regional changes, and compares changes at the voxel level to overcome the insensitivity of the ROI approach. VBM is an effective approach to obtain an even-handed and global assessment of perfusion changes throughout the brain. Voxel-based morphometry (VBM) involves spatial registration of images into a common stereotactic space, voxel-wise comparisons, and biostatistical analysis [124]. Spatial registration transforms the brain volume from each subject to the same stereotactic volume referred herein as *the reference volume* to correct for anatomical variability. Biostatistical results are based on spatial registration methods. Therefore, it is essential to assess the impact of spatial registration approaches on the biostatistical analysis of cerebral blood flow when VBM is applied to perfusion MRI.

Spatial registration of elderly brains is a challenging issue. Whole brain volume and fine cortical structures have large variability between individuals that may change at different atrophy rates as people age. Different brain image voxels may deform or warp to varying degrees during the brain registration. The deformation variability across cortical structures requires an accurate registration method to match the cortical structures between each individual brain and the reference volume. A poor registration method will bias group comparisons. Therefore, the performance of spatial registration on elderly brains has an important effect on group comparisons when applied to functional imaging.

A variety of software registration packages are widely used to process images at brain imaging laboratories. The most popular registration components for brain image analysis are statistical parametric mapping (SPM) [14, 123, 125-133] and automated image registration (AIR) [134, 135]. SPM uses a geometric transformation model with low-dimensional discrete cosine transformation (DCT) basis functions; while AIR uses a polynomial basis functions as its transformation model. The registrations of both SPM and AIR primarily model the low-frequency deformation and ignore the high-frequency (i.e., high-spatial resolution) information. The spatial registration methods of SPM or AIR do not attempt to match every cortical feature, but merely correct for global brain shape differences [124].

A fully deformable model (FDM) was developed with higher degrees of freedom for deformation. FDM combines piecewise-linear and dense voxel-by-voxel geometric transformation models, and computes the displacement of each voxel with minimal constraints [65]. FDM has the potential precision to match each cortical feature with substantial fine-scale deformation. FDM was shown more accurate than affine linear methods at hippocampus segmentation in AD patients [136]. FDM also demonstrated a more reliable mean blood

oxygenation-dependent contrast (BOLD) functional MRI (fMRI) signal in the young subjects' right hippocampus and right anterior cingulate cortex [137]. In these studies, FDM was more accurate than affine methods for segmenting two cortical structures in the subject space and improving structural and functional MRI signals in those two region-of-interests (ROI).

No studies to-date have compared the performance of FDM and SPM/AIR registration methods for the correspondence of cortical structures from the subject to the reference space or assessed the impact of the registration methods on the voxel-by-voxel group analysis of elderly brain functional imaging including perfusion MRI (pMRI). Therefore, we conducted quantitative comparisons to: 1) investigate the accuracy between SPM/AIR and FDM registrations regarding the correspondence of brain anatomical regions from the individual brain with hand-drawn ground-truth regions in the reference volume; and 2) globally assess the effects of registration methods on the biostatistical analysis of pMRI of elderly brains.

6.2 THEORETICAL FORMULATION

6.2.1 Problem formulation

Given a 3-dimensional subject volume *f*, a reference volume *g,* and a perfusion volume *p* which is aligned with *f*, where *f(x, y, z)*, *g(x, y, z)* and *p(x, y, z)* represent the image intensity at the voxel location [*x, y, z*], respectively. Our goal is to estimate the parameters of a geometric transformation which optimize the match between the subject volume *f* and the reference volume *g*, and then use the resultant transformation to relate the perfusion volume *p* to *q*. The reference volume *g* and subject volume *f* are related to each other by the following model:

$$f(t_\alpha(x,y,z)) = s_\beta(g(x,y,z)) + \varepsilon \tag{6.1}$$

The geometric transformation model t_α transforms voxel locations in the reference volume to voxel locations in the subject volume; its behavior is dependent on a parameter of vector α. In the case of affine geometric transformation, α will have entries for a translation, scaling and rotation along three Cartesian axes. The intensity transformation model s_β is needed to accommodate the signal difference between the subject volume and reference. The simplest case is that the intensity transformation is a linear scaling of signal intensity, for which β has only one entry, i.e. scaling factor. ε is the error term. In our perfusion transformation problem, we first estimate parameters α and β by optimization techniques, and then return an estimate $\tilde{q}$ of q by applying p to t_α**:**

$$\tilde{q}(x,y,z) = p(t_\alpha(x,y,z)) \tag{6.2}$$

6.2.2 Registration methods

The registration methods are essentially an optimization problem. The objective of the optimization is to determine the geometric transformation model t_α and the intensity transformation model s_β for which the cost function $c(t_\alpha, s_\beta)$ is minimized. The simplest case for the cost function $c(t_\alpha, s_\beta)$ is the sum of squared differences between the model and the reference volume:

$$c(t_\alpha, s_\beta) = \sum_i (f(t_\alpha(x_i, y_i, z_i)) - s_\beta(g(x_i, y_i, z_i)))^2 \tag{6.3}$$

where (x_i, y_i, z_i) represents the coordinates of the ith sampled point (to reduce the computation cost, not all image voxels are sampled). Usually, there are many entries in α and β, yet an

exhaustive search through the whole parameter space is impossible. An iterative search is normally used to modify the parameters for each iterative step.

AIR: The first stage of AIR estimates a 12-paramter affine geometric transformation and a single scaling parameter for the intensity transformation. That is, $t_\alpha(x,y,z) = A[x,y,z,1]$ and $s_\beta(g(x,y,z)) = \beta \cdot g(x,y,z)$. The 12-parameter estimation of A and scalar β is done using a Gauss-Newton algorithm. For the second stage, the basis functions of the geometric transformation model are a polynomial function of degree M. The geometric transformation model [138] is represented by:

$$t_\alpha(x,y,z) = \sum_{i=0}^{M}\sum_{j=0}^{M}\sum_{k=0}^{M}[b_{1ijk}, b_{2ijk}, b_{3ijk}] \cdot x^i y^j z^k \qquad (6.4)$$

The coefficients b_{ijk} are the geometric transformation parameters, and are estimated by a Gaussian-Newton optimization procedure. The sampled points are chosen as every K-by-K-by-K^{th} voxel.

SPM: The first stage of SPM also estimates a 12-parameter affine geometric transformation and single scaling parameter for the intensity transformation model as in AIR. In the second stage, the geometric transformation model [139] adopts the basis function of discrete cosine transformation (DCT) as its basis function. i.e.

$$t_\alpha(x,y,z) = \sum_{i=0}^{M}[b_{1i}, b_{2i}, b_{3i}] \cdot c_i(x,y,z) \qquad (6.5)$$

The coefficients b_i are the geometric transformation parameters, and the functions $c_i(x,y,z)$ are the basis functions of the DCT. The parameter estimation of both stages uses a Gaussian-Newton algorithm. The sampled points are chosen as every K-by-K-by-Kth voxel as in AIR.

FDM: The first stage of FDM [65] estimates the parameters of an affine geometric transformation as in AIR and SPM. The second stage is a piecewise-linear model, which takes

the estimated parameters from the first stage as a starting point. In the piecewise-linear transformation, a set of control points [x_i, y_i, z_i] is chosen and displacements of the control points [Δx_i, Δy_i, Δz_i] are estimated. The control points are located on a 3D rectangular grid that covers the reference volume. The method first estimates displacements for a 2×2×2 grid of control points, and uses these displacements as the starting points to estimate displacements of 3×3×3 grid of control points, and so on by the Levenburg-Marquardt method. Each voxel point [x, y, z] in the reference volume is bounded by eight control points: [x_l, y_l, z_l], [x_h, y_l, z_l], [x_l, y_h, z_l], [x_l, y_l, z_h], [x_h, y_h, z_l], [x_l, y_h, z_h], [x_h, y_l, z_h], [x_h, y_h, z_h]. The piecewise-linear geometric transformation of each voxel is a trilinear interpolation of the displacements of the control points that bound it. That is, (6.6)

$$t_\alpha(x,y,z) = [x,y,z] + [\alpha_x \cdot \Delta x_l + (1-\alpha_x)\cdot \Delta x_h, \alpha_y \cdot \Delta y_l + (1-\alpha_y)\cdot \Delta y_h, \alpha_z \cdot \Delta z_l + (1-\alpha_z)\cdot \Delta z_h] \text{ w}$$

here $\alpha_x = (x_h - x)/(x_h - x_l)$, $\alpha_y = (y_h - y)/(y_h - y_l)$ and $\alpha_z = (z_h - z)/(z_h - z_l)$.

The third stage is a dense voxel-by-voxel transformation, which takes the estimated parameters from the second stage as a starting point. For the transformation stage, the displacements [Δx, Δy, Δz] of each voxel [x, y, z] in the atlas volume are the parameters to estimate. i.e.

$$t_\alpha(x,y,z) = [x,y,z] + [\Delta x, \Delta y, \Delta z] \quad (6.7)$$

The displacements can be estimated by a first-order Taylor expansion of Equation (6.1) by replacing t_α by Equation (6.7). The displacements only depend on the volume g and $s_\beta(g)$, and their gradients, and can be computed iteratively at each voxel until the algorithm converges.

FDM's intensity transformation model is a linear function, i.e. $s_\beta(g) = a \cdot g + b$. The parameters, a and b, are estimated from the simple heuristic that the mean and variance of the intensity distribution of the reference volume should match those of the subject volume. The sample points are chosen for a piecewise-linear stage as a random selection of K voxels.

In summary, the basis function phases of AIR, SPM, and the piecewise-linear phase of FDM are referred as "semi-deformable" methods since their transformations do vary spatially but in a gradual, constrained, low-dimensional way. While the dense voxel-by-voxel phase of FDM was called as a "fully-deformable" method due to its fully unconstrained geometric transformation. An example showing the use of these techniques to register a pair of images is shown in Figure 6.1 [140]. In other words, FDM uses more degrees of freedom to geometrically deform the subject volume to match the reference volume.

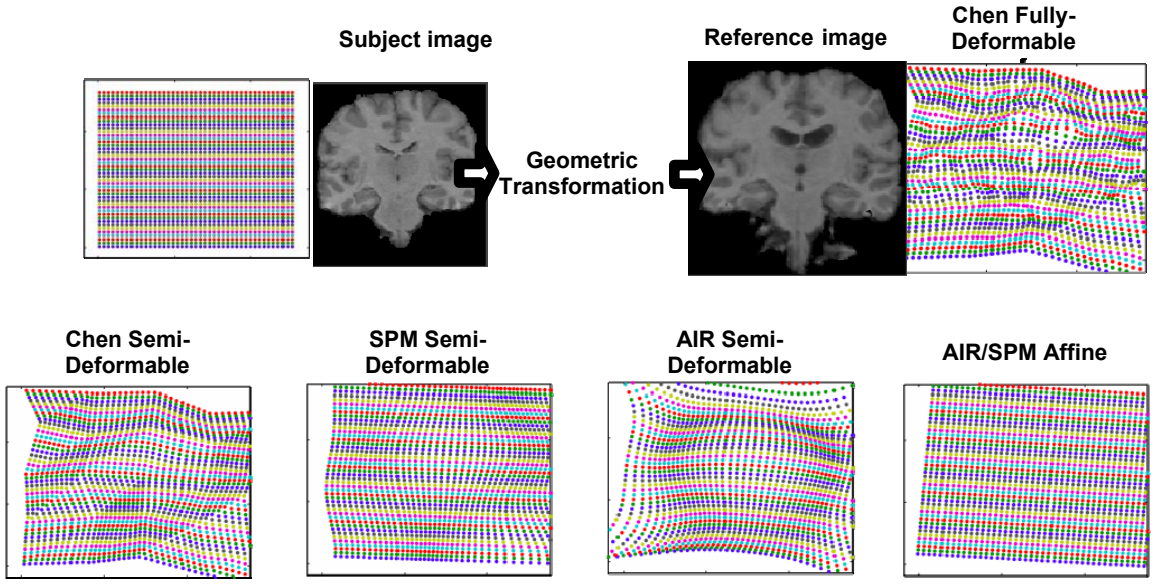

Figure 6.1. Example deformations produced by fully deformable, semi-deformable, and affine registration techniques. The subject volume is registered to the reference volume using the corresponding algorithm. The colored dots show the geometric positions of voxels in the shown slice of the moving image before and after deformation by each of the methods. The transformations produced by the AIR affine method and the SPM affine method were almost identical.

The deformations from SPM/AIR are restricted to the lowest spatial frequencies of the basis function, and so high-frequency deformations cannot be modeled. Therefore, these nonlinear registration methods do not have the potential precision compared to methods with more degrees of freedom. This indicates that SPM/AIR is unsuitable for attempting fine matches between fine cortical structures. The constrained registrations from SPM/AIR assume that the

reference resembles a warped version of the subject volume. However, the most commonly available reference is based on the young healthy brains. Most of the cortical structures in elderly brains (especially diseased ones) shrink at different rates, and the ventricles are enlarged compared to younger brains. Hence a fully-deformable, high-quality registration technique is necessary to compensate for the changing rate of different cortical structures so that the choice of the reference volume does not bias the registration result. The registration methods of SPM/AIR may not be adequate to match fine cortical structures from different subjects based on the above reasons.

6.3 SUBJECTS AND METHODS

6.3.1 Database of Subjects

The Pittsburgh Cardiovascular Health Study (CHS) Cognition Study was a population study, conducted in 2002/03 to determine the incidence of dementia and MCI. These participants were evaluated for cognitive functions and classified as a probable Alzheimer's disease (AD) [141], probable mild cognitive impairment (MCI) [121], or normal cognitive control. One hundred eighty eight participants (referred herein as the subject database) had an MRI of the brain in 2002-03.

6.3.2 MR imaging

All data were acquired using a 1.5 T GE Signa system (Milwaukee, WI, LX) after each subject provided informed consent either directly or by their caregiver and passed the Society of

Magnetic Resonance Imaging standardized MRI screenings. Coronal T_1-weighted spoiled gradient-recalled echo (SPGR) volume covering the whole brain were acquired (124 slices with Matrix: 256 × 192; Thickness: 1.5 mm and zero spacing, TE: min Full, TR: 25 ms, FOV: 24 x 18 cm, rBW: 16 kHz). The SPGR volumes were regrided into 240 × 186 × 180 matrix with voxel size 1 × 1 × 1 mm^3. For the quantitative perfusion map, blood flow velocities, perfusion rates and T_1 relaxation times were measured in each subjects using phase contrast (PC) Cine, multi-slice CASL, and saturation recovery MRI, respectively. Multi-slice CASL used Alternating Single and Double adiabatic inversions (ASD) [61](3.7 s pulse train at 92% duty cycle) and ramp-sampled echo-plane imaging (EPI) to acquire 19 contiguous axial slices (64×64 matrix, 20cm field-of-view, 5 mm slice thickness, 0 spacing, 21 ms echo time (i.e., minimum full), 76 kHz effective receiver bandwidth, 1 s acquisition time, 700 ms transit delay, 90^0 flip angle, 50 signal averages). Images were acquired sequentially from superior to inferior brain to avoid RF perturbation of the endogenous tracer as it moved superiorly into the brain and to minimize intensity discontinuities associated with interleaved acquisitions. The inversion efficiencies in the internal carotid arteries were calculated for each subject based on B_1 maps and phase contrast (PC) cine velocimetry at the label plane [142].

6.3.3 Registration Methods

In this section, we will compare the registration methods between SPM2 and FDM. We chose SPM over AIR for this comparison due to the former's increased popularity in medical image processing.

6.3.3.1 Qualitative evaluation of registration accuracy

A subject was randomly selected from the subject database to evaluate the accuracy of the two registration methods qualitatively. We chose two cortical structures (hippocampus and thalamus) for comparisons. We registered the reference volume colin27 (a standard high-resolution reference volume, the averaged MRI brain volume from 27 scans of the Colin brain [143]) to the subject SPGR volume, and used the resultant geometric transformation parameters (for SPM2 and FDM respectively) to transfer the hippocampus and thalamus masks from the reference volume to the subject volume. The resultant hippocampus and thalamus masks were overlaid on the subject volume (in Figure 6.2). The hippocampus detected from SPM registration is shifted up from its true anatomical position, and the thalamus is mislocated within the ventricle. However, both regions detected from FDM are located correctly in their anatomical regions. Therefore, FDM was more accurate for delineating fine cortical structures than SPM2's registration method in this example.

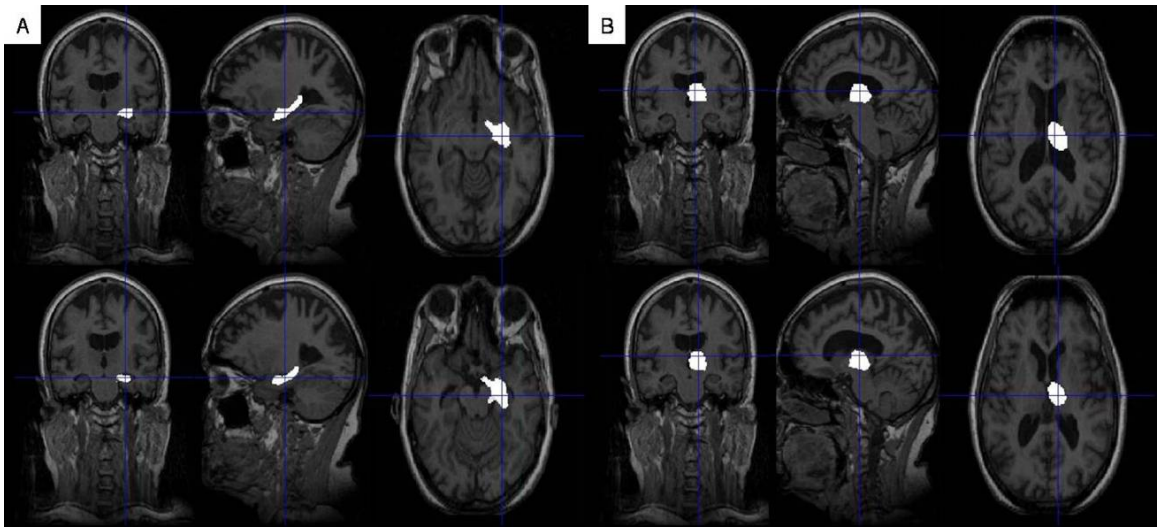

Figure 6.2. Comparison of automatic ROI detection from SPM2 (top row) and from locally FDM (bottom row) for the left hippocampus (A) and left thalamus (B). ROIs are shown projected onto the individual's space (SPGRs). Using SPM2, the left hippocampus is shifted up from its true anatomical position while the thalamus is erroneously located within the ventricles.

6.3.3.2 Quantitative assessment of accuracy of registration methods

Ten subjects (mean age 82 ± 3.4: 4 normal controls, 3 MCI subjects, 3 AD subjects) were randomly selected from the subject database. The 10 SPGR volumes were cropped to remove the extracranial regions using the Brain Extraction Tool (BET) of the FSL software package (Oxford Center for Functional Magnetic Resonance Imaging, Oxford University, UK). We chose the standard Montreal Neurological Institute (MNI) brain colin27 (with voxel size $1 \times 1 \times 1$ mm^3) [144] as the reference volume since the colin27 carries high-resolution anatomical brain structures. In the interest of time, five regions (left posterior cingulate gyrus, left cuneus & calcarine, left hippocampus, right thalamus and right putamen) were selected because 1) those structures are biologically important in AD or healthy aging, and 2) the hippocampus and the posterior cingulate gyrus are suspected regions of atrophy and neurological change for AD [14, 20, 34, 145]. Both the left side and the right side of the cortical structures were randomly selected to avoid the biased evaluation of registration methods in favor of only one side of the brain.

The right thalamus and right putamen were traced in axial views; the left posterior cingulate gyrus, left cuneus & calcarine and left hippocampus were traced in sagittal views. The five regions were manually traced for both the reference volume and ten elderly subject SPGR volumes under the supervision of a licensed neurologist. The manually traced regions served as ground-truth region masks (each region mask is a binary 3D volume in which voxels labeled as the region had a value of 1). The region tracing program was written in MATLAB.

All 10 cropped brain SPGR volumes were normalized to the reference volume using SPM2 and FDM. The warping parameters of each subject from the registration were used to warp the five region masks of the subject to the reference space for SPM2 and FDM,

respectively. Two normalized region masks were obtained using: 1) SPM2 and 2) FDM for each region mask of each subject (Fig. 6.3).

We used the overlap ratio to evaluate the agreement between normalized region masks from each method and the ground-truth region masks of the reference volume. Let normalized region mask N_{ij}^{k} be the set of voxels labeled as the cortical structure *j* (*j = 1, ..., 5*) of the *i*th (*i = 1,..., 10*) subject from the registration method *k* (*k=1, 2.* 1 stands for SPM, 2 for FDM), and the ground-truth region mask G_j be the voxels labeled as cortical structure *j* of the reference volume. The overlap ratio of cortical structure *j* of *i*th subject from the method *k* was quantified as:

$$overlap\_ratio(i,j,k) = \frac{|N_{ij}^{k} \bigcap G_j|}{|N_{ij}^{k} \bigcup G_j|}.$$

The range of the overlap ratio is 0 to 1. The overlap ratios evaluate how well the normalized region masks overlap with the ground-truth region masks of the reference volume. The higher the ratio, the better the overlap.

We also calculated the overall overlap ratio from the 10 subjects for each cortical structure *j* to assess the ability of the methods in removing the anatomical variability. The overall overlap ratio was defined as the percentage of voxels that are shared between all subjects for each cortical structure and registration method:

$$overall\_overlap\_ratio(j,k) = \left|\bigcap_{i=1}^{10} N_{ij}^{k}\right| \Big/ \left|\bigcup_{i=1}^{10} N_{ij}^{k}\right|.$$

6.3.3.3 Effects of registration methods on biostatistical analysis of pMRI

Forty-five subjects were selected from the subject database (Table 6.1 shows demographic information for the three study groups). These subjects had an optimal CASL MRI with no

exclusionary criteria: radiological evidence of structural or vascular central nervous system (CNS) lesions, history of strokes, or head trauma encephalopathy; evidence of large disparity in blood flow between hemispheres; poor arterial labeling efficiency or execution, excessive patient motion as evidenced in the structural images; excessive image artifact; or consumption of caffeine within 8 hours prior to exam. The 45 SPGR volumes were also cropped using BET to remove the extracranial regions.

The 45 absolute perfusion (CBF) maps of gray matter were calculated using the tracer kinetic convolution model of CASL [74]. The gray matter CBF map of each subject was transformed to the cropped SPGR space of the subject by the coregistration algorithm of SPM2.

The 45 cropped SPGR volumes were normalized to the reference volume colin27 using SPM2 and FDM. The warping parameters of each subject from the registration were used to warp the corresponding brain gray matter perfusion map to the reference space. Therefore, two normalized gray matter perfusion volumes were obtained for each subject using SPM2 and FDM, respectively (Fig. 6.3).

We smoothed the two normalized gray matter CBF maps (from SPM2 and FDM) of each subject using the same 6 mm Gaussian kernel. Kernel widths of up to 16mm are being used in the literature. Smoothing increases statistical power. The less one smoothes, the less likely it is to obtain significant results. However, the increased statistical power is in the cost of dramatic loss of spatial precision. The worst case senerio is that you many observe the statistical significance in an area with no signal at all (e.g. white matter). Six mm was chosen as the smoothing kernel width since this corresponds roughly to the cross sectional dimensions of the hippocampus and sensitized the analysis to difference at this spatial scale by the matched filter theorem. Biostatistical analysis of the smoothed CBF maps were performed between groups: a)

normal controls and early AD subjects, b) MCI and early AD subjects, and c) normal controls and MCI subjects using a customized one-way ANOVA multiple comparison algorithm on a voxel-by-voxel basis written in MATLAB (MathWorks Inc.). The customized algorithm permitted an ANOVA of those voxels with perfusion values that were morphometrically shared by a majority of subjects in each group to maximize the brain volume coverage. Because of the variability of slice coverage, the algorithm made the voxels from most of the cortex analyzable in the ANOVA. A two-tailed p-value of 0.02 was chosen for the voxel-by-voxel analysis to identify statistically significant differences between groups (referred as the difference maps). The difference maps were further masked using the brain volume mask (i.e. all of the gray matter voxels that have valid perfusion data in a majority of subjects of each group) to avoid a smoothing artifact. SPM subroutines were modified to overlay the masked difference maps to the surface section of colin27 brain.

Clusters displayed on the colin27 brain were thresholded at a correct cluster-level of $P < 0.02$. The cluster-level correction was performed to guard against false positives from multiple comparisons. The correction took into account the voxel-level threshold and the spatial extent of cluster [146].

6.4 RESULTS

Assessment of accuracy of registration methods: The comparisons of the five overlap ratios measured for SPM2 and FDM are shown in Fig. 6.4A. For all regions, FDM gives a higher mean overlap ratio than SPM2. Paired two-tailed t-tests were applied for the overlap ratios obtained from SPM2 vs FDM. The result of the paired t-tests of five overlap ratios is shown in

Table 6.2. The differences in overlap ratios of all five regions were statistically significant (with two-tailed $p < 0.025$), showing FDM transformed the corresponding anatomical cortical structures from the subject space to the reference space more accurately versus SPM2. The overall overlap ratios from all 10 subjects for five cortical structures are shown in Fig. 6.4B. For all five cortical structures, FDM gives a higher overall overlap ratio than SPM2: 12% higher for the left cuneus and at least 97% higher for the other four cortical structures. Therefore FDM provided more precision to overlay the cortical structures between different subjects than SPM2.

Effects of registration methods on biostatistical analysis of pMRI: The results of the CBF biostatistical analysis are illustrated in Fig 6.5. Cluster-level statistics are shown in Table 6.3. With FDM, the total number of voxels with statistical significant change in perfusion is 6112, 2.39 times greater than SPM2. FDM identified almost 3 times more clusters of statistical significance than SPM2 (FDM: 11 clusters vs. SPM2: 4 clusters). We also observed markedly larger sizes (40% or more) of statistically significant clusters than SPM2 for most clusters with the exception of normal controls vs. MCI subjects.

For normal controls vs. MCIs, the left and right posterior cingulate area yielded one cluster in SPM. The total size of the two separate clusters from FDM was still 5% larger than the one cluster from SPM, while the sizes of the right superior parietal lobe measured from FDM and SPM2 were almost equal. Not only were small clusters of statistical significance from FDM registration not observed in SPM, but a large cluster (right posterior cingulate gyrus for normal controls vs. AD subject, 1155 mm^3) was also not detected in SPM2.

6.5 DISCUSSION

SPM/AIR only corrects for the global brain shape differences in term of the overall mathematical characteristics of these registration algorithms. Their registration methods do not enforce a match between every brain cortical structure because they use only low frequency deformations. However, the goal of our quantitative perfusion analysis is to deform the subject volume so that each subject cortical structure aligns as well as possible with the reference cortical structure, regardless of how heavily each voxel of the subject volume needs to be deformed. FDM is a method with a fully unconstrained condition of deformation.

Our experimental results also verify the deformation degrees of these registration algorithms. Figure 6.1 shows that FDM can account for substantial warps by increasing the volumes of some voxels and shinking the volumes of others. Our results also demonstrate that the high-dimensional FDM algorithm is superior than SPM2 for transforming anatomical structures from the subject to reference space. Previous studies showed that FDM segmented hippocampus and anterior cingulate gyrus more accurately. However, this result was based on the registration from the template to subject space. We demonstrated not only better performance in the hippocampus registration, but better correspondence of other brain structures from the subject to template space in one unified measure. The overall higher overlap ratios from FDM than SPM2 show that FDM can correct for anatomical variability between subjects better than SPM2.

The improved correction of anatomical variability achieved by FDM increases the biostatistical sensitivity of pMRI variations between different cognitive classification groups. FDM was shown to produce more reliable structural and functional MR signals in the ROIs

(hippocampus and anterior cingulate gyrus). We demonstrate that FDM is more sensitive to CASL perfusion changes for different disease states than SPM2 throughout the cerebrum.

The normalization package of the latest version of SPM (SPM5) reportedly uses a low-dimensional algorithm. Therefore, we expect SPM5 will yield similar normalization performance as SPM2 when compared to FDM. Nevertheless, a quantitative comparison of these techniques is warranted.

One issue is related to the normalization performance regarding to SPM2 and FDM. We chose colin27 brain as our reference volume because the reference volume is a current standard high-resolution template and is widely accessible to the researchers. The high-resolution template is important for the high performance of FDM since the high resolution contains the clear boundaries of cortical structures that assist to determine the displacement of each voxel. On the other hand, colin27 is a young brain template. Therefore, the transformation from each elderly brain to the young template requires more deformation. The high-resolution elderly template is in demand to be developed and the normalization performance based on the to-be-developed template requires further investigation. We would guess that FDM will have better performance than SPM in both registration accuracy and statistical sensitivity based on its higher degree of freedom relative to SPM, but it may not be as significant as what we reported here.

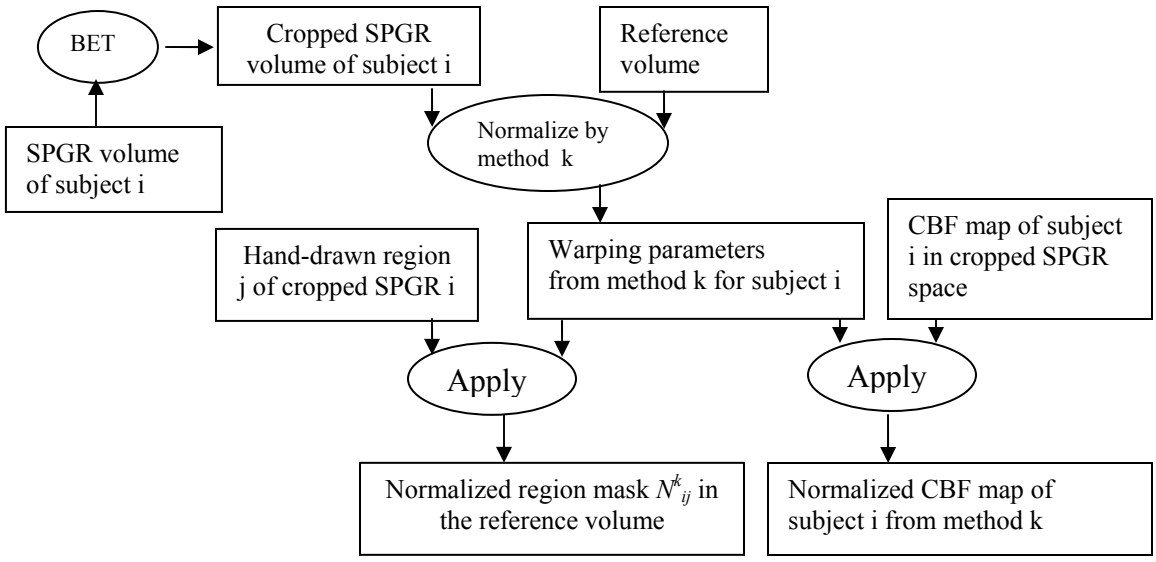

Figure 6.3. Graphical illustration of registration methods in obtaining normalized region mask and normalized CBF maps.

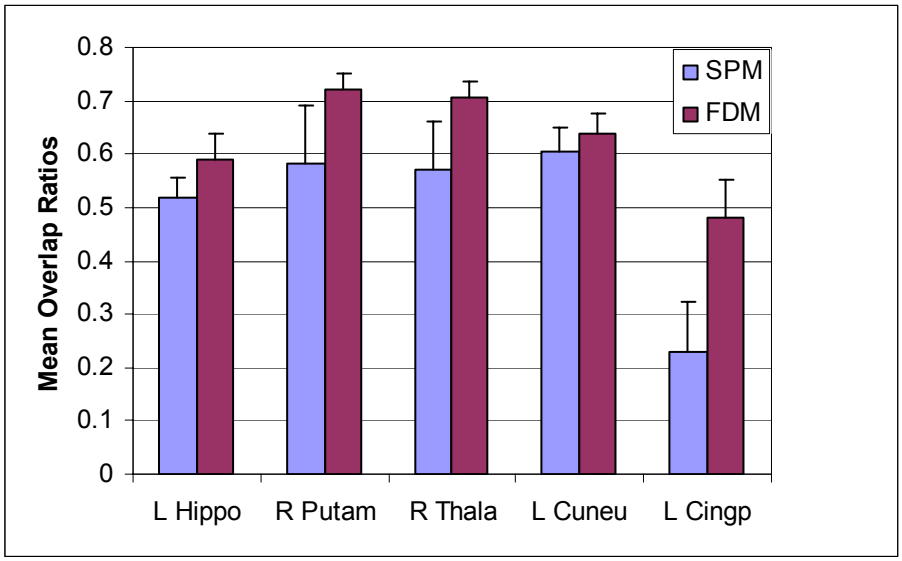

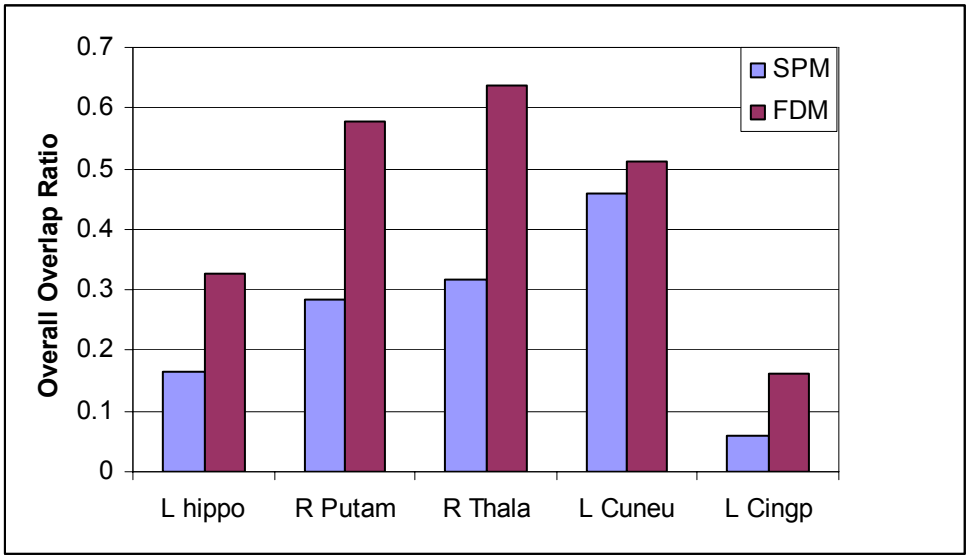

Figure 6.4. A) Mean overlap ratios and B) Overall overlap ratios of five cortical regions: left hippocampus (L Hippo), right putamen (R Putam), right thalamus (R Thala), left cuneus (L cuneu) and left posterior cingulated gyrus (L cingp) over 10 subjects by SPM and FDM.

Table 6.1. Characteristics of study Groups

Characteristic	Controls	MCIs	ADs
# of Cases	16	14	15
Age	82.4 ± 3.8	83.5 ± 3.4	83.0 ± 3.1
Female/Male	5/11	4/10	6/9

3MSE	95.1 ± 4.7	89.1 ± 10.9	87.4 ± 9.5

Table 6.2. Statistical comparison of overlap ratios of five selected regions

Regions	Mean overlap of SPM2	Mean overlap of FDM	t-values	two-tailed p-values
Left Hippocampus	0.5166	0.5881	-4.7154	0.0011
Right Putamen	0.5811	0.7199	-3.7484	0.0046
Right Thalamus	0.5706	0.7045	-4.5973	0.0013
Left Cuneus	0.6046	0.6398	-2.7655	0.0219
Left Posterior Cingulate	0.2288	0.4797	-7.2176	0.00005

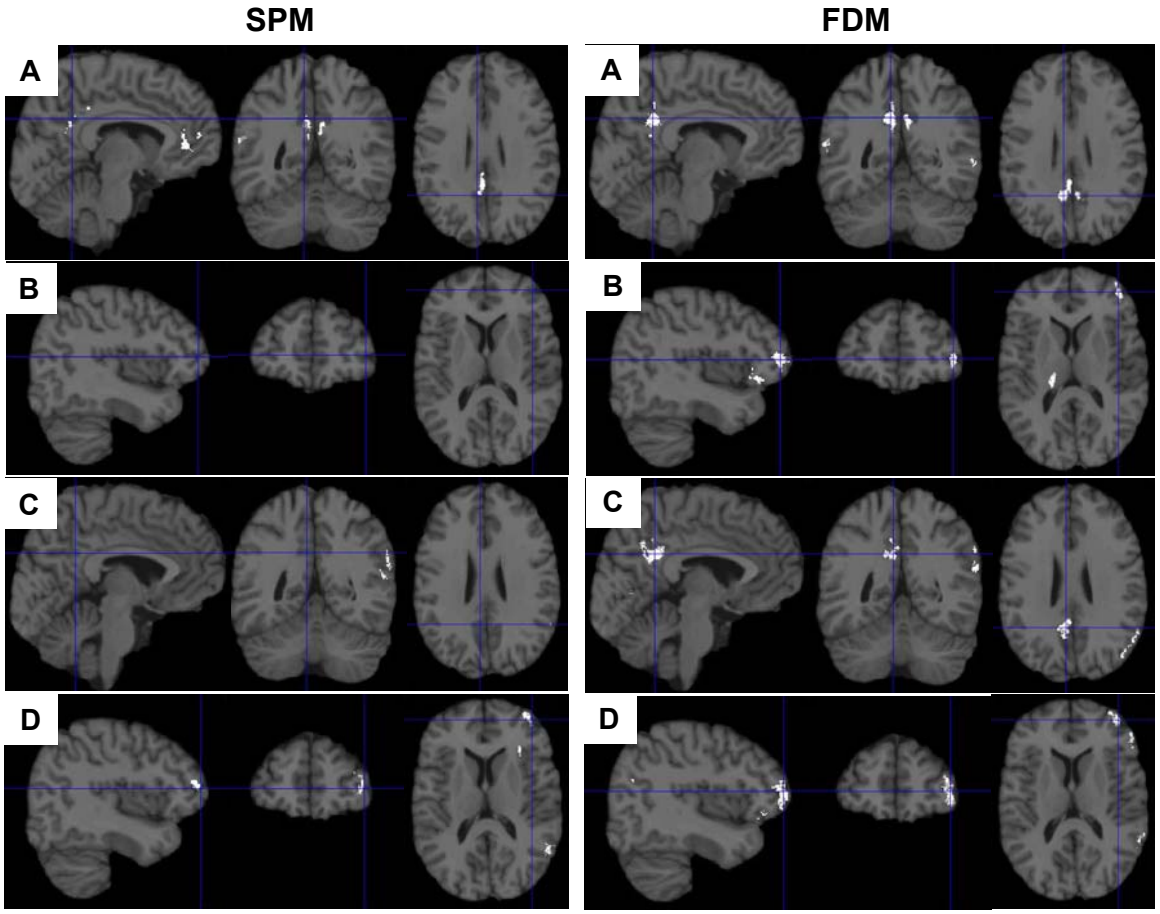

Figure 6.5. Comparison of statistically significant regions (white) between groups from SPM and FDM. A) $CBF_{control} > CBF_{MCI}$; B) $CBF_{MCI} > CBF_{AD}$; C) $CBF_{control} >$ CBFAD.

Table 6.3. Comparison of Cluster-level statistics between groups from FDM and SPM.

	Cluster Location	Cluster size (mm^3) &	Cluster size (mm^3)

		corrected P-value from SPM		& corrected P-value from FDM	
$CBF_{control}$ > CBF_{MCI}	R posterior cingulate ext inf parietal	1383*	0.0001	1024	0.0003
	L posterior cingulate ext inf parietal			431	0.0060
	R superior parietal	233	0.0179	236	0.0180
CBF_{MCI} > CBF_{AD}	L orbital	0 0	N/A N/A	340 249	0.0096 0.0170
	L superior parietal	0	N/A	254	0.0164
	R thalamus	0	N/A	258	0.0171
$CBF_{control}$ > CBF_{AD}	R posterior cingulate ext inf parietal	0	N/A	1155	0.0002
	L orbital	551 0	0.0042 N/A	793 669	0.0011 0.0028
	L superior parietal	395	0.0116	703	0.0019
* L posterior cingulate and R posterior cingulate became one cluster.					

7.0 REGIONAL PERFUSION CHANGES IN MCI AND AD

7.1 INTRODUCTION

The majority of brain functional studies have been conducted in referral clinics[26, 27], with subjects that have advanced disease, especially MCIs. We know very little about CBF changes in MCI and early dementia in subjects from population cohorts. Neuroimaging studies in these subjects, especially those in early disease stages, are extremely important since the severity of symptoms may not have reached the threshold that initiates a referral to specialists. Therefore, neuroimaging of population cohorts provides an ideal opportunity to examine the incipient pathophysiological changes in AD, several years before they are enrolled in memory clinic imaging studies.

The purpose of this chapter is to examine the CBF in subjects with incident dementia and MCI identified through a longitudinal epidemiological study: The Cardiovascular Health Study (CHS) Cognition Study.

7.2 SUBJECTS

The diagnoses of MCI and dementia were done by an Adjudication Committee that examined the longitudinal data, and neuropsychological, neurological, psychiatric, and systemic information.

The CHS Cognition study classified 145 subjects as demented, 141 as MCI, and 246 as normal in 2002-03. However, a total of 188 subjects had an MRI of the brain. For the purpose of this study, we selected those subjects who had no MRI-identified vascular lesions in the brain, had an optimal CASL MRI, and had the diagnosis of either probable AD [141], probable MCI [121], or normal control.

Additional exclusion criteria included: radiological evidence of structural CNS lesions (e.g., brain infarcts, CNS neoplasms, prior brain surgery), history of strokes or head trauma encephalopathy, consumption of caffeine within 8 hours prior to exam, inability to complete MRI exams, inability to segment images using semi-automated tools, placement of the labeling plane was not orthogonal to both carotid arteries and/or the difference between left and right carotid arterial mean velocities exceeded 20%, incorrect operation of the scan (by the technologists), excessive patient motion as evidenced in structural images, excessive image artifact (e.g., hair oil or dental implant), lost or corrupted data files, poor scanner performance (e.g. instability or noise).

After applying the exclusion criteria, 38 Normals, 29 MCIs and 37 ADs were used for statistical analysis.

7.3 METHODS

Spatial registration: An EPI mean image for each subject was registered to the corresponding SPGR volume using SPM2. Then the warping parameters were used to transform the gray matter rCBF maps for the subjects to the SPGR space. SPGR volumes from different subjects were aligned to a standard colin27 brain by a fully deformable atrophy-corrected registration

method (see chapter 6 for details). The SPGR volumes were used to determine the parameters for transforming the CBF maps to the standard space.

7.3.1 Methodological enhancement of statistical analysis

The SPM data processing package is popular for making statistical inferences in group comparisons about regional effects in neuroimaging data, and performing the spatial registration as mentioned in the chapter 6. SPM combines the general linear model (GLM) and the theory of gaussian random field (GRF) to make statistical inferences [147]. The GLM is used to infer the activity at the voxel-level to the group comparisons. To guard against false positives, a correction for multiple comparisons (i.e., comparisons over the voxels) must be made. This is achieved using GRF theory.

A hierarchy of tests are framed in terms of the level of inference (voxel-level, cluster-level and set-level) [146]. These inferences have increasing power but decreasing spatial localization. The cluster-level test is based on the probability of obtaining a cluster with k or more voxels, above a threshold u (i.e. the probability that one cluster, with k voxels or greater size, could happen by chance). The probability takes into account both the significance threshold and the spatial extent of the cluster. The set-level inferences are to assess the significance of distributed (rather than local) activations.

However, all levels of inference of the SPM package require that all subjects have valid data for the voxels which are used to make statistical inferences. In fact, it is almost impossible to get exactly the same slice coverage from the MRI unless the entire brain is acquired. Even if the various heads are correctly positioned in the scanner parallel to B_0 direction and the first slice starts from the same anatomical structure with same slice thickness and interslice spacing, the

image data will not end at the equivalent anatomical structure due to the variance of the brain longitudinal lengths (Fig. 7.1). The heads of the research subjects may not be practically placed in the same fixed position. The common brain area is shown from two subjects in Fig. 7.2 if the head is tilted in the scanner. The common brain coverage area tends to be small from a large group of subjects since a large group of subjects will have cases in both Fig. 7.1 and Fig. 7.2.

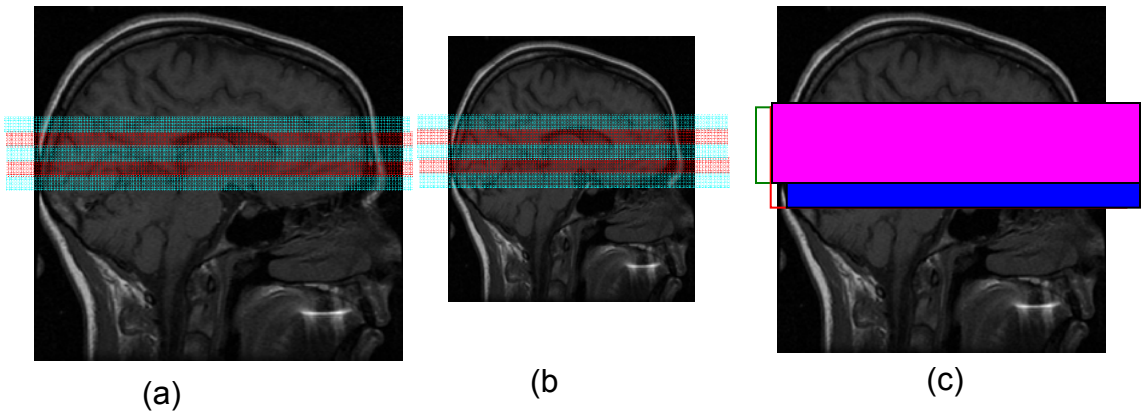

Figure 7.1. Illustration of brain coverage of two subjects who had their head parallel to B0 direction and were scanned at the same anatomical structure (Corpus Callosum) but do not end at the same anatomical structure despite the same slice thickness (5 mm) and interslice spacing (0 mm). After spatial registration, the brain coverage of normalized subject 1 is described by the green box, while the brain coverage of normalized subject 2 is described by the red box. Therefore, normalized subject 1 does not yield the valid data in the blue area. The common brain coverage area of the two subjects is the pink area. The example is exaggerated for illustrative purposes.

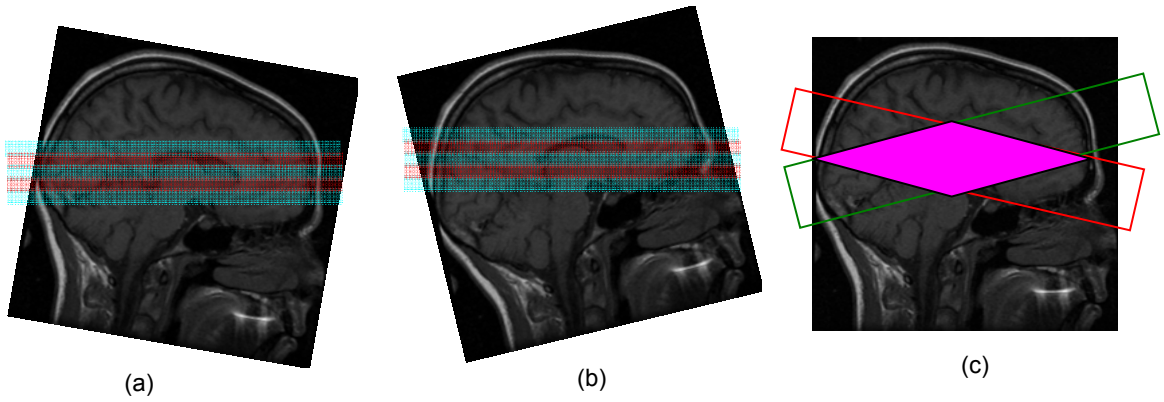

Figure 7.2. Illustration of brain coverage of two subjects who tilted their head and were scanned at the same anatomical structure (Corpus Callosum) but do not end at the same anatomical

structure despite the same slice thickness (5 mm) and interslice spacing (0 mm). Their common brain coverage area is the pink area.

However, the SPM data processing package is only valid for the tiny common brain coverage areas for all of the subjects. Therefore, the data processing will not analyze large cortical regions. One can choose to exclude some subjects whose brain data have less overlap with others. However, researchers normally suffer with small samples. Based on these considerations, we implemented the voxel-level statistical and cluster-level analysis in separate codes to optimally utilize the available data.

The volume of the brain evaluated in this study is all of the gray matter voxels that have valid perfusion data in a majority of subjects (majority criteria: at least 19 subjects for normal controls, 15 for MCI subjects, and 19 for early AD subjects). We refer to this volume as a brain volume mask. The rCBF maps were smoothed using a 6 mm gaussian kernel.

7.3.1.1 Voxel-level group analysis

The smoothed rCBF maps were tested for significant differences between: a) normal controls and early AD subjects, b) MCI and early AD subjects, and c) normal controls and MCI subjects using a customized one-way ANOVA multiple comparison algorithm on a voxel-by-voxel basis written in MATLAB (MathWorks Inc.). The customized algorithm permitted an ANOVA of those voxels with rCBF values that were morphometrically shared by a majority of subjects in each to maximize the brain volume coverage. Because of the variability of slice coverage, the algorithm made the voxels from most of the cortex analyzable in ANOVA. A two-tailed p-value of 0.02 was chosen for the voxel-by-voxel analysis to identify significant differences between groups. The significant difference maps were further masked using the brain volume mask to

avoid a smoothing artifact. SPM subroutines were modified to overlay the masked significant difference maps to the surface section of colin27 brain.

7.3.1.2 Cluster-level group analysis

Cluster searching: The t-statistics maps between group comparisons were thresholded by a t-value corresponding to a two-tailed p-value of 0.02, so that the t-values with a corresponding p-value of less than 0.02 were changed to zero. From each thresholded t-statistics map, we first detected a nonzero voxel *s* as the starting point of a cluster in a scanning order (i.e. every coordinate is from 1 to its maximum value). Then the 3-dimensional map can be considered as a graph *G = (V, E)*, where *V* is a set of vertices and *E* is a set of edges. Here the vertices are all nonzero voxels, the edges connected with a vertex are hidden between the vertex and its all nonzero neighbors (totally 26 neighbors for each vertex), and the voxel *s* is the source. The cluster-searching problem involves finding a connected graph from the source *s*, which can be performed using a classical breath-first-search or depth-first-search algorithm (we chose the breath-first-search algorithm). After cluster-searching, we searched for the next starting point (source) for the next cluster until we completed all of the voxels.

Algorithmically, we can represent the thresholded t-statistics map as a three-dimension matrix *A*. *I, J* and *K* are the three-dimensional maximum indices, respectively. The source vertex can be obtained by scanning matrix *A* from 1 to *I*, from 1 to *J* and from 1 to *K* and searching for the first nonzero vertex that is not in any cluster. A Breadth-first-search algorithm [148] from the source vertex was then utilized to find a cluster by taking nonzero voxels as vertices and all nonzero neighbors of each vertex as its adjacency list.

Algorithm for cluster.

```
for i = 1 to I
   for j = 1 to J
         for k= 1 to K
            do if  A(i ,j ,k) is not in a cluster
                  then A(i, j, k) is a source vertex s for a cluster.
                     Breadth-first-search from source vertex s.
         end
     end
end
```

The probability of a cluster: The probability that a cluster happens by chance (corrected cluster-level P value) was obtained by calling a SPM subroutine which takes a point list of voxels for the cluster, significance threshold, smoothness of image and degree of freedom as parameters. The corrected cluster-level statistics yields a correction for multiple comparisons to guard against false positives.

7.3.2 Volume-Of–Interest (VOI) analysis

We further concentrated our VOIs on the statistically significant clusters (with cluster-level threshold P = 0.02). The average rCBF for each VOI was obtained from the smoothed rCBF maps, which were masked with the corresponding gray matter masks in the standard colin27 space. Only those voxels with valid gray matter rCBF values were used in the quantification of rCBF for each VOI. Subjects with less than 100 voxels in the VOI were excluded from the further two statistical analyses. The analysis was carried out using MATLAB.

ANCOVA Analysis: we further compared the group differences among the control group, the MCI group, and the AD group, by controlling for age, hypertension and gender risk factors using the one-way analysis of covariance (ANCOVA) model. The purpose of the

ANCOVA is to exclude the possibility that group differences that result from imbalance between the ages, hypertensions, and genders,

Multivariate linear regression: a multivariate linear regression between the perfusion and 3MSE score, age, hypertension, gender was calculated from each cluster. The *F* test was used to test for whether those variables (3MSE score, age, hypertension, gender) are significant predictors of the cluster perfusion. If the *F* test showed the significance of the linear model, the t-test for the regression coefficient of 3MSE different than zero was calculated to assess the independent contribution of 3MSE after controlling the other variables.

7.4 RESULTS

The demographic characteristics of the subjects are shown in Table 7.1. There were no statistically significant differences among groups in terms of age, gender, education level, and HRS scores. The proportion of subjects carrying the APOE-4 allele was similar in the three groups. AD subjects had lower 3MSE scores than MCI and normals. There were no statistically significant global gray matter rCBF differences between groups**.** However, we observed the statistically significant clusters from the cluster-level analyses. Cluster-level statistics for the clusters (thresholded at a corrected cluster level of $P < 0.02$) are shown in Table 7.2. The clusters were displayed on the three orthogonal surface of the colin27 brain, but the crosshairs were pointed at the clusters with corrected cluster level of $P < 0.01$ (Figure 7.3).

MCI Group versus Control Group

The comparison of the MCI group vs. the control group demonstrated significant clusters of hypoperfusion in the right inferior parietal lobe extending to the posterior cingulate gyrus

bilaterally (*P* = 0.0079; cluster size = 425) (Figure 7.3A), and significant clusters of hyperperfusion in the left hippocampus (P = 0.0002; cluster size = 1266) (Figure 7.3B), right hippocampus area (P = 0.0078; cluster size = 393) (Figure 7.3C), right caudate and putamen (P = 0.0179; cluster size = 354), and left subcallosal lesion (P = 0.0186; cluster size = 256).

MCI Group versus early AD Group

The early AD group had significant clusters of hypoperfusion in the left inferior parietal lobe (P = 0.0028; cluster size = 582) (Figure 7.3D), left inferior frontal lobe(P < 0.0001; cluster size = 2166) and left superior temporal lobe (P = 0.0028; cluster size = 536) (Figure 7.3E), left caudate (P = 0.0018; cluster size = 683) (Figure 7.3F), left orbital frontal lobe (P < 0.0001; cluster size = 1870) (Figure 7.3G), left thalamus (P = 0.0019; cluster size = 657) (Figure 7.3H), left hippocampus (Figure 7.3I), left superior frontal lobe (P = 0.0124; cluster size = 364), left superior parietal lobe (P = 0.0135; cluster size = 307), right superior temporal lobe (P = 0.0102; cluster size = 277), and left occipital lobe (P = 0.0102; cluster size = 336) compared to the MCI group. There were no significant clusters of hyperperfusion observed for the AD group compared with the MCI group.

Early AD Group versus Control Group

The early AD groups had significant clusters of hypoperfusion in the right inferior parietal lobe extending to the posterior cingulate gyrus bilaterally (P < 0.0001; cluster size = 2101) (Figure 7.3J), left superior parietal (P = 0.0001; cluster size = 1451) (Figure 7.3K), left orbital frontal lobe (P < 0.0001; cluster size = 2384) (Figure 7.3L) and left inferior frontal lobe (P = 0.0076; cluster size = 383) (Figure 7.3M), and a significant cluster of hyperperfusion in the right anterior cingulate gyrus (P = 0.0076; cluster size = 336) (Figure 7.3N).

ANCOVA Analysis

The ANCOVA analysis was used to test for group differences after controlling for the potential confounding factors (age, hypertension, gender). Three VOIs (right amygdala, left caudate nucleus, and left thalamus) lost the significance (with two-tailed p-value threshold 0.02) after controlling for those risk factors, indicating that these regions are affected by the risk factors. The mean perfusion values (after accounting for the confounding factors) of the VOIs with significant group differences compared to the normal controls are shown in Table 7.3. The VOIs of hyperperfusion (left hippocampus, left subcallosum, right caudate & putamen, and right anterior cingulate) remained significantly higher compared to the normal controls even after controlling for the risk factors. In order to describe the changing pattern of MCI and AD patients for the VOIs with respect to normal controls more clearly, we show the rCBF Z-scores of MCI and AD subjects relative to adjusted normal controls in Figure 7.4.

Multivariant linear regression

The multivariant linear regression was performed to test for the correlation of perfusion for each brain VOI with 3MSE score. The perfusion values in the left inferior frontal lobe, left orbital frontal lobe, left superior frontal lobe, left superior parietal lobe, left superior temporal lobe, left & right posterior cingulate gyrus, right anterior cingulate gyrus were significantly correlated with 3MSE (Table 7.5).

7.5 DISCUSSION

We made a specific effort to exclude subjects with disease processes other than AD that may have affected cognition, which allowed us to examine the transition from normal to AD, and early phases of dementia in relative isolation. The perfusion MRI analysis showed patterns of

both hypoperfusion and hyperperfusion of the MCI and early AD group. Specifically for hypoperfusion, the MCI group had decreased CBF in the right inferior parietal lobe and posterior cingulate gyri compared to normal controls. The early AD group had decreased CBF in the parietal association cortices, posterior cingulate gyri, and frontal association cortices compared to the normal controls. The AD group had decreased CBF in the hippocampus, thalamus, caudate, tempoparietal cortices, frontal cortices, and occipital cortices compared to the MCI group. The hypoperfusion brain regions involved were similar to those reported in FDG PET or HMO SPECT. For hyperperfusion, the MCI group had increased CBF in the left hippocampus, left subcallosal lesion, right amygdala, and right caudate & putamen. The early AD group had increased CBF in the right anterior cingulate gyrus. The regional findings implied that a hemodynamic process at the capillary level accompanied the neurodegenerative process, as indicated by the areas of reduced rCBF.

There was hypoperfusion of the right inferior parietal lobe and posterior cingulate gyri in the MCI group compared to the normal control group. The regions were the regions that affected in the AD group. However, the AD group did not have significant hypoperfusion in the right inferior parietal region relative to the MCI group. The lack of regional coherence in the AD versus the MCI group suggested that the posterior cingulate gyrus and right parietal lobe that affected by MCI group was prior to the onset of clinical AD. This result is consistent with that of a previous pulsed arterial spin labeling MR study [27]. Researchers have shown that the posterior cingulate gyrus is one of the earliest structures to be affected in AD [15, 16, 18-20]. The posterior cingulated gyrus can be abnormal in MCI cases, and some studies have found that the posterior cingulate gyrus is a strong predictor of conversion from MCI to AD [15, 16, 18, 20].

The decreased CBF with AD subjects in the parietal association cortices, posterior cingulate gyri, and frontal association cortices is consistent with PET and SPECT studies [149-151]. This finding is also consistent with the progressive pattern observed in the cingulate gyri and temporoparietal cortices with milder AD and frontal cortices involved with more advanced AD [13, 152]. These results are also consistent with previous pulsed arterial spin-labeling MR study involving subjects with AD, but we observed more hypoperfusion regions due to our increased brain coverage.

An ANCOVA analysis was performed to determine whether the hyperperfusion exists after controlling for the risk factors (age, hypertension, sex). We found that the regions of hyperperfusion remain significant, suggesting that the regional hyperperfusion we observed is independent of those risk factors. The hyperperfusion findings demonstate hyperemia in the left hippocampus, right amygdala, right anterior cingulate gyrus, left subcallosm and right caudate & putamen, indicating the presence of a compensatory mechanism. The results of the correlation analysis showed that some regions are significantly correlated with 3MSE. It is worth noting that the right anterior cingulate gyrus appears negatively correlated with rCBF, suggesting the existence of an active compensatory mechanism.

Neurons, microglia, and blood vessels are an integrated unit, and any alteration of this system can lead to brain dysfunction [153-155]. The fact that our cognitively impaired subjects had both increased and decreased rCBF in different regions relative to controls indicate that the vascular process associated with AD is dynamic and complex. Although functional neuroimaging studies have shown decreased rCBF and glucose metabolism in AD subjects, it is difficult to determine which occurs first, the vascular phenomenon or the neurodegenerative process.

The increased cortical CBF in MCI and early AD is consistent with pathological studies that show the presence of compensatory mechanisms in the brains of dementia cases. Choline acetyltransferase and acetylcholinesterase activity were reported to be increased (in the hippocampus and frontal lobes) [156] or normal [157] in MCI and early AD. Cerebral acetylcholinesterase activity is diminished in AD cases, but its severity did not correlate with abnormal glucose metabolism [158].

The increased rCBF extended to the subcallosal region, which is rich in cholinergic neurons [159] and is affected in AD [160]. The cingulate gyrus thus appears to be a pivotal structure where pathology and compensatory mechanisms are inter-related. It has connections with all heteromodal association areas and is involved in memory processes and in the modulation of behavior, emotions, and autonomic responses [161-163].

Although the hippocampus is one of the areas most affected by AD neurofibrillary pathology [164, 165], we found that that CBF was increased in MCI compared to early AD, suggesting that the compensatory mechanisms in the hippocampus were more pronounced in the MCI stage than in early AD. This is consistent with previous reports of increased choline acetyltransferase and acetylcholinesterase activity [156] in MCI and early AD. In addition, functional neuroimaging studies (PET and SPECT) have found that hippocampal glucose metabolism can be preserved in early AD [32, 166, 167]. However, our results may be difficult to compare with these studies, since coupling of glucose metabolism and blood flow has not been confirmed in MCI and early AD.

Taken together, our data suggest an early dysfunction in the Papez circuit (i.e., mesial temporal lobe, thalamus, anterior and posterior cingulate gyrus) [168] in early AD and MCI. AD pathology is present in the thalamus [169], and PET studies have found an association between

episodic memory and activation of the hippocampus, thalamus, and cingulate gyrus of AD subjects [170, 171]. More recently, longitudinal MRI studies have shown that the mesial temporal lobe, thalamus, orbitofrontal cortex, and inferior parietal cortex lost more volume over time in a selected group of MCI subjects [172]. This is important because the inter-related set of structures is critically involved in memory and emotional regulation.

The presence of both increases and decreases in CBF indicates a dynamic process between vascular (and likely cellular) compensatory mechanisms and AD pathology that appears to be more pronounced in the MCI state, i.e., prior to some threshold of neuropathology beyond which such compensation is not possible. The understanding of these compensatory processes is essential for the development of both primary and secondary prevention treatments.

Table 7.1. Demographic characteristics

	Control	**Early AD**	**MCI**	**X^2/F-ratio**
Number of subjects	38	37	29	
Age	82.78 ± 3.54	83.68 ± 3.50	82.73 ± 3.95	1.06
Education level (>high school)	15 (75%)	13 (59%)	8 (53%)	1.94
Male/Female	13/25	13/18	12/11	1.93
Caucasians	17 (85%)	16 (73%)	14 (100%)	2.78
3MSE	95.24 ± 4.48	85.16 ± 9.46	91.10 ± 8.59	9.78*
HRS	1.1 ± .9	1.0 ± 1.7	.9 ± 1.2	.10
APOE-4 allele	4 (21%)	8 (40%)	4 (27%)	1.63

*****ANOVA: Control and MCI different from AD ($p < 0.001$)
Abbreviations: AD: Alzheimer's disease; MCI: Mild Cognitive Impairment; 3MSE: Modified Mini-Mental State Examination; HRS: Hachinski Rating Scale.

Table 7.2. Summary of cluster-level statistics for decreased and increased CBF in Control, MCI and Early AD subjects

Group Analysis	Cluster location	Cluster-level corrected p-value	Cluster size
Control > MCI	L/R posterior cingulate, right inferior parietal	0.0079	425
MCI > Control	L hippocampus R hippocampus area R caudate & putamen	0.0002 0.0078 0.0179	1266 393 354

	L subcallosm	0.0186	256
MCI > AD	L hippocampus	< 0.0001	3211
	L inferior frontal	< 0.0001	2166
	L orbital frontal	< 0.0001	1870
	L caudate	0.0018	683
	L thalamus	0.0019	657
	L inferior parietal	0.0028	582
	L superior temporal	0.0028	536
	R superior temporal	0.0102	277
	L occipital	0.0102	336
	L superior frontal	0.0124	364
	L superior parietal	0.0135	307
AD > MCI	NO		
Control > AD	L orbital frontal	< 0.0001	2384
	L/R posterior cingulate, inferior parietal	< 0.0001	2101
	L superior parietal	0.0001	1451
	L inferior parietal	0.0076	383
AD > Control	R anterior cingulate	0.0076	336

Table 7.3. The mean CBF values of Control, MCI, and Early AD subjects after controlling the age, hypertension and gender effects. Black font stands for the significant change of CBF compared to normal controls.

REGION	Control perfusion	MCI perfusion	AD perfusion
L & R posterior cingulate	53.4231	**40.6653**	**40.9568**
R caudate & putamen	37.0577	**47.6090**	42.3857
L subcallosm	35.3047	**51.5062**	35.9145
L hippocampus	37.4982	**53.6585**	37.3389
R hippocampus	36.6203	**48.8715**	40.1613
L inferior parietal lobe	56.6975	58.1019	**43.1191**
R anterior cingulate	40.8668	48.0527	**57.8757**
L superior parietal lobe	44.4516	40.9650	**31.3015**
L inferior frontal lobe	44.6551	41.2890	**32.1100**
L orbital frontal lobe	51.8297	50.5894	**36.3601**

Blood flow values are expressed as milliliters per 100g tissue per minute [ml/(100g·min)].

Table 7.4. Significant correlations between cluster perfusion and 3MSE.

REGION	3MSE coefficient	Two-tailed p value
L inferior frontal lobe	0.4801	0.0047
L orbital frontal lobe	0.4227	0.0027
L superior frontal lobe	0.3899	0.0098
L superior parietal lobe	0.4571	0.0057
L superior temporal lobe	0.4719	0.0061
L & R posterior cingulate gyrus	0.5525	0.0030

R anterior cingulate gyrus	-0.6943	0.0056

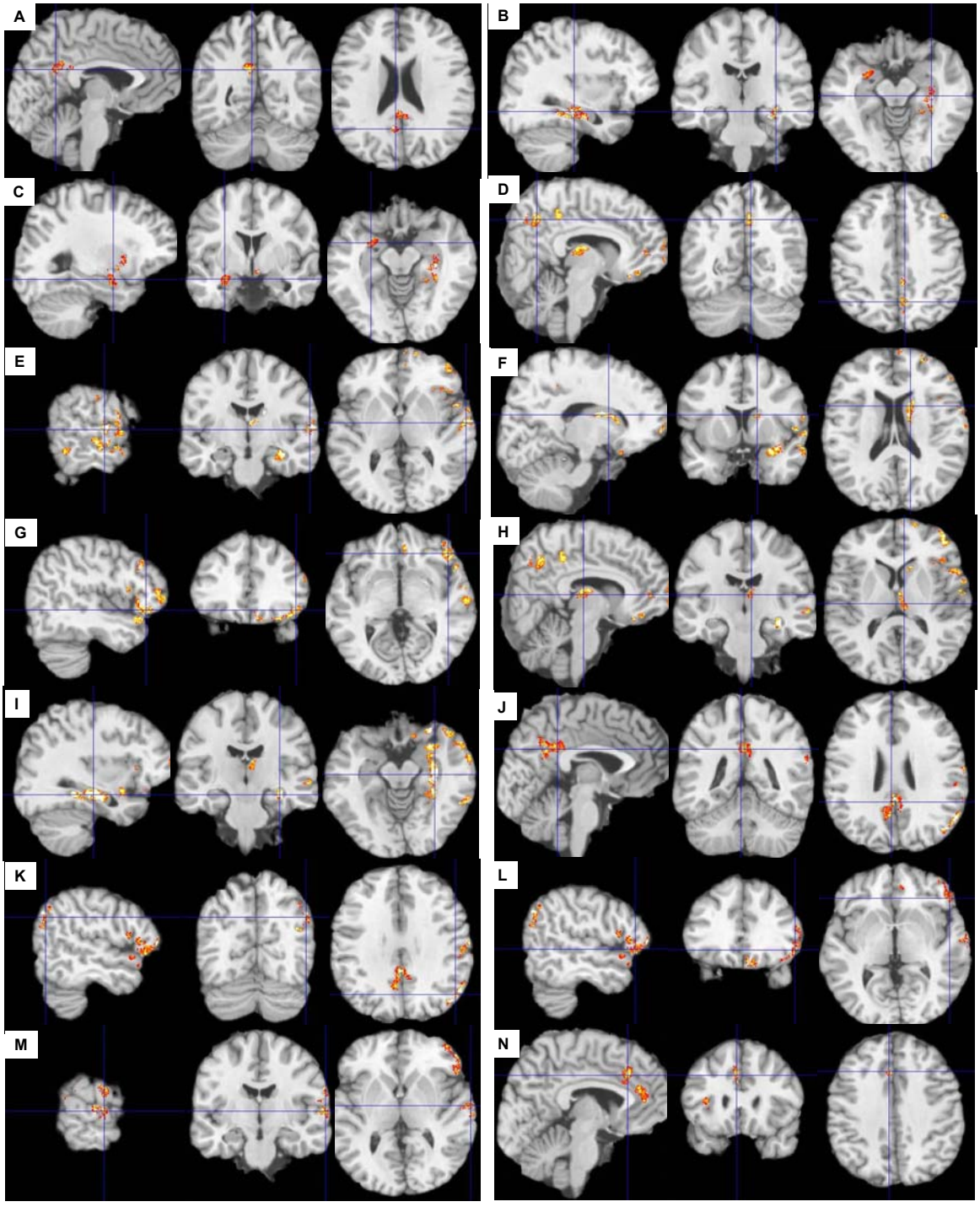

Figure 7.3. Statistically significant changes in regional CBF by ANOVA ($p < 0.02$) are overlaid in color on the top of a surface section of the colin27 brain. A) CBFControl > CBFMCI at L & R post cingulate, B) $CBF_{MCI} > CBF_{Control}$ at L hippocampus, C) $CBF_{MCI} > CBF_{Control}$ at R hippocampus area, D) $CBF_{MCI} > CBF_{AD}$ at L inf parietal, E) $CBF_{MCI} > CBF_{AD}$ at

L inf frontal & L sup temporal, F) $CBF_{MCI} > CBF_{AD}$ at L caudate, G) $CBF_{MCI} > CBF_{AD}$ at L orbital frontal, H) $CBF_{MCI} > CBF_{AD}$ at L thalamus, I) $CBF_{MCI} > CBF_{AD}$ at L hippocampus, J) $CBF_{Control} > CBF_{AD}$ at L/R post cingulate, K) $CBF_{Control} > CBF_{AD}$ at sup parietal, L) $CBF_{Control} > CBF_{AD}$ at L orbital frontal, M) $CBF_{Control} > CBF_{AD}$ at inf frontal N) $CBF_{AD} > CBF_{Control}$ at R anterior cingulate. The color scale ranges from yellow (highest positive t-score) to red (lowest positive t-score).

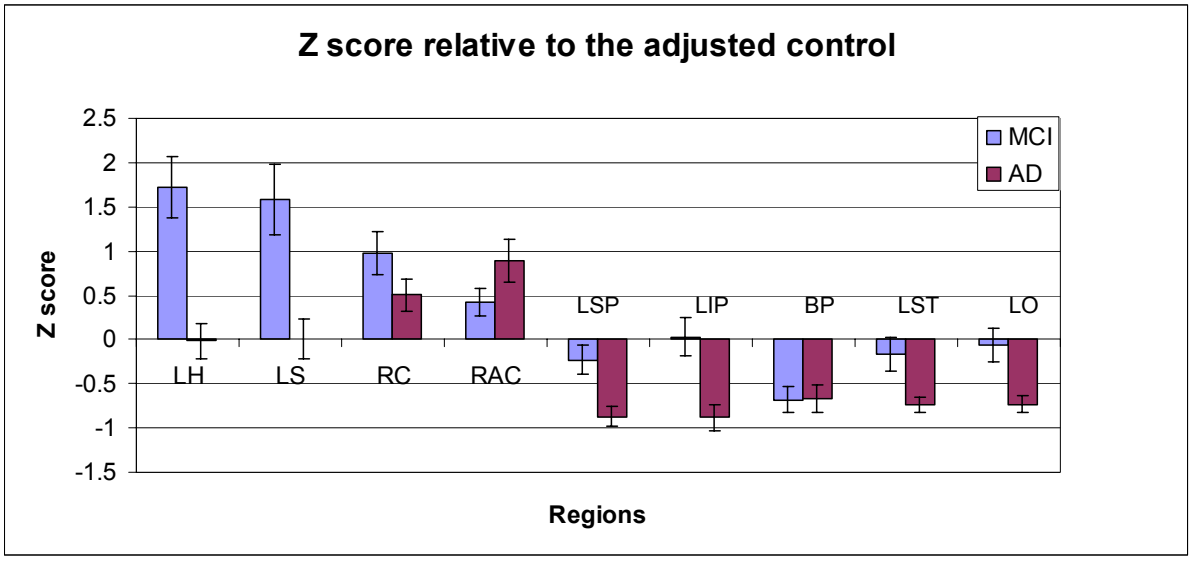

Figure 7.4. Comparison of standard Z-score of CBFs of MCI and AD subjects compared with normal controls after adjusting the risk factors for the VOIs identified from cluster-based analysis. Error Bars represent standard error from the mean (SEM). (LH = left hippocampus; LS = left subcallosal area; RC = right caudate and putamen; RAC = right anterior cingulate; LSP = left superior parietal; LIP = left inferior parietal; BP = Bilateral posterior cingulate; LST = left superior temporal; LO = left orbital frontal).

8.0 RISK FACTOR OF HYPERTENSION TO AD

8.1 INTRODUCTION

Hypertension (HTN) is frequent in elderly subjects; 30-40% prevalence in subjects age 65 or higher [173-176]. HTN has a significant impact on cardiovascular functions [177], and in cerebral structures, with the subsequent cognitive deterioration [178-181]. The most common explanation for the effect of HTN on cognition is that it increases the risk of cerebrovascular disease (CVD) [182, 183]. Long-term HTN can cause vascular hypertrophy and microvascular remodeling by promoting arteriosclerosis in large vessels and lypohyalinosis in penetrating arterioles, with subsequent regional cerebral blood flow (rCBF) dysfunction [184-186], which could lead to strokes and white matter disease. HTN was found to be a risk factor for cognitive decline [178-181], and for Alzheimer's disease (AD) [179, 187]. HTN causes a CNS vulnerability state that leads to cognitive deficits mainly through CVD. However, HTN also appears to be a risk factor for AD. Therefore, it is crucial to understand the pathophysiology of HTN in cognitively normal controls, MCI and AD subjects.

Studies conducted in middle-aged cognitively normal subjects with HTN showed a pattern of reduced rCBF and compensation using positron emission tomography (PET) [188]. When engaged in memory tasks, hypertensive subjects had less activation than normotensives in the middle posterior watershed area, parietal lobes, and thalamus. Interestingly, hypertensive

subjects with normal performance in memory tasks had increased CBF in the amygdala/hippocampus area. Functional MRI studies have shown that there was a correlation between activation in the anterior cingulate gyrus, insula, thalamus, and periacueductal grey matter and measures of blood pressure when cognitively normal hypertense subjects performed the Stroop test [189].

Volumetric MRI studies have shown that elevated systolic pressures in untreated hypertensive and cognitively normal subjects (mean age 61.3 years) correlated with decreased gray matter volumes in superior frontal, anterior cingulate, and middle temporal gyri [190]. In addition, the gray matter volume was associated with memory and executive function tests, and non-treated midlife blood pressure was associated with decreased hippocampal volume 30 years later [191]. These studies suggested that HTN can alter brain structure and rCBF beyond the expected cerebral regions localized at the end of the tree of the perforant arteries. These limbic and paralimbic areas are critical for higher cognitive functions, and are targeted by AD pathology. Therefore, the purpose of this study is to investigate the rCBF in cognitively normal subjects, identified through a population-based study, using continuous arterial spin-labeled MRI (CASL-MRI). We hypothesize that the rCBF of hypertensive subjects will be altered at the capillary level in multiple brain regions, reflecting a vulnerability state caused by HTN.

8.2 MATERIAL AND METHODS

8.2.1 CHS Cognition study

The Pittsburgh Cardiovascular Health Study Cognition Study (CHS-CS) is a continuation of the CHS Dementia Study, and it was conducted in 2002/03 to determine the incidence of dementia and mild cognitively impaired (MCI) in a population of normal and MCI subjects identified in 1998/99 in the CHS-CS in Pittsburgh. Of the 927 participants examined in 1998-99, a total of 532 normal and MCI subjects were available for study in 2002/03. All subjects had complete neurological and neuropsychological examinations in 1998-99, and an MRI of the brain in 1992-94, and 449 had a repeat MRI in 1998-99. The characteristics of the total CHS cohort, and the Pittsburgh CHS-CS have been described previously [121, 192], as well as the details concerning the longitudinal follow-up of the CHS participants [121, 122]. All participants completed neurological, neuropsychological examinations in 1998-99, and in 2002-03.

Subjects

The CHS-CS is conducting an MRI of the brain for all subjects who convert from Normal to MCI, Normal to dementia, or MCI to dementia. In addition, we are performing MRI of the brain to a group of 25-30 controls per year. Of the 188 subjects who had an MRI of the brain in 2002-04, we selected 38 controls, 29 MCI and 37 AD subjects for this study. These participants had an optimal CASL MRI with no MRI-identified vascular lesions in the brain. Additional exclusion criteria to maximize case reliability and validity were: radiological evidence of structural CNS lesions (e.g., brain infarcts, CNS neoplasms, prior brain surgery) or history of strokes or head trauma encephalopathy, consumption of caffeine within 8 hours prior to exam, inability to segment images using semi-automated tools, placement of the labeling plane was not

orthogonal to both carotid arteries and/or the difference between left and right carotid arterial mean velocities exceeded 20% of the mean, excessive patient motion as evidenced in structural images, or excessive image artifact (e.g., hair oil or dental implant).

Clinical examination

Neurological exam: The neurological exam included a brief mental status examination, as well as cranial nerve testing, motor tone, abnormal movements, strength, deep tendon reflexes, release signs, plantar response and clonus, cerebellar testing, primary sensory testing, gait, and postural stability. The examiner also completed the Unified Parkinson's Disease Rating Scale (UPDRS) [193] and the Hachinski Ischemic Scale (HRS) [194].

Psychiatric examination: Symptoms of depression were measured with the modified version of the Center for Epidemiology Studies Depression Scale (CES-D) 10-item version [195] and additional behavioral symptoms were measured with the Neuropsychiatric Inventory (NPI).

Neurpsychological exam: All participants were assessed with the following cognitive measures: Premorbid intelligence: the American version of the National Reading test (AMNART) [196], Raven's Colored Progressive Matrices [197], Memory: California Verbal Learning Test (CVLT) [198], Rey-Osterreith figure, Language: Boston Naming test [199], Verbal fluency test, Visuoperceptual/visuoconstructional: Block design (from the Wechsler Adult Intelligence Scale-revised) [200], Copy of a geometric figure, and Executive functions: Stroop test, Digit Spans [200], Baddeley & Papagno Divided Attention Task [201], and the Motor: Grooved Pegboard Test [202]. Total time of the neuropsychological battery was 2 hours.

8.2.2 CASL MRI & Image Processing

The details of MRI data acquisitions protocol and image processing are shown in Section 5.6. Absolute rCBF maps of gray matter were generated for each individual subject.

8.2.3 Statistics

An EPI mean image for each subject was registered to the corresponding SPGR image using SPM2. Then the warping parameters were used to transform the gray matter rCBF maps for the subjects to the SPGR space. SPGR images from different subjects were aligned to a standard colin27 brain by a fully deformable atrophy-corrected registration method [65]. The SPGR images were used to determine the parameters for transforming the CBF maps to the standard space. The volume of the brain evaluated in this study was all the gray matter voxels that have valid perfusion data in a majority of subjects, and we refer to this as a brain volume mask. The rCBF maps were smoothed using a 6 mm gaussian kernel.

The smoothed rCBF maps were tested for significant differences between hypertensive and normo-tensive subgroup within normal controls, MCI subjects, and AD subjects. Due to variability in slice coverage between subjects, some voxels in the standardized space contained rCBF measurements. Therefore, a customized t-test algorithm was written in MATLAB (MathWorks Inc.) to test differences in rCBF between normotensives and hypertensives on a voxel-by-voxel basis. The customized algorithm permitted t-tests of only those voxels in which rCBF was measured in a majority of subjects to maximize the brain volume coverage. By permitting the analysis of voxels in which only a subset of rCBF measurements were available, the algorithm allowed the analysis to include voxels from most of the cortex. A two-tailed p-

value of 0.02 was chosen for the voxel-by-voxel analysis to identify significant differences between groups. The significant difference maps were further masked using a brain volume mask to avoid a smoothing artifact. The masked significant difference maps were displayed on the surface section of colin27 brain by modifying SPM subroutines. Clusters displayed on colin27 brain were thresholded at a correct cluster-level of $P < 0.01$ [146]. The cluster-level correction was performed to guard against false positives from multiple comparisons. The correction took into account the voxel-level threshold, the size and shape of cluster.

8.3 RESULTS

The demographic characteristics of the subjects are shown in Table 8.1. There were no statistically significant differences among groups in terms of age, gender, education level. AD subjects had lower 3MSE scores than MCI and Normal controls. Demographic and clinical characteristics of cognitively normal subjects are shown in Table 8.2. There were more subjects with HTN using convertase II inhibitors and diuretics than those without. There were no statistical differences in terms of age, gender, education level, Modified Mini-Mental State Examination [203] score, heart disease, diabetes mellitus, and other medication intake (beta-blockers, calcium channel blockers, other vasodilators).

CASL MRI

There was no hyperperfusion observed for hypertensive subgroup compared with normo-tensive subgroup within each group (normal controls, MCI subjects, or AD subjects).

Hypertensive normal controls vs. normo-tensive normal controls

The comparisons of hypertensive normal controls versus normo-tensive normal controls demonstrated significant clusters of hypoperfusion in the anterior cingulate gyrus (Fig 8.1A), inferior parietal lobe (Fig 8.1B), inferior frontal lobe and putamen (Fig 8.1C) bilaterally, left superior frontal lobe, left orbital frontal lobe, left hippocampus (Fig 8.1C) and superior parietal (Cluster-level $P > 0.01$, not shown). Cluster-level statistics for all clusters are shown in Table 8.3.

Hypertensive MCIs vs. normo-tensive MCIs

No significant clusters of hypoperfusion were seen in the hypertensive MCIs versus normo-tensive MCIs.

Hypertensive ADs vs. normo-tensive ADs

The comparisons of the hypertensive ADs versus. normo-tensive ADs showed significant clusters in the putamen bilaterally, left inferior frontal lobe together with superior temporal lobe (Fig 8.1D), left hippocampus and left middle temporal lobe (Cluster-level $P > 0.01$, not shown).

8.4 DISCUSSION

We only observed hypoperfusion for the subgroup with hypertension compared with the subgroup without hypertension. We found that compensatory hyperemia (e.g. anterior cingulate gyrus) in MCI and AD subjects along with decreased perfusion in specific brain regions in this cohort. The presence of hypertension appears to moderate the increase in blood flow, suggesting at least one mechanism for vascular risk in dementia. Hypoperfusion was most evident in normal subjects, suggesting that vascular damage occurs well before the onset of dementia symptoms.

These findings showed that rCBF, at the capillary level, is affected in normal elderly subjects with HTN, not only in the subcortical regions, but also in limbic and paralimbic structures, even when they are receiving the proper anti-hypertensive treatment. However, it seems that the effect of HTN is attenuated after the onset of the pathological cognitive process. These findings are consistent with previous observations of the association between HTN and hippocampal and amygdala atrophy [191], and with the notion that HTN can affect cerebral structures that are targeted by AD pathology [188, 189], increasing the vulnerability of hypertensive subjects to develop AD.

Our findings showed diminished rCBF in the frontal (orbitofrontal cortex and cingulate gyrus), temporal, and parietal cortices, and subcortical regions (striatum) in elderly subjects with HTN. These findings suggested that HTN can alter brain structure and rCBF beyond the expected cerebral regions localized at the end of the tree of the perforant arteries in subcortical regions (striatum). This is consistent with previous studies conducted in non-demented patients with HTN that showed that diminished cerebrovascular dilative response to physiological stimuli [188, 189], and a pattern of reduced rCBF and compensation in middle age subjects with HTN using PET. Furthermore, volumetric MRI studies have shown that elevated systolic in untreated hypertensive, and cognitively normal, subjects (mean age 61.3 years) correlated with gray matter volumes in superior frontal, anterior cingulate, and middle temporal gyri [190].

Long-term HTN can cause significant structural vascular damage to large vessels and microcirculation, with subsequent rCBF dysfunction [184-186]. Damage to the vascular endotelium is the earliest and most critical pathophysiological process of the CVD associated with HTN; as shown in subjects with juvenile HTN. However, the complexity and heterogeneity of the effect of HTN on the vascular endothelium is not fully understood, especially the vulnerability of the

microcirculation of specific cortical areas to HTN. Moreover, the relationship between these HTN-related vascular factors and neurodegeneration is unknown. The increased vascular production of superoxide dismutase [204-206], which leads to inactivation of NO-dependent vasodilatation, appear to play a critical role in the HTN vascular damage. These vascular processes can alter the glutamate-mediated [Ca+] neuronal-to-astrocyte control of the microcirculation [207, 208], which may explain the relationship between decreased rCBF in heteromodal association areas in subjects with HTN. Recent findings, in normal subjects, have shown that there is an astrocyte-mediated Ca+ rise in parenchimal arterioles as a response to neuronal activity [208], and that cortical areas with increased synaptic activity, such as the heteromodal association areas, have increased vulnerability to AD pathology [209]. Taken together, these studies indicated that neurons, astrocytes, and microcirculation are closely interrelated, and damage to the vascular endothelium may cause neuronal dysfunction, especially in areas of increased synaptic activity.

Finally, our findings are consistent with the notion that HTN can contribute to cognitive deficits, in the absence of radiological (CT- or MRI-identified) infarcts, or clinical strokes [178, 179]. In addition, they are relevant to the hypothesis that CVD can modulate AD clinical manifestation [210, 211] by expressing the clinical symptoms of dementia with fewer AD pathological changes, and that hypertension plays a critical role in this process [212].

This study is limited by the small number of subjects, and by the lack of information about duration of antihypertensive medication. It was shown that antihypertensive treatments diminished the risk of dementia [213, 214], and they can modify structural brain changes [215]. The relationship between CASL MRI in hypertensive patients and incident dementia needs to be

examined. This will allow us to identify a rCBF pattern that may predict dementia in healthy individuals with HTN.

Table 8.1. Subjects Characteristics with and without hypertension

Class		Hypertensive	Normotensive
Normal	Number of subjects	16	22
	Male/Female	6/10	7/15
	Age	83.5 ± 3.1	82.2 + 3.7
	3MSE	94.4 ± 4.7	95.8 ± 4.2
MCI	Number of subjects	11	18
	Male/Female	81.8 ± 4.6	83.2 ± 3.4
	Age	7/4	5/13
	3MSE	92.5 ± 5.9	90.2 ± 9.9
AD	Number of subjects	18	19
	Male/Female	6/12	7/12
	Age	83.8 ± 3.6	83.5 ± 3.4
	3MSE	83.4 ± 10.1	86.7 ± 8.7

Table 8.2. Demographic and clinical characteristics of cognitively normal subjects with and without hypertension

	Hypertensive	**Normotensive**	**χ^2/ t-test**	**p-value**
Number of Subjects	16	22		
Age	83.5 ± 3.1	82.2 ± 3.7	-1.09	.28
Education level (%) (>high school)	10 (62.5)	16 (73)	.44	.50
Race: Whites (%)	11 (69)	20 (91)	3.02	.08
Male/Female	6/10	7/15	.13	.71
3MSE	94.4 ± 4.7	95.8 ± 4.2	.93	.35
Heart Disease* (%)	1 (6)	4 (18)	1.54	.28

Diabetes Mellitus** (%)	1 (6)	2 (9)	.10	.74
Convertase II inhibitors (%)	8 (50)	0 (0)	13.9	<.001
Beta Blockers	4 (25)	3 (14)	.79	.37
Calcium Channel Blocker (%)	6 (37.5)	6 (27)	.44	.50
Diuretics (%)	10 (62.5)	1 (4.5)	15.2	<.001
Other vasodilators (%)	3 (18)	2 (9)	.75	.38

***** History of angina, or Myocardial infarction, ** by American Diabetes Association.

Table 8.3. Summary of Cluster-level statistics for hypoperfusion clusters

	Region	Cluster p-value	Custer size
Normal	L anterior cingulate	0.0000	4763
	L sup frontal	0.0000	2238
	L inf frontal & L Putamen & L hippo	0.0000	12099
	R inf frontal	0.0002	1207
	R putamen	0.0000	1589
	R anterior cingulate	0.0000	2166
	L sup parietal	0.0125	312
	L inf parietal	0.0000	3092
	R inf parietal	0.0064	467
	L middle temporal	0.0001	1356
	L orbital frontal	0.0031	605
MCI	NO		
AD	L inf frontal & superior temporal	0.0000	2488
	L middle temporal	0.0177	258
	L putamen	0.0028	495
	R putamen	0.0016	642
	R thalamus	0.0180	220
	L hippocampus	0.0261	201

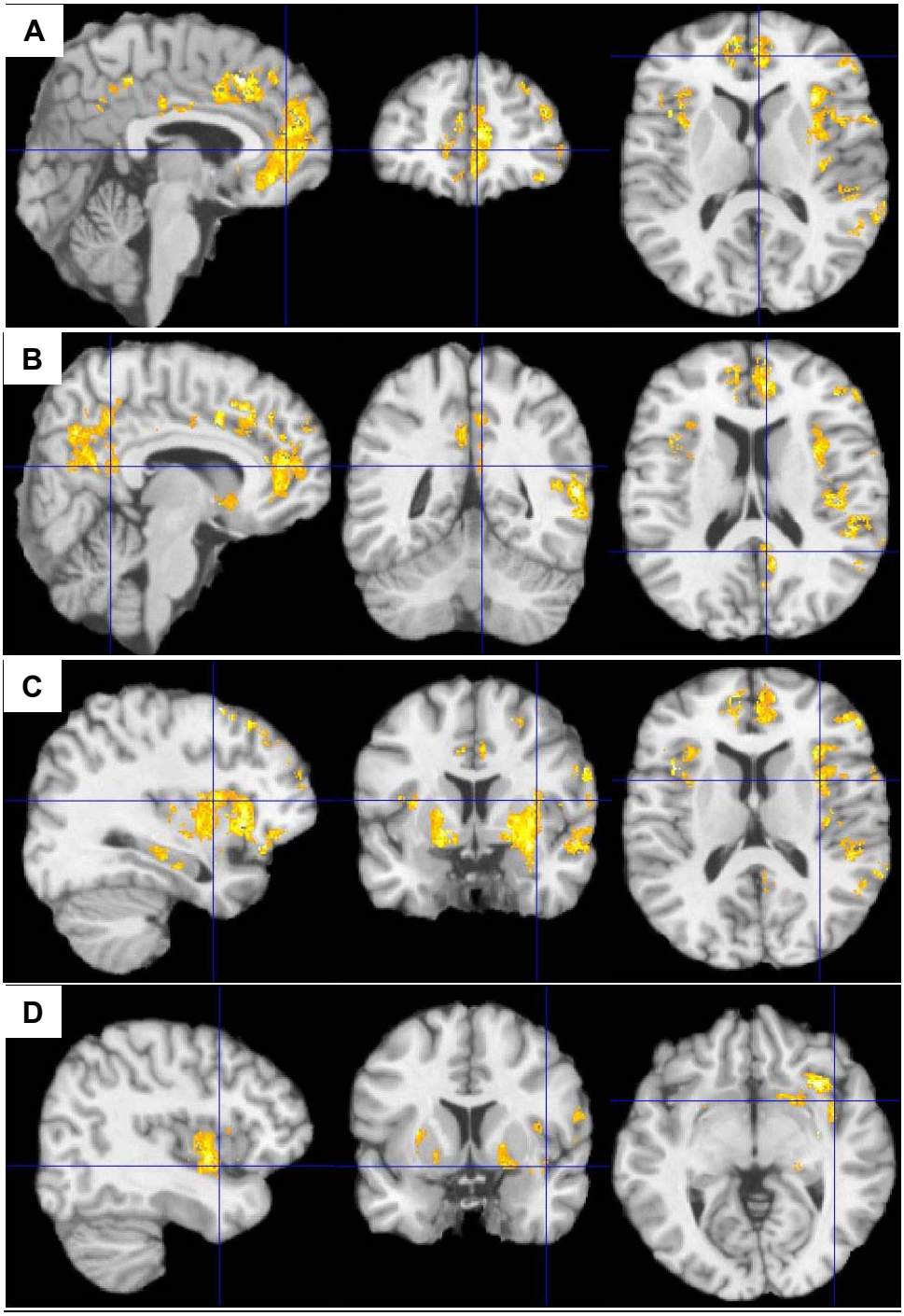

Figure 8.1. Statistically significant regional CBF decreases in hypertensive subjects compared with normo-tensive subjects by t-test (cluster-level $P < 0.01$) are overlaid in color on the top of a surface section of the colin27 brain. A) Anterior cingulate gyrus $CBF_{hyper\_normal} < CBF_{normo\_normal}$; B) Posterior cingulate gyrus $CBF_{hyper\_normal} < CBF_{normo\_normal}$; C) Bilateral putamen, left superior frontal lobe, left orbital frontal lobe, left hippocampus $CBF_{hyper\_normal} < CBF_{normo\_normal}$. D) Bilateral putamen, left inferior frontal lobe and superior temporal lobe $CBF_{hyper\_AD} > CBF_{normo\_AD}$ The color scale ranges from yellow (highest positive t-score) to red (lowest positive t-score).

9.0 SUMMARY AND FUTURE WORK

Individual brain perfusion map was measured by a noninvasive technique: continuous arterial spin labeling (CASL). CASL techniques use off-resonance RF pulses to invert flowing arterial water (1H proton) spins in the carotids of the neck. However, the RF pulses produce significant off-resonance saturation effects (MT effects). A dual-Lorentzian model was established to characterize the MT effects in CASL. The labeling region tends to lie in the inhomogeneous region in the scanner, so the individual inversion efficiency may very significantly between subjects. An analytical model was established to calculate the individual inversion efficiency and also verified by the *in vivo* experiments. Quantification of perfusion map was improved by incorporating short postlabeling delay, MT effects, individual inversion efficiency, individual arrival time and superior-to-inferior acquisition.

Spatial normalization transforms the brain volume from each subject to the same reference volume to correct for anatomical variability. From the quantitative comparison of two normalization algorithms (statistical parametric mapping (SPM2) vs. fully deformable model (FDM)), FDM increased anatomical normalization accuracy and thus improved the biostatistical group comparison of pMRI (perfusion MRI) compared with SPM2. Therefore, FDM was applied to transform the individual brain perfusion map to the reference volume.

A group of population subjects from cognitive healthy study (CHS) were used to evaluate the perfusion changes among normal controls, mild cognitive impairments (MCIs) and early

Alzheimer's disease (ADs). First, voxel-level statistical comparison of perfusion was performed by customized one-way ANOVA. The voxels in which at least half of subjects have valid perfusion data in each group were counted in the ANOVA analyses. Second, cluster-level analysis was performed to correct for false positives in the voxel-level comparison. Third, the statistically significant clusters were targeted to evaluate the group difference by controlling the risk factors. The effects of hypertension on the CBF within each group (normal controls, MCIs, or ADs) were investigated by voxel-level and cluster-level statistics.

We observed not only the decreased cerebral blood flow (CBF), but also the increased CBF. Moreover, the regions with increased CBF remain significant even after the risk factors are controlled. The regional findings imply a compensatory mechanism, at the capillary level, accompanied the neurodegenerative process. For the effects of hypertension, only hypoperfusion was observed for the subgroup with hypertension compared to the subgroup without hypertension. The presence of hypertension appears to moderate the increase in blood flow, suggesting one mechanism for vascular risk in AD. Hypoperfusion was most evident in normal controls suggesting that vascular damage occurs well before the Onset of AD symptoms.

The perfusion techniques, registration techniques, and statistical tools that developed in the thesis can be used to study the longitudinal perfusion changes and predict the potential population with high risk to develop the Alzheimer's disease. These techniques can be applied to study the perfusion changes and risk factors for other brain diseases (such as Lewis body disease, Stroke, Parkinson disease), and detect the drug effects of any potential drugs. These techniques can be adopted to investigate the perfusion of other human organs (such as kidney, liver).

APPENDIX A GLOSSARY

Bloch equations: Equations of motion for the magnetization vector in the presence of magnetic field.

Echo-planar imaging: Ultra-fast imaging technique that fills whole two-dimensional k-space data from a single data acquisition.

Flip angle: Degree of magnetization vector rotated by an RF pulse relative to the direction of the static magnetic field.

Full saturation: A state in which the directions of spins are random, so that the net magnetization is zero.

Gradient echo: Echo signal generated by dephasing and rephasing a transverse magnetization via changing the gradient direction.

On-resonance: A state in which the frequency of an excitation RF field is same as the Larmor frequency of spins.

Off-resonance: A state in which the frequency of an excitation RF field is different from the Larmor frequency of spins.

Pulse sequences: A diagram showing that when and how long RF and/or gradient pulses are applied to a spin system.

Partial saturation: A state in which the net magnetization is nonzero, by applying repeated RF pulses in times on the order of or shorter than T_1.

APPENDIX B ABBREVIATION

AIF	Artery input function
AD	Alzheimer's disease
AFP	Adiabatic fast passage
AIR	Automated image registration
AM	Amplitude modulated
ANCOVA	Analysis of covariance
ANOVA	Analysis of variance
APDI	Alternating proximal and distal irradiation
ASD	Alternating single and double adiabatic inversion
BET	Brain Extraction Tool
BOLD	Blood oxygenation-dependent contrast
CASL	Continuous arterial spin labeling
CBF	Cerebral blood flow
CHS	Cognitive healthy study
CNS	Central nerve system
CW	Continuous Wave
CVD	Cerebrovascular disease
CT	Computed tomography
DAI	Double adiabatic inversion
DCT	Discrete cosine transformation
DSC	Dynamic susceptibility contrast
EPI	Echo-planar imaging
FDA	Food and Drug Administration
FDM	Fully deformable model
fMRI	Functional magnetic resonance imaging
FSL	FMRIB Software Library
GLM	General linear model
GRF	Gaussian random field
HTN	Hypertension
IDL	Interactive Data Language
IRB	Institutional Review Board
MCI	Mild cognitive impairment
MNI	Montreal Neurological Institute
MRI	Magnetic resonance imaging
MT	Magnetization transfer
NMR	Nuclear magnetic resoance

PC	Phase contrast
PET	Positron emission tomography
pMRI	Perfusion magnetic resonance imaging
RF	Radiofrequency
rms	Root-mean-square
rCBF	Regional cerebral blood flow
rBW	Receiver bandwidth
ROI	Region of interest
SAI	Single adiabatic inversion
SAR	Specific absorption rate
SNR	Signal-noise-ratio
SPDI	Simultaneous proximal and distal irradiation
SPET	Single photon emission computed tomography
SPGR	Spoiled gradient-recalled echo
SPM	Statistical parametric mapping
TE	Time of echo
TR	Time of repetition
VBM	Voxel-based morphometry

BIBLIOGRAPHY

1. Ewbank CD. Alzheimer's disease as a cause of death in the U.S.: estimates and projections. The annual meetings of the population association of America, San Francisco, April 1995.

2. Hofman A, Rocca WA, Brayne C, et al. The prevalence of dementia in Europe: a collaborative study of 1980-1990 findings. Euroderm Prevalence Research Group. Int J Epidemiol 1991;20(3):736-748.

3. Evans DA, Funkenstein HH, Alberts MS. Prevalence of Alzheimer's disease in a community population of older persons: Higher than previously reported. JAMA 1989;262(18):2551-2556.

4. Fitzpatrick AL, Kuller LH, Ives D, et al. Incidence and prevalence of dementia in the cardiovascular health study. J Am Geriatr Soc 2004;52(2):195-204.

5. Sloane PD, Zimmerman S, Suchindran C, et al. The public health impact of Alzheimer's disease, 2000-2050: Potential implication of treatment advances. Ann Rev Public Health 2002;23:213-231.

6. Brookmeyer R, Gray S, Kawas C. Projections of Alzheimer's disease in the United States and the public health impact of delaying disease onset. Am J Public Health 1998;88(9):1337-1342.

7. Bren L. Alzheimer's: searching for a cure. FDA Consumer magazine, July-August 2003.

8. Chetelat G, Baron JC. Early diagnosis of Alzheimer's disease:contribution of structural neuroimaging. NeuroImage 2003;18(2):525-541.

9. Flicker C, Ferris SH, Reisberg B. Mild Cognitive impariment in the elderly: predictors of dementia. Neurology 1991;41:1006-1009.

10. Peterson RC, Smith GE, Waring SC, Ivnik RJ, Tangalos EG, Kokmen E. Mild cognitive imairment: clinical characterization and outcome. Arch Neurol 1999;56:303-308.

11. Dougall NJ, Bruggink S, Ebmeier KP. Systematic review of the diagnostic accuracy of 99-m-Tc-HMPAO-SPECT in dementia. Paychiatry 2004;12:554-570.

12. Jagust W, Thisted R, Devous MD, et al. SPECT perfusion imaging in the diagnosis of Alzheimer's disease: A clinical-pathologic study. Neurology 2001;56:950-956.

13. Bradley KM, O'Sullivan VT, Soper NDW, et al. Cerebral perfusion SPET correlated with Braak pathological stage in Alzheimer's disease. Brain 2002;125:1772-1781.

14. Kogure D, Matsuda H, Ohnishi T, Kumihiro T, Uno M, Takasaki M. Longitudinal evaluation of early Alzheimer disease using brain perfusion SPECT. J Nucl Med 2000;41(7):1155-1162.

15. Minoshima S, Giordani B, Berent S, Frey KA, Foster NL, Kuhl DE. Metabolic reduction in the posterior congulare cortex in very early Alzheimer's disease. Ann Neurol 1997;42:85-94.

16. Drzezga A, Riemenschneider M, Strassner B, et al. Cerebral glucose metabolism in patients with AD and different APOE genotypes. Neurology 2005;64:102-107.

17. Harris GJ, Lewis RF, Satlin A, et al. Dynamic susceptibility contrast MR imaging of regional cerebral blood volume in Alzheimer disease: A promising alternative to nuclear medicine. Am J Neuroradiol 1998;19:1727-1732.

18. Alexander GE, Chen K, Pietrini P, Rapoport SI, Reiman EM. Longitudinal PET evaluation of cerebral metabolic decline in dementia: a potential outcome measure in Alzheimer's disease treatment studies. Am J Psychiatry 2002;159:738-745.

19. Bonte FJ, Harris TS, Roney CA, Hynan LS. Differential diagnosis between Alzheimer's and frontotemporal disease by the posterior cingulate sign. J Nucl Med 2004;45(5):771-774.

20. Huang C, Wahlund L-O, Svensson L, Winblad B, Julin P. Cingulate cortex hypoperfusion predicts Alzheimer's disease in mild cognitive impairment. Bio Med Central Neurology 2002;2(9):1-6.

21. Karas GB, Burton EJ, Rombouts SARB, et al. A comprehensive study of gray metter loss in patients with Alzheimer's disease using optimized voxel-based morphometry. NeuroImage 2003;18:895-907.

22. Du AT, Schuff N, Kramer JH, et al. Higher atrophy rate of entorhinal cortex than hippocampus in AD. Neurology 2004;62:422-427.

23. Ishii K, Kawachi T, Sasaki H, et al. Voxel-based morphometric comparison between early- and late-onset mild Alzheimer's disease and assessment of diagnostic performance of z score images. Am J Neuroradiol 2005;26(2):333-340.

24. Testa C, Laakso MP, Sabattoli F, et al. A comparison between the accuracy of voxel-based morphometry and hippocampal volumetry in Alzheimer's disease. J Magn Res Imaging 2004;19:274-282.

25. Good CD, Johnsrude IS, Ashburner J, Henson RNA, Friston KJ, Frackowiak RSJ. A voxel-based morphometric study of aging in 465 normal adult human beings. NeuroImage 2001;14(1 Pt 1):21-36.

26. Alsop DC, Detre JA, Grossman M. Assessment of cerebral blood flow in Alzheimer's disease by spin-labeled magnetic resonance imaging. Annals of Neurology 2000;47(1):93-100.

27. Johnson NA, Jahng G-H, Weiner MW, et al. Pattern of cerebral hypoperfusion in Alzheimer disease and mild cognitive impairment measured with arterial spin-labeling MR imaging: Initial experience. Radiology 2005;234:851-859.

28. Drzezga A, Lautenschlager N, Siebner H, et al. Cerebral metabolic changes accompanying conversion of mild cognitive impairment into Alzheimer's disease: a PET follow-up study. Eur J Nucl Med Mol Imaging 2003;30:1104-1113.

29. Nestor PJ, Fryer TD, Smielewski P, Hodges JR. Limbic hypometabolism in Alzheimer's disease and mild cognitive impairment. Ann Neurol 2003;54:343-351.

30. Chetelat G, Desgranges B, de la Sayette V, Viader F, Eustache F, Baron J-C. Mild cognitive impairment. Can FDG-PET predict who is to rapidly convert to Alzheimer's disease? Neurology 2003;60:1374-1377.

31. Berent S, Giordani B, Foster N, et al. Neuropsychological function and cerebral glucose utilization in isolated memory impairment and Alzheimer's disease. J Psychiatr Res 1999;33(1):7-16.

32. De Santi S, de Leon MJ, Rusinek H, et al. Hippocampal formation, glucose metabolism, and volume losses in MCI and AD. Neurobiology of Aging 2001;22:529-539.

33. Pennanen C, Kivipelto M, Tuomainen S, et al. Hippocampus and entorhinal cortex in mild cogniitve impairment and early AD. Neurobiol Aging 2004;25:303-310.

34. Visser PJ, Verhey FRJ, Hofman PAM, Scheltens P, Jolles J. Medial temporal lobe atrophy predicts Alzheimer's disease in patients with minor cognitive impairment. J Neurol Neurosur Psychiatry 2002;72:491-497.

35. Dickerson BC, Salary DH, Bates JF, et al. Medial temporal lobe function and structure in mild cognitive impairment. Ann Neurol 2004;56:27-35.

36. Du AT, Schuff N, Amend D, et al. Magnetic resonance imaging of the entorhinal cortex and hippocampus in mild cognitive impairment and Alzheimer's disease. J Neurol Neurosurg Psychiatry 2001;71:441-447.

37. Jack CR, Petersen RC, Xu YC, et al. Medial temporal atrophy on MRI in normal aging and very mild Alzheimer's disease. Neurology 1997;49:786-794.

38. Killiany RJ, Hyman BT, Gomez-Isla T, et al. MRI measures of entorhinal cortex vs hippocampus in preclinical AD. Neurology 2002;58:1188-1196.

39. Soininen HS, Partanen K, Pitkanen A, et al. Volumetric MRI analysis of the amygdala and the hippocampua in subjects with age-associated memory impairment: Correlation to visual and verbal memory. Neurology 1994;44:1660-1668.

40. Bell-McGinty S, Lopez OL, Meltzer CC, et al. Differential cortical atrophy in subgroups of mild cognitive impairment. Arch Neurol In Press.

41. Karas GB, Scheltens P, Rombouts SARB, et al. Global and local gray matter loss in mild cognitive impairment and Alzheimer's disease. NeuroImage 2004;23:708-716.

42. Chetelat G, Desgranges B, de la Sayette V, Viader F, Eustache F, Baron J-C. Mapping gray matter loss with voxel-based morphometry in mild cognitive impairment. NeuroReport 2002;13(15):1939-1943.

43. Ostergaard L, Chesler DA, Weisskoff RM, Sorensen AG, Rosen BR. Modeling cerebral blood flow and flow heterogeneity from magnetic resonance residue data. J Cerebral Blood Flow Metab 1999;18:425-432.

44. Schreiber WG, Guckel F, Stritzke P, Schmiedek P, Schwartz A, Brix G. Cerebral blood flow and cerebrovascular reserve capacity: estimation by dynamic magnetic resonance imaging. J Cereb Blood Flow Metab 1998;18(10):1143-1156.

45. Williams DS, Detre JA, Leigh JS, Koretsky AP. Magnetic reonance imaging of perfusion using spin inversion of arterial water. PNAS USA 1992;89:212-216.

46. Wong EC, Buxton RB, Frank LR. A theoretical and experiemental comparison of continous and pulsed arterial spin labeling techniques for quantitative perfusion imaging. Magn Reson Med 1998;40:348-355.

47. Detre JA, Leigh JS, Williams DS, Koretsky AP. Perfusion imaging. Magn Reson Med 1992;23:37-45.

48. Abragam A. Principles of Nuclear Magnetism. Oxford: Clarendon Press, 1961.

49. Dixon WT, Du LN, Faul DD, Gado M, Rossnick S. Projection angiograms of blood labeled by adiabatic fast passage. Magn Reson Med 1986;3(3):454-462.

50. Williams DS, Grandis DJ, Zhang W, Koretsky AP. Magnetic resonance imaging of perfusion in the isolated rat heart using spin inversion of arterial water. Magn Reson Med 1993;30(3):361-365.

51. Wolff SD, Balaban RS. Magnetization transfer contrast (MTC) and tissue water proton relaxation in vivo. Magn Reson Med 1989;10(1):135-144.

52. Zhang W, Williams DS, Detre JA, Koretsky AP. Measurement of brain perfusion by volume-localized NMR spectroscopy using inversion of arterial water spins: accounting for transit time and cross-relaxation. Magn Reson Med 1992;25(2):362-371.

53. Ye FQ, Mattay VS, Jezzard P, Frank JA, Weinberger DR, McLaughlin AC. Correction for vascular artifacts in cerebral blood flow values measured by using arterial spin tagging techniques. Magn Reson Med 1997;37(2):226-235.

54. Alsop DC, Detre JA. Reduced transit-time sensitivity in noninvasive magnetic resonance imaging of Human cerebral blood flow. Journal of Cerebral Blood Flow and Metabolism 1996;16:1236-1249.

55. Henkelman RM, Huang X, Xiang Q, Stanisz GJ, Swanson SD, Bronskill MJ. Quantitative interpretation of magnetization transfer. Magn Resn Med 1993;29:759-766.

56. Morrison C, Henkelman RM. A model of magnetization transfer in tissues. Magn Resn Med 1995;33:475-482.

57. Sled JG, Pike GB. Quantitative Imaging of Magnetization Transfer Exchange and Relaxation Properties In Vivo Using MRI. Magnetic Resonance in Medicine 2001;46:923-931.

58. Tozer D, Ramanti A, Barker GJ, Davies GR, Miller DH, Tofts PS. Quantitative Magnetization Transfer Mapping of Bound Protons in Multiple Sclerosis. Magnetic Resonance in Medicine 2003;50:83-91.

59. Silva AC, Zhang W, Williams DS, Koretsky AP. Multi-slice MRI of rat brain perfusion during amphetamine stimulation using arterial spin labeling. Magn Reson Med 1995;33(2):209-214.

60. Talagala SL, Barbier EL, Williams DS, Silva AC, Koretsky AP. Multislice perfusion MRI using continuous arterial water labeling: Controlling for MT effects with simultaneous proximal and distal RF. 6th ISMRM 1998:P381.

61. Alsop DC, Detre JA. Multisection cerebral blood flow imaging with continous arterial spin labeling. Radiology 1998;208:410-416.

62. Detre JA, Alsop DC. Perfusion magnetic resonance imaging with continuous arterial spin labeling: methods and clinical applications in the central nervous system. Eur J Radiol 1999;30(2):115-124.

63. Gach HM, Kam AW, Talagala SL, Reid ED. double adiabatic inversion efficiencies measured in vitro. Proceedings of 9th ISMRM Annual meeting, Glasgow, Scotland 2001:p1568.

64. Pekar J, Jezzard, P., Roberts, D. A., Leigh, J. S., Frank, J. A., McLaughlin, A. C. Perfusion imaging with compensation for asymmetric magnetization transfer effects. Magn Reson Med 1996;35:70-79.

65. Chen M. 3-D Deformable Registration Using a Statistical Atlas with Applications in Medicine. doctoral dissertation, Carnegie Mellon University, October. 1999.

66. Liang Z, Lauterbur PC. Principles of Magnetic Resonance Imaging. New York: IEEE Press, 1999.

67. Alpert NM, Eriksson L, Chang JY, et al. Strategy for the measurement of regional cerebral blood flow using short-lived tracers and emission tomography. J Cereb Blood Flow Metab 1984;4(1):28-34.

68. Watabe H, Itoh M, Cunningham V, et al. Noninvasive quantification of rCBF using positron emission tomography. J Cereb Blood Flow Metab 1996;16(2):311-319.

69. Treyer V, Jobin M, Burger C, Teneggi V, Buck A. Quantitative cerebral H2(15)O perfusion PET without arterial blood sampling, a method based on washout rate. Eur J Nucl Med Mol Imaging 2003;30(4):572-580.

70. Friberg L, Andersen AR, Lassen NA, Holm S, Dam M. Retention of 99mTc-bicisate in the human brain after intracarotid injection. J Cereb Blood Flow Metab 1994;14 Suppl 1:S19-27.

71. Sokoloff L, Reivich M, Kennedy C, et al. The [14C]deoxyglucose method for the measurement of local cerebral glucose utilization: theory, procedure, and normal values in the conscious and anesthetized albino rat. J Neurochem 1977;28(5):897-916.

72. Odano I, Ohkubo M, Takahashi M. Quantification of cerebral blood flow and partition coefficient using iodine-123-iodoamphetamine. J Nucl Med 1997;38(8):1248-1253.

73. Ostergaard L, Sorensen AG, Kwong KK, Weisskoff RM, Gyldensted C, Rosen BR. High resolution measurement of cerebral blood flow using intravascular tracer bolus passages. Part II: Experimental comparison and preliminary results. Magn Reson Med 1996;36(5):726-736.

74. Buxton RB, Frank LR, Wong EC, Siewert B, Warach S, Edelman RR. A general kinetic model for quantitative perfusion imaging with arterial spin labeling. Magn Reson Med 1998;40:383-396.

75. McLaughlin AC, Ye FQ, Pekar JJ, Santha AK, Frank JA. Effect of magnetization transfer on the measurement of cerebral blood flow using steady-state arterial spin tagging approaches: a theoretical investigation. Magn Reson Med 1997;37(4):501-510.

76. Zhang W, Silva AC, Williams DS, Koretsky AP. NMR measurement of perfusion using arterial spin labeling without saturation of macromolecular spins. Magn Reson Med 1995;33(3):370-376.

77. Pell GS, Thomas DL, Lythgoe MF, et al. Measurement of perfusion using arterial spin tagging with the FOCI pulse. ISMRM 6th Annual Meeting 1998:p1190.

78. Ostergaard L, Smith DF, Vestergaard-Poulsen P, et al. Absolute cerebral blood flow and blood volume measured by magnetic resonance imaging bolus tracking: comparison with positron emission tomography values. J Cereb Blood Flow Metab 1998;18(4):425-432.

79. Silva AC, Zhang W, Williams DS, Koretsky AP. Estimation of water extraction fractions in rat brain using magnetic resonance measurement of perfusion with arterial spin labeling. Magn Reson Med 1997;37(1):58-68.

80. Silva AC, Williams DS, Koretsky AP. Evidence for the exchange of arterial spin-labeled water with tissue water in rat brain from diffusion-sensitized measurements of perfusion. Magn Reson Med 1997;38(2):232-237.

81. Petrella JR, DeCarli C, Dagli M, et al. Assessment of whole-brain vasodilatory capacity with acetazolamide challenge at 1.5 T using dynamic contrast imaging with frequency-shifted burst. AJNR Am J Neuroradiol 1997;18(6):1153-1161.

82. Alsop DC, Detre JA. Background supressed 3D RARE arterial spin labeled perfusion MRI. Proceedings of 7th ISMRM Annual meeting 1999:p601.

83. Grad J, Bryant RG. Nuclear Magnetic Cross-Relaxation Spectroscopy. . J. Magn. Resonance 1990;90:1-8.

84. Kubo R, Tomita K. A general theory of magnetic resonace absoption. J. Phys. Soc. Jpn 1954;9:888-919.

85. Iino M. Transition from Lorentzian to Gaussian line shape of magnetization transfer spectrum in bovine serum albumin solutions. Magn Reson Med 1994;32(4):459-463.

86. Li JG, Graham SJ, Henkelman RM. A flexible magnetization transfer line shape derived from tissue experimental data. Magn Reson Med 1997;37(6):866-871.

87. Sled JG, Pike GB. Quantitative interpretation of magnetization transfer in spoiled gradient echo MRI sequences. J Magn Reson 2000;145(1):24-36.

88. Holt RW, Duerk JL, Hua J, Hurst GC. Estimation of Bloch model MT spin system parameters from Z-spectral data. Magn Reson Med 1994;31(2):122-130.

89. Ramani A, Dalton C, Miller DH, Tofts PS, Barker GJ. Precise estimate of fundamental in-vivo MT parameters in human brain in clinically feasible times. Magn Reson Imaging 2002;20(10):721-731.

90. Thulborn KR, Boada FE, Shen GX, Christensen JD, Reese TG. Correction of B1 inhomogeneities using echo-planar imaging of water. Magn Reson Med 1998;39(3):369-375.

91. Press WH, Flannery BP, Teukolsky SA, Vetterling WT. Numerical Recipes, the Art of Scientific Computing. Cambridge: Cambridge University Press, 1998.

92. Caines GH, Schleich T, Rydzewski JM. Incorporation of magnetization transfer into the formalism for rotating-frame spin-lattice proton NMR relaxation in the presence of an off-resonance-irradiation field. Jounal of Magnetic Resonance 1991;95(3):558-566.

93. Chalela JA, Alsop DC, Gonzalez-Atavales JB, Maldjian JA, Kasner SE, Detre JA. Magnetic resonance perfusion imaging in acute ischemic stroke using continuous arterial spin labeling. Stroke 2000;31(3):680-687.

94. Detre JA, Alsop DC, Vives LR, Maccotta L, Teener JW, Raps EC. Noninvasive MRI evaluation of cerebral blood flow in cerebrovascular disease. Neurology 1998;50(3):633-641.

95. Gonzalez-At JB, Alsop DC, Detre JA. Cerebral perfusion and arterial transit time changes during task activation determined with continuous arterial spin labeling. Magn Reson Med 2000;43:739-746.

96. Utting JF, Thomas DL, Gadian DG, Helliar RW, Lythgoe MF, Ordidge RJ. Understanding and optimizing the amplitude modulated control for multiple-slice continuous arterial spin labeling. Magn Reson Med 2005;54(3):594-604.

97. Werner R, Norris DG, Alfke K, Mehdorn HM, Jansen O. Improving the amplitude-modulated control experiment for multislice continuous arterial spin labeling. Magn Reson Med 2005;53(5):1096-1102.

98. Utting JF, Thomas DL, Gadian DG, Ordidge RJ. Velocity-driven adiabatic fast passage for arterial spin labeling: results from a computer model. Magn Reson Med 2003;49(2):398-401.

99. Maccotta L, Detre JA, Alsop DC. The efficiency of adiabatic inversion for perfusion imaging by arterial spin labeling. NMR Biomed 1997;10(4-5):216-221.

100. Marro KI, Hayes CE, Kushmerick MJ. A model of the inversion process in an arterial inversion experiment. NMR Biomed 1997;10(7):324-332.

101. Gach HM. Inversion efficiencies in pulsatile flow for arterial spin labeling. Proceedings of 10th ISMRM Annual Meeting, Honolulu 2002:p1071.

102. Gach HM, Kam AW, Reid ED, Talagala SL. Quantitative analysis of adiabatic fast passage for steady laminar and turbulent flows. Magn Reson Med 2002;47(4):709-719.

103. Zhernovoi AI. Fast adiabatic passage in nuclear magnetic resonance. Soviet Physics Solid State 1967;9:523-524.

104. Zaharchuk G, Ledden, P. J., et al. Multislice perfusion and perfusion territory imaging in humans with separate label and image coils. Magnetic Resonance in Medicine 1999;41:1093-1098.

105. Lee HK, Nalcioglu O, Moran PR. Spatially resolved flow velocity measurements and projection angiography by adiabatic passage. Magn Reson Imaging 1991;9(1):115-127.

106. Barth M, Moser E. Proton NMR relaxation times of human blood samples at 1.5 T and implications for functional MRI. Cell Mol Biol (Noisy-le-grand) 1997;43(5):783-791.

107. Zhernovoi AI. Changes of the magnetization projection Mz during adiabatic fast passage in nuclear magnetic resonance. Soviet Physics Solid State 1972;13(2):2159-2160.

108. Thomas DL, Lythgoe MF, van der Weerd L, Ordidge RJ, Gadian DG. Regional variation of cerebral blood flow and arterial transit time in the normal and hypoperfused rat brain measured using continuous arterial spin labeling MRI. J Cereb Blood Flow Metab 2006;26(2):274-282.

109. Wang J, Alsop DC, Li L, et al. Comparison of quantitative perfusion imaging using arterial spin labeling at 1.5 and 4.0 Tesla. Magn Reson Med 2002;48(2):242-254.

110. Wang H, Chu Y, al e. Regional cerebral hypoperfusion of medial temporal lobe in mild cognitive impairment. The 9th International Conference on Alzheimer's Disease and Related Disorders, Philadelphia 2004.

111. St Lawrence KS, Wang J. Effects of the apparent transverse relaxation time on cerebral blood flow measurements obtained by arterial spin labeling. Magn Reson Med 2005;53(2):425-433.

112. Ewing JR, Cao Y, Fenstermacher J. Single-coil arterial spin-tagging for estimating cerebral blood flow as viewed from the capillary: relative contributions of intra- and extravascular signal. Magn Reson Med 2001;46(3):465-475.

113. Parkes LM, Tofts PS. Improved accuracy of human cerebral blood perfusion measurements using arterial spin labeling: accounting for capillary water permeability. Magn Reson Med 2002;48(1):27-41.

114. Kwong KK, Chesler DA, Weisskoff RM, et al. MR perfusion studies with T1-weighted echo planar imaging. Magn Reson Med 1995;34(6):878-887.

115. Herscovitch P, Raichle ME. What is the correct value for the brain--blood partition coefficient for water? J Cereb Blood Flow Metab 1985;5(1):65-69.

116. Warmuth C, Gunther M, Zimmer C. Quantification of blood flow in brain tumors: comparison of arterial spin labeling and dynamic susceptibility-weighted contrast-enhanced MR imaging. Radiology 2003;228(2):523-532.

117. Thomas DL, Lythgoe MF, van der Weerd L, Ordidge RJ, Gadian DG. Regional variation of cerebral blood flow and arterial transit time in the normal and hypoperfused rat brain measured using continuous arterial spin labeling MRI. J Cereb Blood Flow Metab 2005.

118. Spees WM, Yablonskiy DA, Oswood MC, Ackerman JJ. Water proton MR properties of human blood at 1.5 Tesla: magnetic susceptibility, T(1), T(2), T*(2), and non-Lorentzian signal behavior. Magn Reson Med 2001;45(4):533-542.

119. Ye FQ, Berman, K. F., et al. H215O PET validation of steady-state arterial spin tagging cerebral blood flow measurements in humans. Magnetic Resonance in Medicine 2000;44:450-456.

120. Pantano P, Baron JC, Lebrun-Grandie P, Duquesnoy N, Bousser MG, Comar D. Regional cerebral blood flow and oxygen consumption in human aging. Stroke 1984;15(4):635-641.

121. Lopez OL, Jagust WJ, Dekosky ST, et al. Prevalence and classification of mild cognitive impairment in the cardiovascular health study cognitive. Arch Neurol 2003;60:1385-1389.

122. Kuller LH, Lopez OL, Newman A, et al. Risk factors for dementia in the cardiovascular health cognition study. Neuroepidemiology 2003;22(1):13-22.

123. Tonini G, Shanks MF, Venneri A. Short-term longitudinal evaluation of cerebral flow in mild Alzheimer's disease. Neurol Sci 2003;24(1):24-30.

124. Ashburner J, Friston KJ. Voxel-based morphometry--the methods. Neuroimage 2000;11(6 Pt 1):805-821.

125. Ishii K, Sasaki, M., Yamaji, S., Sakamoto, S., Kitagaki, H., Mori, E. Demonstration of decreased posterior cingulate perfusion in mild Alzheimer's disease by means of H215O positron emisson tomography. Eur J Nucl Med 1997;24(6):670-673.

126. Kumakura Y, Momose T, Oku S, Ohtake T, Nishikawa J, Sasaki Y. Analysis fo cerebral blood flow SPEC imaging on standard brian atlas in patients with dementia of Alzheimer type. The Japanese Jounal of nuclear medicine 1998;35(1):29-32.

127. Garrido GE, Furuie SS, Buchpiguel CA, et al. Relation between medial temporal atrophy and funtional brain activity during memory processing in Alzheimer's disease: a combined MRI and SPEC study. Jounal of neurology, neurosurgery, and psychiatry 2002;73(5):508-516.

128. Scarmeas N, Habeck CG, Zarahn E, et al. Covariance PET patterns in early Alzheimer's disease and subjects with cognitive impairment but no dementia: utility in group discrimination and correlations with functional performance. Neuroimage 2004;23(1):35-45.

129. Nestor PJ, Fryer TD, Ikeda M, Hodges JR. Retrosplenial cortex (BA 29/30) hypometabolism in mild cognitive impairment (prodromal Alzheimer's disease). Eur J Neurosci 2003;18(9):2663-2667.

130. Ibanez V, Pietrini P, Alexander GE, et al. Regional glucose metabolic abnormalities are not the result of atrophy in Alzheimer's disease. Neurology 1998;50(6):1585-1593.

131. Ibanez V, Pietrini P, Furey ML, et al. Resting state brain glucose metabolism is not reduced in normotensive healthy men during aging, after correction for brain atrophy. Brain Res Bull 2004;63(2):147-154.

132. Bokde AL, Pietrini P, Ibanez V, et al. The effect of brain atrophy on cerebral hypometabolism in the visual variant of Alzheimer disease. Arch Neurol 2001;58(3):480-486.

133. Mosconi L, Perani D, Sorbi S, et al. MCI conversion to dementia and the APOE genotype: a prediction study with FDG-PET. Neurology 2004;63:2332-2340.

134. Imran MB, Kawashima R, Awata S, et al. Tc-99m HMPAO SPEC in the evaluation of Alzheimer's disease correlation between neuropsychiatric evaluation and CBF images. J Neurol Neurosurg Psychiatry 1999;66(2):228-232.

135. Matsuda H, Kanetaka H, Ohnishi T, et al. Brain SPET abnormalities in Alzheimer's disease before and after atrophy correction. Eur J Nucl Med Mol Imaging 2002;29(11):1502-1505.

136. Carmichael OT, Aizenstein HA, Davis SW, et al. Atlas-based hippocampus segmentation in Alzheimer's disease and mild cognitive impairment. Neuroimage 2005;27(4):979-990.

137. Wu M, Carmichael O, Lopez-Garcia P, Carter CS, Aizenstein HJ. Quantitative comparison of AIR, SPM, and the fully deformable model for atlas-based segmentation of functional and structural MR images. Hum Brain Mapp 2006.

138. Woods RP, Grafton ST, Holmes CJ, Cherry SR, Mazziotta JC. Automated image registration: I. General methods and intrasubject, intramodality validation. Journal of Computer Assisted Tomography 1998;22:139-152.

139. Ashburner J, Friston KJ. Nonlinear spatial normalization using basis functions. Hum Brain Mapp 1999;7(4):254-266.

140. Carmichael OT, Aizenstein HA, Davis SW, et al. Atlas-based hippocampus segmentation in Alzheimer's disease and mild cognitive impairment. Neuroimage 2005.

141. McKhann G, Drachman D, Folstein M, Katzman R, Price D, Stadlan EM. Clinical diagnosis of Alzheimer's disease: report of the NINCDS-ADRDA Work Group under the auspices of Department of Health and Human Services Task Force on Alzheimer's Disease. Neurology 1984;34(7):939-944.

142. Gach HM, Dai W. Simple model of double adiabatic inversion (DAI) efficiency. Magn Reson Med 2004;52(4):941-946.

143. Holmes CJ, Hoge R, Collins L, Woods R, Toga AW, Evans AC. Enhancement of MR images using registration for signal averaging. J Comput Assist Tomogr 1998;22:324-333.

144. Holman BL, Johnson KA, Gerada B, Carvalho PA, Satlin A. The sintigraphic apperance of Alzheimer's disease: as prospective study using technetium-99m-HMPAO SPEC. J Nucl Med 1992;33:181-185.

145. Celsis P. Age-related cognitive decline, mild cognitive impairment or preclinical Alzheimer's disease? Ann Med 2000;32(1):6-14.

146. Friston KJ, Holmes A, Poline JB, Price CJ, Frith CD. Detecting activations in PET and fMRI: levels of inference and power. Neuroimage 1996;4(3 Pt 1):223-235.

147. Friston KJ, Holmes AP, Worsley KJ, Poline J-B, Frith CD, Frackowiak RSJ. Statistical parametric maps in functional imaging: A general linear approach. Human Brain Mapping 1995;2:189-210.

148. Cormen TH, Leiserson CE, Rivest RL, Stein C. Introduction to Algorithms. New York: McGraw-Hill, 1990.

149. Mielke R, Kessler J, Szelies B, Herholz K, Wienhard K, Heiss WD. Normal and pathological aging--findings of positron-emission-tomography. J Neural Transm 1998;105(8-9):821-837.

150. Jagust WJ. Neuroimaging in dementia. Neurol Clin 2000;18(4):885-902.

151. Petrella JR, Coleman RE, Doraiswamy PM. Neuroimaging and early diagnosis of Alzheimer disease: a look to the future. Radiology 2003;226(2):315-336.

152. Lee YC, Liu RS, Liao YC, et al. Statistical parametric mapping of brain SPECT perfusion abnormalities in patients with Alzheimer's disease. Eur Neurol 2003;49(3):142-145.

153. Fox PT, Raichle ME. Focal physiological uncoupling of cerebral blood flow and oxidative metabolism during somatosensory stimulation in human subjects. Proc Natl Acad Sci 1986;83(1140-1144).

154. Kwong K, Belliveau J, Chesler D, et al. Dynamic magnetic resonance imaging of human brain activity during primary sensory stimulation. PNAS 1992;89:5675-5679.

155. Bandettini PA, Kwong KK, Davis TL, et al. Charcaterization of cerebral blood oxygenation and flow change during prolonged brain activation. Hum Brain Mapp 1997;5(2):93-109.

156. DeKosky ST, Ikonomovic MD, Styren SD, et al. Upregulation of choline acetyltransferase activity in hippocampus and frontal cortex of elderly subjects with mild cognitive impairment. Ann Neurol 2002;51(2):145-155.

157. Davis KL, Mohs RC, Marin D, et al. Cholinergic markers in elderly patients with early signs of Alzheimer's disease. JAMA 1999;281(15):1433-1434.

158. Kuhl DE, Koeppe RA, Minoshima S, et al. In vivo mapping of cerebral acetylcholinesterase activity in aging and Alzheimer's disease. Neurology 1999;52(4):691-699.

159. Ongur D, Ferry AT, Price JL. Architectonic subdivision of the human orbital and medial prefrontal cortex. J Comparative Neurology 2003;460:425-449.

160. Van Hoesen GW, Parvizi J, Chu CC. Orbitofrontal cortex pathology in Alzheimer's disease. Cereb Cortex 2000;10(3):243-251.

161. Koski L, Paus T. Functional connectivity of the anterior cingulate cortex within the human frontal lobe: a brain-mapping meta-analysis (review): Springer Verlag, 2000.

162. Vogt BA, Vogt LJ, Perl DP, Hof PR. Cytology of human caudomedial cingulate, retrosplenial, and caudal parahippocampal cortices. J Comp Neurol 2001;438(3):353-376.

163. Vogt BA, Berger GR, Derbyshire SW. Structural and functional dichotomy of human midcingulate cortex. Eur J Neurosci 2003;18(11):3134-3144.

164. Gomez-Isla T, Price JL, McKeel DW, Morris JC, Growdon JH, Hyman BT. Profound loss of layer II entrohimal cortex neurons occurs in very mild Alzheimer's disease. J Neurosci 1996;16(14):4491-4500.

165. Braak H, Braak E. Neuropathological stageing of Alzheimer-related changes. Acta Neuropathol 1991;82:239-259.

166. Ishii K, Sasaki M, Yamaji S, Sakamoto S, Kitagaki H, Mori E. Relatively preserved hippocampal glucose metabolism in mild Alzheimer's disease. Dement Geriatr Cogn Disord 1998;9(6):317-322.

167. Matsuda H. Cerebral blood flow and metabolic abnormalities in Alzheimer's disease. Ann Nucl Med 2001;15(2):85-92.

168. Papez JW. A proposed mechanism of emotion. Arch Neurol Psychiatry 1937;38:725-743.

169. Grossi D, Lopez OL, Martinez AJ. The mammillary bodies in Alzheimer's disease. Acta Neurological Scandinavica 1989;80:41-45.

170. Desgranges B, Baron J-C, Lalevee C, et al. The neural substrates of episodic memory impairment in Alzheimer's disease as revealed by FDG-PET: relationship to degree of deterioration. Brain 2002;125:1116-1124.

171. Grady CL, Furey ML, Pietrini P, Horvitz B, Rapoport SI. Altered brain functional connectivity and impaired short-term memory in Alzheimer's disease. Brain 2001;124:739-756.

172. Chetelat G, Landeau B, Eustache F, Mezenge F, Viader F, de la Sayette V. Using voxel-based morphometry to map the structural changes associated with rapid conversion in MCI: A longitudinal MRI study. NeuroImage In press.

173. Joffres MR, Hamet P, MacLean DR, L'Italien G J, Fodor G. Distribution of blood pressure and hypertension in Canada and the United States. Am J Hypertens 2001;14(11 Pt 1):1099-1105.

174. Wolf-Maier K, Cooper RS, Banegas JR, et al. Hypertension prevalence and blood pressure levels in 6 European countries, Canada, and the United States. Jama 2003;289(18):2363-2369.

175. Hajjar I, Kotchen JM, Kotchen TA. Hypertension: trends in prevalence, incidence, and control. Annu Rev Public Health 2006;27:465-490.

176. Knopman DS, Mosley TH, Catellier DJ, Sharrett AR. Cardiovascular risk factors and cerebral atrophy in a middle-aged cohort. Neurology 2005;65(6):876-881.

177. Pepine CJ, Kowey PR, Kupfer S, et al. Predictors of adverse outcome among patients with hypertension and coronary artery disease. J Am Coll Cardiol 2006;47(3):547-551.

178. Kilander L, Nyman H, Boberg M, Hansson L, Lithell H. Hypertension is related to cognitive impairment: a 20-year follow-up of 999 men. Hypertension 1998;31(3):780-786.

179. Kivipelto M, Helkala EL, Hanninen T, et al. Midlife vascular risk factors and late-life mild cognitive impairment: A population-based study. Neurology 2001;56(12):1683-1689.

180. Launer LJ, Masaki K, Petrovitch H, Foley D, Havlik R. The association between mid-life blood pressure levels and late life cognitive function: The Honolulu-Asia Aging Study. J Am Med Assoc 1995;274:1846-1851.

181. Reinprecht F, Elmstahl S, Janzon L, Andre-Petersson L. Hypertension and changes of cognitive function in 81-year-old men: a 13-year follow-up of the population study "Men born in 1914", Sweden. J Hypertens 2003;21(1):57-66.

182. Struijs JN, van Genugten ML, Evers SM, Ament AJ, Baan CA, van den Bos GA. Modeling the future burden of stroke in The Netherlands: impact of aging, smoking, and hypertension. Stroke 2005;36(8):1648-1655.

183. Mancia G. The association of hypertension and diabetes: prevalence, cardiovascular risk and protection by blood pressure reduction. Acta Diabetol 2005;42 Suppl 1:S17-25.

184. Kalaria RN. Small vessel disease and Alzheimer's dementia: pathological considerations. Cerebrovasc Dis 2002;13 Suppl 2:48-52.

185. Moossy J. Pathology of cerebral atherosclerosis. Influence of age, race, and gender. Stroke 1993;24(12 Suppl):I22-23; I31-22.

186. Tanoi Y, Okeda R, Budka H. Binswanger's encephalopathy: serial sections and morphometry of the cerebral arteries. Acta Neuropathol (Berl) 2000;100(4):347-355.

187. Qiu D, Mei J, Tanihata T, Kawaminami K, Minowa M. A cohort study on cerebrovascular disease in middle-aged and elderly population in rural areas in Jiangxi Province, China. J Epidemiol 2003;13(3):149-156.

188. Jennings JR, Muldoon MF, Ryan C, et al. Reduced cerebral blood flow response and compensation among patients with untreated hypertension. Neurology 2005;64(8):1358-1365.

189. Gianaros PJ, Derbyshire SW, May JC, Siegle GJ, Gamalo MA, Jennings JR. Anterior cingulate activity correlates with blood pressure during stress. Psychophysiology 2005;42(6):627-635.

190. Gianaros PJ, Greer PJ, Ryan CM, Jennings JR. Higher blood pressure predicts lower regional grey matter volume: Consequences on short-term information processing. Neuroimage 2006;31(2):754-765.

191. Korf ES, White LR, Scheltens P, Launer LJ. Midlife blood pressure and the risk of hippocampal atrophy: the Honolulu Asia Aging Study. Hypertension 2004;44(1):29-34.

192. Kuller L, Fisher L, McClelland R, et al. Differences in prevalence of and risk factors for subclinical vascular disease among black and white participants in the Cardiovascular Health Study. Arterioscler Thromb Vasc Biol 1998;18(2):283-293.

193. Fahn S, Elton RI. UPDRS Development Committee: Unified Parkinsons Rating Scale. In: Fahn S, Marsden CD, Caine D, Goldstein M, eds. Recent developments in Parkinson's disease. Florham Park: MacMillan Healthcare Information, 1987: 153-163.

194. Hachinski VC, Iliff LD, Zilhka E, et al. Cerebral blood flow in dementia. Arch Neurol 1975;32(9):632-637.

195. Fried LP, Kronmal RA, Newman AB, et al. Risk factors for 5-year mortality in older adults: The cardiovascular health study. JAMA 1998;279:585-592.

196. Nelson HE, O'Connell A. Dementia: the estimation of premorbid intelligence levels using the New Adult Reading Test. Cortex 1978;14(2):234-244.

197. Raven RW. Progressive patient care. Br Med J 1962;5270:43-44.

198. Delis DC, Freeland J, Kramer JH, Kaplan E. Integrating clinical assessment with cognitive neuroscience: construct validation of the California Verbal Learning Test. J Consult Clin Psychol 1988;56(1):123-130.

199. Huff FJ, Collins C, Corkin S, Rosen TJ. Equivalent forms of the Boston Naming Test. J Clin Exp Neuropsychol 1986;8(5):556-562.

200. Wechsler D. Intellectual development and psychological maturity. Child Dev 1950;21(1):45-50.

201. Baddeley AD. Selective attention and performance in dangerous environments. Br J Psychol 1972;63(4):537-546.

202. Klove H. Clinical Neuropsychology. Med Clin North Am 1963;47:1647-1658.

203. Teng EL, Chui HC. The Modified Mini-Mental State (3MS) examination. J Clin Psychiatry 1987;48(8):314-318.

204. Gongora MC, Qin Z, Laude K, et al. Role of extracellular superoxide dismutase in hypertension. Hypertension 2006;48(3):473-481.

205. Miller AA, Megson IL, Gray GA. Inducible nitric oxide synthase-derived superoxide contributes to hypereactivity in small mesenteric arteries from a rat model of chronic heart failure. Br J Pharmacol 2000;131(1):29-36.

206. Kelm M, Dahmann R, Wink D, Feelisch M. The nitric oxide/superoxide assay. Insights into the biological chemistry of the NO/O-2. interaction. J Biol Chem 1997;272(15):9922-9932.

207. Zonta M, Angulo MC, Gobbo S, et al. Neuron-to-astrocyte signaling is central to the dynamic control of brain microcirculation. Nat Neurosci 2003;6(1):43-50.

208. Filosa JA, Bonev AD, Nelson MT. Calcium dynamics in cortical astrocytes and arterioles during neurovascular coupling. Circ Res 2004;95(10):e73-81.

209. Cirrito JR, Yamada KA, Finn MB, et al. Synaptic activity regulates interstitial fluid amyloid-beta levels in vivo. Neuron 2005;48(6):913-922.

210. Snowdon DA, Grainer LH, Mortimer JA, Riley KP, Grainer PA, Markesbery WR. Brain infarction and the clinical expression of Alzheimer disease: The nun study. JAMA 1997;277(10):813-817.

211. Petrovitch H, Ross GW, Steinborn SC, et al. AD lesions and infarcts in demented and non-demented Japanese-American men. Ann Neurol 2005;57:98-103.

212. Petrovitch H, White LR, Izmirilian G, et al. Midlife blood pressure and neuritic plaques, neurofibrillary tangles, and brain weight at death: the HAAS. Honolulu-Asia aging Study. Neurobiol Aging 2000;21(1):57-62.

213. Forette F, Seux ML, Staessen JA, et al. Prevention of dementia in randomised double-blind placebo-controlled Systolic Hypertension in Europe (Syst-Eur) trial. Lancet 1998;352(9137):1347-1351.

214. Tzourio C, Anderson C, Chapman N, et al. Effects of blood pressure lowering with perindopril and indapamide therapy on dementia and cognitive decline in patients with cerebrovascular disease. Arch Intern Med 2003;163(9):1069-1075.

215. Dufouil C, Chalmers J, Coskun O, et al. Effects of blood pressure lowering on cerebral white matter hyperintensities in patients with stroke: the PROGRESS (Perindopril Protection Against Recurrent Stroke Study) Magnetic Resonance Imaging Substudy. Circulation 2005;112(11):1644-1650.